Louisiana Tech University

Louisiana Tech Digital Commons

Summer 2016

Investigation of small-scale thermal recovery and storage systems

Suvhashis Thapa
Louisiana Tech University

Recommended Citation

INVESTIGATION OF SMALL-SCALE THERMAL RECOVERY AND STORAGE SYSTEMS

by

Suvhashis Thapa, M.S.

A Dissertation Presented in Partial Fulfillment
of the Requirements for the Degree of
Doctor of Philosophy

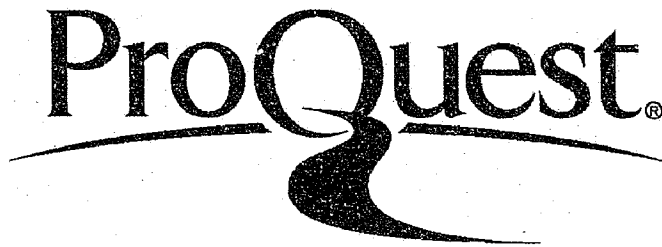COLLEGE OF ENGINEERING AND SCIENCE
LOUISIANA TECH UNIVERSITY

August 2016

ProQuest Number: 10301329

ProQuest 10301329

LOUISIANA TECH UNIVERSITY

THE GRADUATE SCHOOL
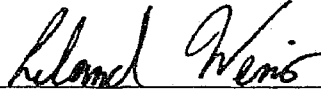
06/09/2016
_____
Date

We hereby recommend that the dissertation prepared under our supervision

by Suvhashis Thapa, M.S.
_____
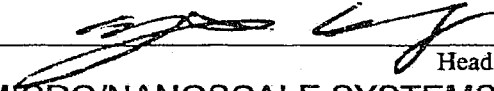
entitled_____

"INVESTIGATION OF SMALL-SCALE THERMAL RECOVERY AND

STORAGE SYSTEMS"

_____

be accepted in partial fulfillment of the requirements for the Degree of

DOCTOR OF PHILOSOPHY IN ENGINEERING

_____
Supervisor of Dissertation Research
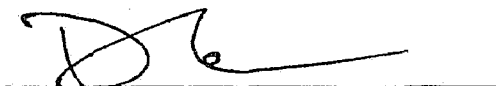
_____
Head of Department

MICRO/NANOSCALE SYSTEMS
_____
Department
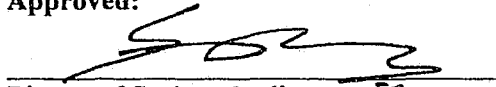
Recommendation concurred in:

_____

_____

_____   Advisory Committee

_____

Approved: Approved:
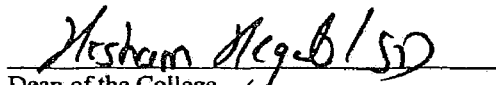
_____   _____
Director of Graduate Studies   Dean of the Graduate School

_____
Dean of the College

ABSTRACT

An approach to recover and store waste heat is presented in this dissertation. The waste heat is the energy that is rejected to the environment without being put to practical use and it is a result of both equipment inefficiency and thermodynamic limitation on the equipment and the process. In a typical Otto cycle, for instance, out of the total energy consumed by the system, only one-third of the energy is converted into useful work and the rest is discharged in the environment as waste heat [1]. For a spark ignition, a 1.4 liters internal combustion engine with the thermal efficiency of 15% to 32%, 1.7 kW to 45 kW of energy is wasted through coolant in the radiator and 4.6 kW to 120 kW of energy is wasted by the exhaust gas [1, 2]. Similar to the case of industry, 20% to 50% of the to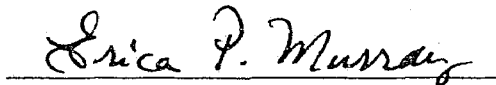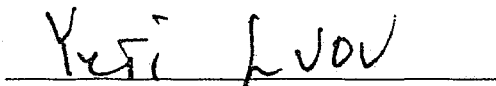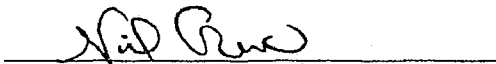tal energy consumed during an industrial process is rejected as waste heat [3]. These losses could be minimized either by improving the efficiency of the system itself or via the installation of a secondary waste heat recovery system. The recovery system uses the losses to generate mechanical or electrical work to enhance the efficiency of the primary system [4]. In addition to thermal recovery, thermal storage can play an important role in thermal energy scavenging and efficiency. The thermal storage technique is well established in a solar power plant where the excess heat and/or the captured heat itself is stored temporarily in a thermal storage device. The thermal energy storage (TES) process is then reversed, allowing the stored heat to be made available to a boiler at the periods of higher energy demand. Such

notion of heat recovery and heat storage via the utilization of microdevice and phase change material based TES is presented in this dissertation.

APPROVAL FOR SCHOLARLY DISSEMINATION

The author grants to the Prescott Memorial Library of Louisiana Tech University the right to reproduce, by appropriate methods, upon request, any or all portions of this Dissertation. It is understood that "proper request" consists of the agreement, on the part of the requesting party, that said reproduction is for his personal use and that subsequent reproduction will not occur without written approval of the author of this Dissertation. Further, any portions of the Dissertation used in books, papers, and other works must be appropriately referenced to this Dissertation.

Finally, the author of this Dissertation reserves the right to publish freely, in the literature, at any time, any or all portions of this Dissertation.

Author **SUVHASHIS THAPA**

Date **06/09/2016**

DEDICATION

Mother, Nirmala Chauhan;

Father, Khagendra Bahadur Thapa;

Wife, Shistata Nirula;

Aunt, Nilam Bhattarai;

Friend, Nir Jung Karki.

TABLE OF CONTENTS

LIST OF TABLES

LIST OF FIGURES

ACKNOWLEDGMENTS

It would not have been possible to write this dissertation without the help and support from the kind people around me, some of whom it is possible to give particular mention here.

First and foremost, I am heartily thankful to my advisor, Dr. Leland Weiss, for his guidance and support from the initial to the final stage of the project. I attribute the level of my PhD degree to his encouragement and effort, and without him, this dissertation would not have been completed or written.

I would like to thank Dr. Niel Crews for accepting me in his lab and teaching me the basics of performing research while I was working on my master's degree.

I would like to thank Aryn Hays, Ashok Baniya, Eric Borquist, Sangeet Shrestha, and other workers in Dr. Weiss's laboratory for being friendly and supportive.

I would like to thank my parents, my wife and friends (especially Suraj and Ilija). They were always supporting and encouraging me with their best wishes.

CHAPTER 1

INTRODUCTION

Energy has always been a vital resource in human development. The world's economic and technological development are dependent upon the adoption of sources that has a higher energy content. Since the invention of fire to the industrial revolution, mankind has experienced major shifts in energy resources. Today in the 21st century fossil fuels like coal, oil, and natural gas have become the reliant energy sources. Different sectors like industry and transportation require fossil fuel as a primary source of energy. The total energy consumed by the United States alone as indicated by the U.S. Department of Energy was 97.7 quadrillions BTUs (British Thermal units) in the year 2012 [5]. The industry and transportation hold approximately 48% of the total energy consumed [6]. This figure is expected to reach 107.64 quadrillion BTUs in 2014 with an increasing rate of approximately 0.32% per year [5]. To address this energy concerns about fossil fuel, alternative energy resources have to be explored.

According to the Department of Energy prediction, utilization of renewable energy as an alternative resource in total energy consumption will elevate to 16% by 2040 [5]. With already emerged resources such as solar, wind, hydro, geothermal and biomass, the waste heat could become another prospective future alternative renewable resource as well. The reason is its abundance in availability. A graphical

survey produced by the Lawerence Livermore National Laboratory in 2014 shows all estimated energy sources in the U.S., their uses, and how much of that energy is put to useful work and how much is wasted is presented in Figure 1.1 [7]. This is an evidence illustrating the waste heat availability and its possibilities to become a potential energy source itself.
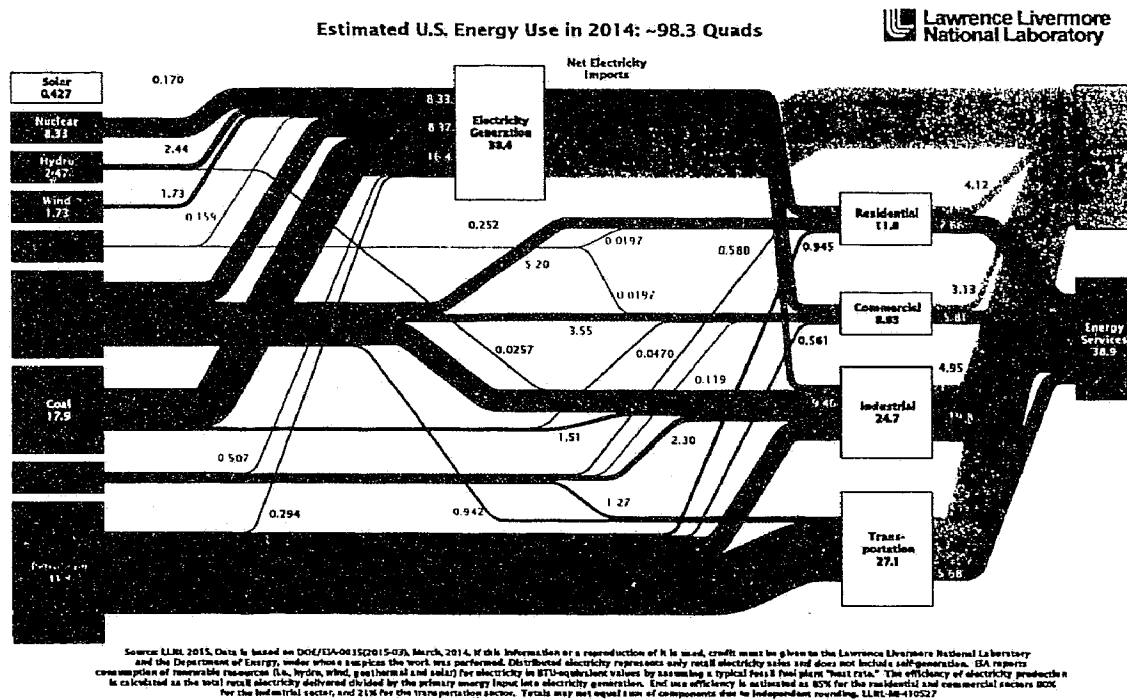
Figure 1.1: A graphical view of estimated energy use in the U.S. produced by Lawerence Livemore National Laboratory.

According to the survey, U.S. consumed approximately 98.3 quadrillion BTUs of energy in the year 2014 of which only 38.9 quadrillion BTUs was put to practical use and the remaining 59.4 quadrillion BTUs was discarded as waste heat. The rejected energy was approximately 61% of the total energy consumed in that year.

In the transportation sector, the conversion of energy to useful work was much worst (refer to Figure 1.1). The transportation sector consumed approximately 27.1 quadrillion BTUs of energy in which only 5.68 quadrillion BTUs was converted to useful work [7]. The remaining larger portion (21.4 quadrillion BTUs) of it was rejected as waste heat. This energy inefficiency is the result of thermodynamic limitations where much of the remaining energy is rejected as waste heat through radiator cooling and exhaust gas. This thermal energy can be utilized as a source to generate useful work to improve an efficiency of the larger process which would be discarded as waste heat with no practical usefulness. In an approach to recover waste heat, the MEMS-based boiler has been presented and its capability to recover waste heat has been explored. Apart from this source of heat, other sectors present are equally suitable to exploit, for example, industrial and residential. The work on renewable energy source itself such as solar thermal energy has already been proposed and published utilizing small-scale device [8].

In addition to thermal recovery, thermal storage can play an important role in thermal energy scavenging and efficiency as well. The thermal storage technique is well established in a solar power plant where the excess heat and/or the captured heat itself is stored temporarily in a thermal storage device. The thermal energy storage (TES) process is then reversed allowing stored heat to be made available to a boiler at the periods of higher energy demand. The steam produced in a boiler is supplied to the generator to produce mechanical or electrical work [9]. The possibilities of storing waste heat utilizing phase change material (PCM) based composites is an interest of this study as well.

1.1 Objective and Thesis Structure

The study pertaining to recovering and storing waste heat is presented in this dissertation. The research work begins with the development of MEMS-based boiler for waste heat scavenging. A low-cost microfabrication technique is integrated with thermal energy recovery technique to scavenge waste heat and generate power for small-scale applications. A microfabrication process utilizes the photolithography technique to manufacture multiple devices from each processing steps with high repeatability, and thus minimizing the overall cost of manufacturing. In addition to this work, the research work also investigates the thermal energy storage technique to utilize the waste thermal energy more efficiently by balancing energy supply and demand. For this, a phase change TES is utilized and several materials constituting to enhance the thermal properties of TES is proposed. The results of the study are illustrated and discussed.

A detailed review of the thermal recovery based on different thermodynamic cycles are presented in Chapter 2. Furthermore, the proposed waste heat scavenging device is explained as well.

A study of a MEMS-based boiler for waste heat scavenging is presented in Chapter 3 and Chapter 4. A detailed design, fabrication, test setup and results are summarized. A computational approach to optimize the Superheater design parameters is presented in Chapter 5. An experimental demonstration of an Exhaust heat recovery utilizing the boiler developed in Chapter 4 is presented in Chapter 6. A detailed design, fabrication, test setup and results are summarized.

A detailed review of the thermal energy storage techniques is presented in Chapter 7. Latent heat storage via phase change of various fabricated composites was investigated to store ambient thermal energy. The material selection, composite fabrication, test setup and results are presented in Chapter 8. Finally, Chapter 9 presents a general conclusion of the study and offers recommendations for future work.

CHAPTER 2

A GENERAL REVIEW OF ENERGY RECOVERY VIA MECHANICAL THERMODYNAMIC CYCLES

2.1 Thermal Energy Recovery

Waste thermal energy refers to energy that is exhausted from the thermodynamic process without being put to practical use. These energies are rejected even though it could still be reused for economic purpose. Waste heat can be discarded at almost any temperature depending on the process. On the basis of temperature, waste heat is categorized as high (>650 °C), medium (230-650 °C) and low (<230 °C) grade thermal energies [3]. The waste heat recovery from high and medium grade thermal energies is more feasible and cost effective with respect to heat quality. This is due to comparatively better work potential or efficiency of converting waste heat (based on Carnot cycle) to another form of energy (such as electrical or mechanical) associated with higher temperature waste heat sources [3]. Even though it is not efficiently utilized, the availability of low-grade thermal energy is relatively abundant. The reason may be the low-efficiency power generation from low-grade heat sources.

The abundance of low temperature waste thermal energy as well as the challenges associated with its recovery demand thorough investigation. In this context, several thermodynamic cycles have been proposed and studied to recover low-grade

heat. They are Kalina cycle, Goswami cycle, organic Rankine cycle, supercritical Rankine cycle, and trilateral flash cycle [10]. The following section presents a brief review on thermodynamic cycles for low-grade heat recovery.

2.1.1 Types of Thermodynamic Cycles for Low-Grade Thermal Energy Conversion

2.1.1.1 Kalina Cycle

The Kalina Cycle was invented by Dr. Alexander Kalina in the late 1970s [11]. It is a thermodynamic process designed to convert low-grade heat into useful work. The Kalina cycle is comprised of two different fluid mixtures with different boiling temperatures. The fluid mixture allows the cycle to operate over a range of temperatures which would not be possible with the single fluid. Typically, a mixture of water and ammonia are widely used due to the non-azeotropic characteristic of the mixture [12]. This characteristic allows us to change composition and temperature during boiling for all possible ratio of ammonia and water mixture. Therefore, the mixture boils and condensate with increasing and decreasing temperature, respectively.

The typical Kalina cycle based system consists of components such as heat recovery vapor generator,vapor separator, recuperative heat exchanger, condenser, and control system. The cycle requires a variation of fluid mixture ratio at different components of the cycle. Therefore, the process is designed to restore specific ammonia concentration at a particular component of the system. For instance, high ammonia concentration at the boiler and lower concentration of ammonia at the condenser. The variation in ammonia concentration allows the process to extract maximum heat from the source and discard maximum heat to the sink. In this way, a high temperature

difference between the source and sink is maintained during the process to increase the overall efficiency of the cycle. The Kalina cycle demonstrates superior efficiency compared to conventional Rankine cycle. The efficiency improvement of about 10 to 20% has been claimed [13].

Despite the aforementioned advantages, the Kalina cycle based system experiences several drawbacks. They are as follows:

- High vapor fraction is required in the boiler which may result in heat exchanger dryness and lowering of the heat transfer rate [14].

- The ammonia is corrosive to metals (steel, Zinc, copper, etc.) requiring frequent maintenance of the system [14].

- High capital building cost due to cycle complexity [14].

2.1.1.2 Goswami Cycle

The Goswami cycle was proposed by Dr. Yogi Goswami in 1998 [14]. The cycle integrates Rankine power cycle with an absorption refrigeration cycle allowing a generation of power and cooling simultaneously in a single thermodynamic cycle. Similar to the Kalina cycle, the Goswami cycle utilizes the advantage of fluid mixture with different boiling points. The mixture of ammonia and water was used as a working fluid at an early stage of research. However, research on several other mixtures such as ammonia-lithium nitrite and ammonia-sodium thiocyanate have been reported to date [15].

In a conventional Goswami cycle, the mixture of fluids is first pressurized. The pressurized mixture is preheated and pumped to the boiler. The mixture is then

partially heated in the boiler. The exiting vapor is purified by condensing water via rectification. The rectified vapor is superheated and then expanded to a temperature below ambient temperature in an expander. In this way, the power output and refrigeration output is obtained in a single cycle. The cycle demonstrates a promising capability of generating power and refrigeration in a single loop, efficient conversion of low-grade heat source, and design flexibility to produce preferred combination of power and cooling outputs [14, 16]. However, Goswami cycle is still under research [14].

2.1.1.3 Trilateral Flash Cycle

The Trilateral Flash cycle is a unique thermodynamic cycle specifically in terms of operation. Unlike other thermodynamic cycles, it does not require working fluid to be vaporized, saturated or superheated to absorb heat. Rather, the cycle avoids boiling part and utilizes working fluid at liquid phase for heat extraction. This allows the process to attain heat transfer with almost perfect thermal matching between the heat source and the working fluid [17, 18]. The power is generated by the two-phase expander. Theoretical studies have shown that the efficiency of Trilateral Flash cycle could be around 14-85% higher than ORC [14]. These studies were performed assuming the adiabatically efficient two-phase expander.

In reality, it is hard to realize a working adiabatically efficient two-phase expander [17, 18]. However, studies performed on the twin screw expander have claimed to achieve adiabatic efficiency of about 50-80% [19, 18]. Despite this advancement, the Trilateral Flash Cycle is still in the technical development stage.

2.1.1.4 Organic Rankine Cycle

The working principle of Organic Rankine cycle (ORC) is similar to the steam powered Rankine cycle (RC). A typical working diagram of ORC is illustrated in Figure 2.1. The working fluid is pumped to the evaporator at certain temperature and pressure where it absorbs thermal energy from the heat source. The fluid evaporates and then the vapor is superheated in the superheater. The superheated vapor is expanded in an expander such as a turbine. The mechanical work out of the turbine is converted to another form of energy such as electricity by a generator. The expanded vapor is cooled by the condenser and the fluid is returned to the evaporator via the pump.

Waste Heat   **Evaporator**   **Condenser**

Pump
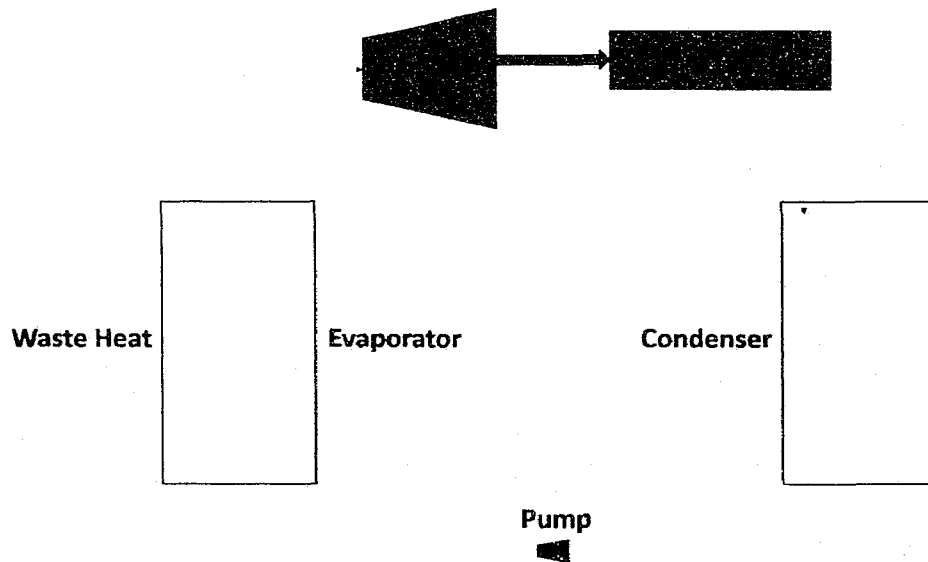
Figure 2.1: A typical Rankine Cycle

The water is replaced with organic fluid as working fluid in the ORC. There are various organic fluids commercially available and can be selected as per the application. The option includes propane, silicon oil, iso-pentane, iso-butane, toluene, haloalkanes,

etc. [14, 10]. These organic fluids have a lower boiling point and high vapor pressure than water which allows the ORC to operate from low-temperature heat source [3]. A suitable fluid can be selected to yield the required throughput depending upon the temperature of operation and the fluid thermodynamic properties.

In addition to lower boiling and higher vapor pressure properties, a molecular weight of the organic fluid is higher than water. The heavier molecular weight allows fluid to flow at a higher mass flow rate to achieve higher turbine efficiency (as high as 80-85%) [3]. Despite these fluid characteristics, the maximum efficiency of the ORC is only about 10-20% [3]. This is due to the operation of a cycle at a low temperature gradient between heat absorption (evaporator) and rejection (condenser). It can be noted from the ORC efficiency that only a small part of the heat is converted to useful work. However, when this efficiency is compared to the theoretical Carnot efficiency of a heat engine working between the low heat source temperature of 423 K and the heat rejection temperature of 298 K. The maximum possible Carnot efficiency is about 30% [3]. The ORC efficiency of 10-20% is a significant amount of the theoretical Carnot efficiency. This makes the ORC suitable for low-temperature heat scavenging. Moreover, the ORC system is simple and requires less maintenance due to the use of a single-stage expander [10].

Among all thermodynamic cycles discussed in this review, ORC is the most commercially matured thermodynamic cycle. The Power plants from large to small scale in term of power outputs are reported in operation [14, 3].

2.1.1.5 Supercritical Rankine Cycle

The working fluid with relatively low critical temperature and pressure are utilized in Supercritical Rankine Cycle. The fluid is directly compressed to the supercritical pressure and then heated to the supercritical temperature before expansion [10]. Therefore, the process does not experience a distinct two-phase change of the working fluid, unlike ORC. This allows the process to attain comparatively better thermal match between the heat absorber (working fluid) and heat source.

Several studies comparing Supercritical Rankine cycle with ORC were performed [10, 20, 21, 22]. The studies claimed that the carbon dioxide powered Supercritical Rankine cycle was efficient in terms of heat transfer from heat source to working fluid than ORC with R123 as a working fluid [20, 21]. In addition to the carbon dioxide as a supercritical working fluid, various organic fluids such as isobutene, propane, propylene, difluoromethane, and R245fa were suggested as well [10]. However, only a few studies on supercritical cycle with organic fluids were performed [10].

The supercritical Rankine cycle has its own drawback despite the efficient heat transfer due to thermal matching. The cycle operates at a high pressure, typically 60-160 bar for a carbon dioxide powered cycle. This may cause difficulty in operation and also may require safety. In addition, the supercritical fluid has a low critical temperature such as 31.1 °C for carbon dioxide [10], and thus condensing an already low-temperature fluid to preferably 24 °C will be a design challenge.

There have been no report of the operational power plant based on Supercritical Rankine cycle until now [14]. It is still in the research stage.

2.1.2 A Proposed MEMS Based Heat Scavenging System

A detailed explanation of the proposed low-grade heat conversion device is presented in this section. Figure 2.2 illustrates the proposed low-grade heat scavenging system [23]. The proposed device basically consists of four interconnected components. They are designated as follows:

- Boiler

- Superheater

- Free Piston Expander (FPE)

- Condenser
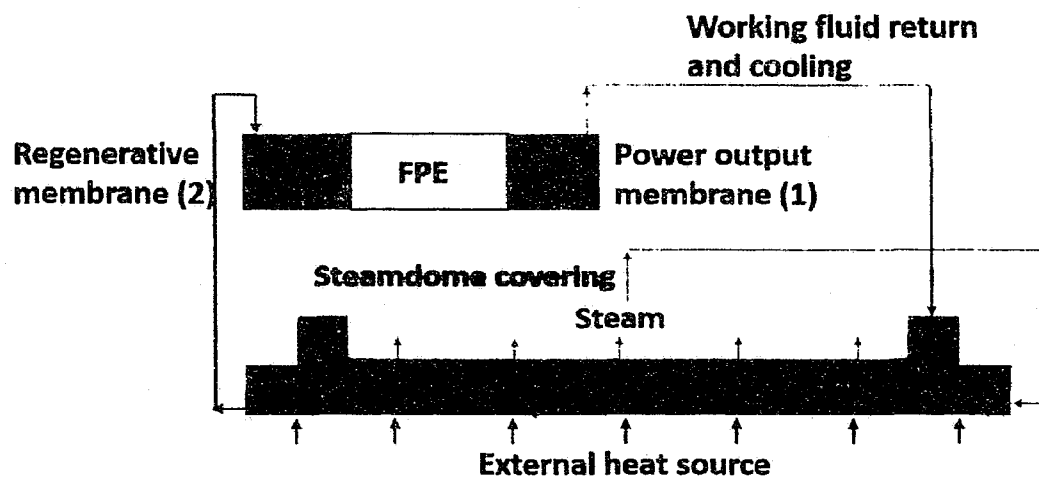
Figure 2.2: The proposed heat recovery system.

The proposed system works on the modified version of the ORC. The pump in an ORC system has been replaced by capillary channels. The channels utilize capillary action by the virtue of surface tension for the fluid flow in the heat exchanger. This cancels out the required pumping work from the cycle efficiency calculation.

The boiler captures waste heat causing phase change of the working fluid from liquid to vapor (Refer to Figure 2.2) [23]. The generated steam is then allowed to traverse through the Superheater. The FPE expands the superheated steam to produce useful work in either mechanical or electrical form. The expanded vapor is then cooled and returned to the boiler. Apart from the low-temperature waste heat, the device is equally suited to explore other renewable sources like solar energy [24].

A detailed progressive study of the boiler, an essential component of the low-grade heat scavenging system, is presented in the following chapter.

CHAPTER 3

PRELIMINARY INVESTIGATION OF A MEMS BASED BOILER WITH STRAIGHT CAPILLARY CHANNEL DESIGN FOR LOW TEMPERATURE WASTE HEAT SCAVENGING[†]

3.1 Introduction

Pressing energy concerns and growing rates of worldwide energy consumption present a need for focused research on thermal energy scavenging and power production from renewable sources. In 2010, the United States consumed 98 quadrillion BTUs (British Thermal Units) of energy [25]. The U.S. Department of Energy has further predicted that global energy consumption will increase by 44% compared to 2006 levels [5]. Of particular concern is the operating efficiency of many standard cycles. The Otto cycle, for example, exhibits an approximate efficiency of 35% [26]. The remaining two-thirds of initial fuel energy are expelled into the surrounding environment as waste thermal energy from either exhaust or heat exchanger devices. This is of particular concern as transportation sources account for nearly 30% of total energy consumed in the U.S. on an annual basis [25]. Other sectors of energy consumption produce large amounts of waste thermal energy as part of their regular operation as well.

[†]This chapter has been reproduced and referenced as Suvhashis, T., Emmanuel, O., Christopher, C. and Leland, W., "MEMS-BOILER OPERATION FROM LOW TEMPERATURE HEAT TRANSFER AND THERMAL SCAVENGING," Micromachines, vol. 3, no. 2, pp. 331-344, 2012.

The work in this paper presents investigations of a unique phase-change based steam system designed to capture waste heat from some of the sources noted previously. The use of this normally wasted energy provides an overall efficiency enhancement for the larger process as a whole. The system is designed around small-scale, microfabricated devices that may operate across the low-temperature gradients commonly associated with waste thermal energy sources. As an added benefit, the devices developed as part of this waste heat scavenging effort are equally well suited to exploit other sources of environmental thermal energy. These include solar thermal sources [8].

Micro-devices and engines have been under investigation by a wide variety of research groups for a number of years. One of the first engines was a micro steam engine constructed by Sandia National Labs in 1993 [27]. Since then, efforts have expanded to include micro steam turbines operating on the Rankine cycle [28, 29]. There has also been interest in micro-engines operating on the Brayton and Wankel cycles [30]. One challenge to many of these approaches has been the nature of high speed rotating components when implemented on the micro scale. High-speed stability and bearing tolerance are among the engineering and fabrication challenges. Nonetheless, progress continues on these unique devices [28]. Other micro-engine concepts have relied on power output that does not yield rotary motion. Work by Weiss *et al.* included a flexing-expander membrane-based device that outputs power via membrane expansion [31, 32]. The device consisted of two membranes, separated by a gasket and filled with working fluid that boils at low temperature. When thermal energy was applied, the working fluid expanded causing membrane expansion and power output. This

device represented a thermodynamically closed operating cycle, where no working fluid crossed the boundaries established by the device's volume. Thermal energy was introduced in discrete applications through the inclusion of a novel thermal switch [33].

This present work investigates the operation of a system in an open thermodynamic cycle. The complete system is shown in Figure 3.1 [23]. In its final form, low-temperature waste heat (or thermal energy from another source) is consumed by the system boiler where working fluid transitions from liquid to vapor. The resulting pressurized vapor is expanded by a unique Free Piston Expander (FPE) to produce the work output from the system. Expanded working fluid is cooled via a heat exchanger and then returned to the boiler for reuse. In this manner, the system represents a modified Rankine Cycle which lacks the typical rotary expansion and high operating temperature.
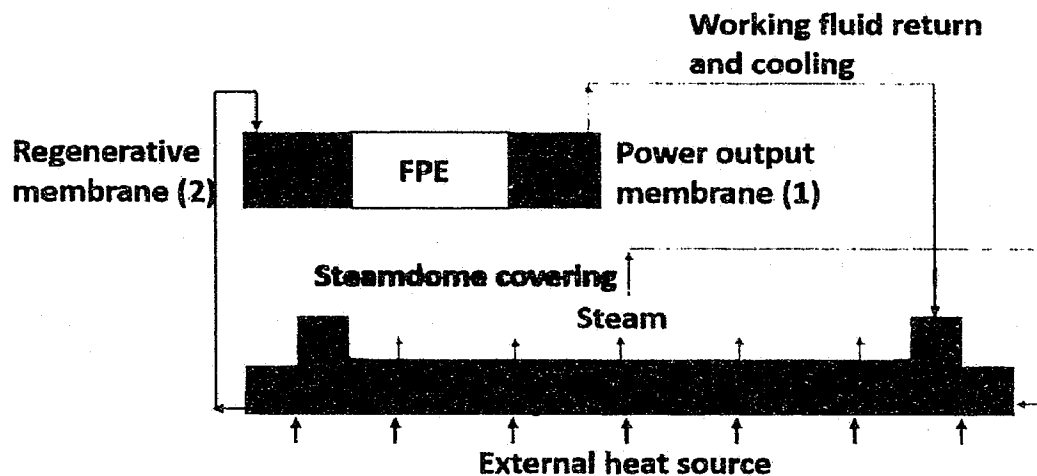
Figure 3.1: The proposed heat recovery system.

The boiler and FPE are uniquely designed components of this system. The FPE has been modeled and discussed in previously published work [34]. The free piston (noted as FPE in Figure 3.1) slides linearly within a bore based on input pressure from the system's boiler. As the piston slides, it expands the working fluid and pressurizes the primary power output's membrane. Once fully expanded, the vapor is released to the cooling line and the piston begins its return to the starting position. The return is driven by energy stored within the primary membrane. The secondary, regenerative membrane helps absorb piston energy during the return stroke and aids in the overall efficiency of the system through this unique regenerative capture. The action of the membranes constitutes the system's power output and is designed to produce either mechanical or electrical power. Electrical power may be created through the actuation of an external PZT cantilever or similar device. Mechanical power output is achievable through direct membrane mechanical action.

The boiler is the particular focus of this present work. Like the FPE, the boiler is a unique design for a low-temperature application. The design focuses on the ability to generate working fluid pressure with minimal moving parts or components common to large-scale steam systems or true Rankine cycle devices on the microscale. This paper represents the first time a boiler of this type has been produced via MEMS techniques and operated at pressurized conditions. The operation of the boiler is dependent on the capillary action of the working fluid across the heated lower surface as noted in Figure 3.1. This capillary action is based on the microfabrication of capillary channels that take the working fluid from the surrounding fluid reservoirs, providing a continuous source of working fluid supply to the heated surface. The

top of the boiler is enclosed with a steamdome to provide a central collection point for vaporized working fluid. From the steamdome, the pressurized working fluid is available to devices like the FPE in the final assembly of the overall system.

The overall approach to this low-temperature energy challenge has several advantages including ease of fabrication due to the lack of high-speed bearings or rotating parts. The operation of the device at temperatures typical of environmentally scavenged waste heat allows a wide degree of flexibility in material selection as well. The remainder of this work discusses the fabrication and characterization of the boiler. Reported testing considers variations like channel dimension, power input, a temperature of operation, and generated working fluid pressure and fluid flows.

3.2 Research Objectives

This chapter presents the preliminary investigation of a MEMS based microboiler which is an essential component of the small-scale scavenging system. The work presented in this chapter is focused on the boiler's development area. There were four objectives of this study. They are listed below:

- Fabricate the boiler system based on capillaries to drive the working fluid flow.

- Select input power to the boiler based on real-world waste heat sources.

- Evaluate the working fluid flow rate for each boiler given four different capillary channel heights (50 μm, 100 μm, 150 μm, and 170 μm).

- Characterize the boiler operation under full pressurization including temperature, pressure, and working fluid flow rates.

Research objectives were achieved and presented throughout this paper for each stated point. The boiler consisted of two components: 1) a microfabricated boilerplate with capillary channels and 2) an acrylic steamdome. Each component was fabricated separately. The silicon was etched to form micro channels with constant 100 μm width and varying depth. The boilerplates with four different channel depths were microfabricated. The steamdome was fabricated using a casting technique. Each fabricated component was epoxied together to form the boiler. In this way, four boilers with different channel dimensions were readied for further experimental setup. Several components such as thermocouple, pressure sensor, resistance heater, and inlet and exit tubing were added to the boiler to make it fully functional for testing.

A number of tests were performed on the boiler's experimental setup to study and characterize its operation. First, the capability of different capillary channels to flow the fluid from the reservoir to the heated surface were studied. These tests provided a maximum mass flow rate for each boiler. Based on the results, a boiler with a maximum mass flow rate was chosen for further pressurized operation. In pressurized operation, the exit of the boiler was restricted and the working fluid flow rate was altered to achieve the steady state pressure. Pressure along with corresponding temperature data were recorded and analyzed.

3.3 Experimental Materials and Method

3.3.1 Fabrication

The boiler consisted of two components, a silicon etched boilerplate and an acrylic covering steamdome. Each component was fabricated separately and glued

together to form the boiler. The fabricated boiler was approximately 13 mm in width by 38 mm in length by 10 mm in height. Four different 100 μm wide straight channel with depths 57 μm, 100 μm, 150 μm, and 170 μm were considered to study the effect of varying depth on the capillary flow rate for this work. The overall dimension of the boilerplate was kept constant to 13 mm in width and 38 mm in length independent of the channel's depth.

A photolithographic mask for each channel depth was designed using L-edit software and printed. A standard 4-inch type $<100>$ silicon wafer served as a substrate for boilerplate fabrication. An Inductive Coupled Plasma (ICP) etching technique was utilized to etch silicon and form channels and reservoirs in the boilerplate. The etch time was approximately 2 to 3 $\frac{\mu m}{min}$ at constant ICP power supply. The etching time increased with an increase in channel depth based on the etch rate. A photoresist was used as an etch resistant mask for the channel depth below 100 μm as it required shorter exposure time to the ionized gas inside the ICP etch chamber. However, a thin chrome layer of approximately 200 nm was utilized as an etch mask for the channel depth above 100 μm. S1813, a positive type photoresist, was considered for this work.

Beginning with a 57 μm deep channel fabrication, a silicon wafer was cleaned using acetone to remove any organic particles present on the wafer's surface. The wafer was then immediately soaked in isopropyl alcohol (IPA) to remove any stains left by acetone. After stain removing, the wafer was rinsed well with deionized water and blown dry with a nitrogen stream. The cleaned wafer was dehydrated by heating the wafer in a hotplate at 200 °C for about 20 minutes. This dehydration step will

facilitate better adhesion of the photoresist to the wafer's surface. The dehydrated wafer was spin coated at a maximum spinning speed of 3000 revolutions per minute (RPM) to form a 1 μm thick layer of photoresist atop the wafer. The coated wafer was soft baked in a hotplate at 115 °C for about 90 seconds to vaporize the liquid present in the photoresist. This will improve bonding between the photoresist molecules itself and to the wafer's surface as well. The soft baked wafer was exposed to ultra violet (UV) rays through the mask using photolithographic mask aligner. The mask was designed to allow UV light to pass through the channel and reservoir features. The exposed portion of the photoresist through the mask became soluble in the developer due to the change in molecular structure. The exposed wafer was then soaked in an MF-319 developer for 30 seconds to strip off the soluble portion of the photoresist atop the silicon leaving imprints of channels running between the two reservoirs. The wafer was etched to strip off the silicon to form 57 μm channels and reservoirs in the wafer.

Similar fabrication steps were followed for all deeper channel boilerplates, however, a 200 nm thick chrome was E-beam evaporated on one side of the silicon wafer. This thin metallic layer provided an extra layer of etch resistant mask to withstand the longer period of etching time required to form deeper channels. The chrome coated wafer was cleaned, dehydrated, exposed and developed. After the removal of exposed photoresist, an additional step of chrome removal was carried out. The developed wafer was soaked in a chrome etchant. This stripped off the exposed chrome at the channels and reservoirs. The silicon was then etched to form boilerplate with varying depth features. After the wafers were etched, each individual boilerplate

was diced separating it from the wafer. Figure 3.2 shows a boilerplate with 100 μm deep channels running between the working fluid reservoirs [35].
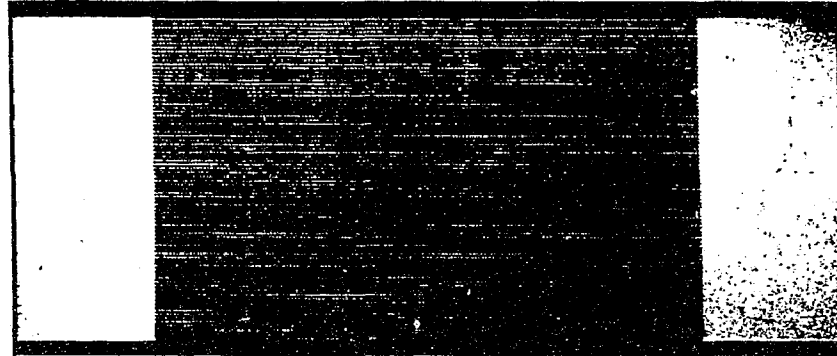
Figure 3.2: Boilerplate.

After the fabrication of the boilerplates, the steamdome was fabricated using a casting technique. A 10 mm thick acrylic board was cut to obtain an acrylic piece of 13 mm by 38 mm. The cut piece was drilled leaving 3 mm thick outer walls along the perimeter of the steamdome, and 3 mm thick inner walls separating two reservoirs from the central steam collecting dome. This produced separate space for reservoirs and steam collecting dome. A rubber mold was created using this acrylic cast. A two-part liquid resin from Alumilite Corporation was mixed in an equal ratio by weight and poured into the mold. The liquid resin was then left to cure for approximately 12 hours to form a rigid resin steamdome. The cured steadome was removed from the mold and epoxied to the boilerplate. Figure 3.3 shows the epoxied steamdome and the boilerplate together [35].
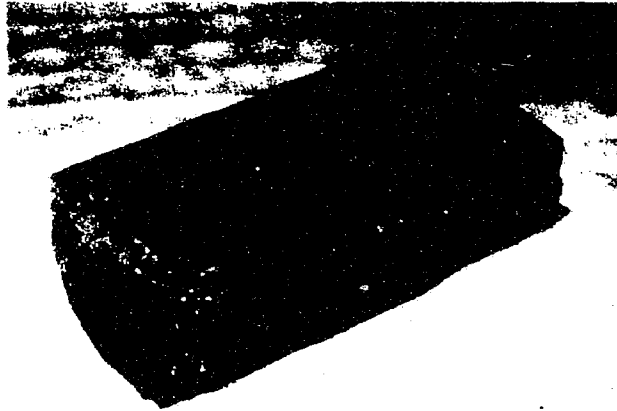
Figure 3.3: Boiler.

A 0.0625-inch hole was drilled atop each reservoir for the input of the working fluid. A 0.125-inch hole was drilled atop the central steam collecting dome for the vapor to exit. Additionally, a tiny hole was drilled next to the exit hole to include a temperature sensor.

3.3.2 Experimental Setup

Separately, a fabricated boiler and steamdome were glued together to form enclosed volume for reservoirs and a chamber for collecting steam. This readied the boiler for a further test setup. A brass nipple fitting from McMaster-Carr was partly inserted in the previously drilled 0.125-inch hole atop the central steam collecting chamber. A 'T' shaped tubing of dimensions 396 mm by 396 mm by 396 mm was tightly fitted to the brass nipple to avoid any leakage of phase changed working fluid. A pressure sensor type PMC No. 60 from Precision-Measurement CO was fitted to one end of the 'T' tubing for the pressure measurement and a 0.8 cm long micro-sized

tubing from IDEX Health & Science LLC was glued to the other end. This tubing served as an exit to the boiler.

A resistance heater type KHLV-101/P from Omega Engineering INC was attached at the bottom of the boiler to serve as a heat source. The heater was connected to the power supply from BK Precision facilitated with voltage and current read outputs. Two K-type thermocouples were added to the boiler to monitor vapor temperature in the steam collecting chamber and the heat source temperature. Micro tubing was inserted into the reservoir through the inlet hole for the fluid feed to the boiler. The working fluid was supplied via a syringe pump to avoid temperature fluctuation caused by unpredictable manual supply. All the sensors were connected to the computer via NI LabView SignalExpress software to automate reading from the boiler. A fully functional boiler setup with all the added components is shown in Figure 3.4 [35].
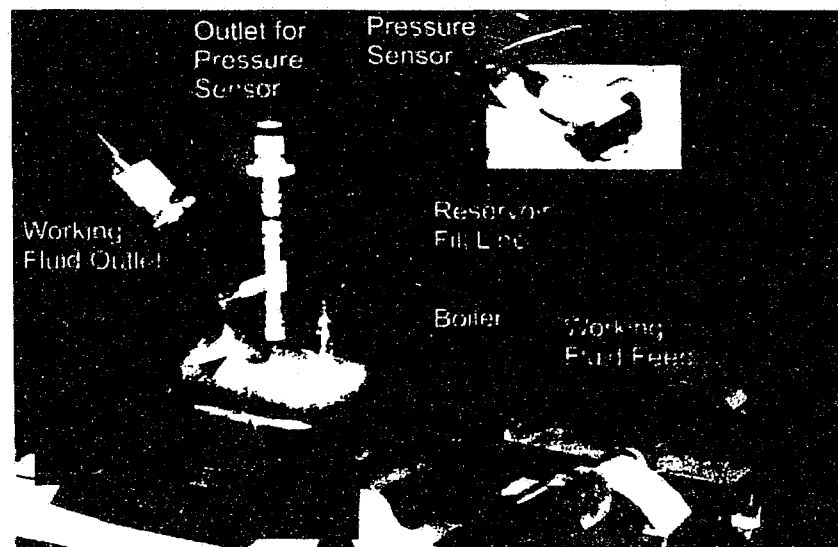
Figure 3.4: Boiler test setup.

HFE-7200 from 3M^{TM} was chosen as a working fluid because of its numerous advantages. The advantage includes high wettability, high heat of vaporization and low environmental impact [36]. In addition to these properties, HFE-7200 has the boiling temperature of 76 °C favorable for this study. After the section of the working fluid, testing was performed on the boiler. A detailed experimental procedure performed on the boiler is explained below.

First, two power inputs of 2.6 W and 3.6 W were selected for the study. These power were chosen by monitoring the heater temperature and comparing it to the real-world waste heat source temperature. For instance, an exhaust gas temperature from a four cylinder four stroke diesel engine ranges approximately from 310 °C to 450 °C [37]. Based on the available temperature range, two different power inputs to the boiler were selected. A series of tests was performed on the variously constructed boilers for each power inputs.

Two different tests designated as Atmospheric Test and Pressurized Tests were performed on the boiler. Temperature, pressure, and fluid flow data were monitored for each experiment. A detail explanation of each test is given below:

- **Atmospheric Test:** The power input of 2.6 W was supplied to the resistance heater. The boiler was allowed to heat up for approximately 15 minutes. This initial warm up ensured the boiler was dry and ready to accept the working fluid. The fluid was supplied to the boiler via syringe pump. The outlet micro tubing attached to the 'T' shaped tubed was left open allowing the boiler to operate at atmospheric pressure.

Initially, the boiler was over supplied with working fluid and the temperature curves of the vapor inside the steamdome and the power source were visually inspected. Based on the internal steamdome temperature, the working fluid feed rate was reduced until a steady state temperature profile was achieved. For each boiler type, capillary flow rates were noted. Similarly, the experiments were repeated for 3.6 W power input. With known capillary mass flow rates for both power inputs, the boiler's ability to pump fluid out of it was studied. This study will allow evaluating the power absorbed by the boiler to phase change the fluid. Beginning with 2.6 W, the boiler was initially heated for about 15 minutes and then the known fluid feed rate was supplied. The phase changed fluid exiting out of the boiler was collected in a syringe for about 4 minutes. The syringe was placed in an ice bath to allow condensation of the entering vaporized fluid. The collected working fluid mass in the syringe was then weighed. The measured mass was divided by a time duration of 4 minutes, in this case, to calculate the mass flow rate out of the boiler. This mass flow rate ($\dot{m}$) was combined with the known heat of vaporization (ΔH_v) of HFE-7200 fluid to determine power absorption via phase change of the working fluid (q) using Equation 3.1. The mass flow rate for each boiler types was noted. Similarly, the tests were repeated for 3.6 power input. Based on q, the boiler with maximum heat absorption was selected for Pressurized Test:

$$q = \dot{m} * \Delta H_v. \qquad (3.1)$$

- **Pressurized Test:** As mentioned in the Atmospheric Test, a boiler with comparatively higher q value was selected for this test. A power input of 3.6 W was supplied to the resistance heater and the boiler was heated to attain a steady state. The noted fluid feed rate from the Atmospheric Test was supplied to the boiler; however, the outlet of the boiler was obstructed using a clamp to allow the boiler to operate at pressurized conditions. The temperature and pressure real-time data were visually inspected. The feed rate was minimized to attain steady pressure and temperature data. In this fashion, a number of operating pressure and its matching fluid feed rate were noted.

3.3.3 Experimental Error

The error associated with the test data were evaluated using Kline and McClintock's uncertainty analysis [38]. The error associated with the voltage and the current readings were $\pm$ 0.1 V and $\pm$ 0.001 amp, respectively. The error associated with each power input was ± 9 mV. The error associated with the pressure reading was $\pm$ 0.5 kPa. The error associated with temperature, mass of the fluid and time were on the order of $\pm$ 0.5 °C, $\pm$ 0.005 g and $\pm$ 1 second, respectively. The error associated with each individual evaporation rate was determined to be in the order of $\pm$ 0.56 $\frac{mg}{s}$.

3.4 Results and Discussion

Experiments were performed on the individual fabricated boiler as mentioned in Section 3.2.2 to evaluate the ability of the capillary channel to the drive fluid across the heated surface, the operating pressure of the boiler and the steamdome internal

temperature. Based on these recorded data, a performance of the individual boiler was characterized.

As stated, the Atmospheric Test was conducted on each boiler with power inputs of 2.6 W and 3.6 W. The boiler was first initially heated for about 15 minutes and the working fluid was supplied to the boiler via a syringe pump connected to the inlet micro tubing. The boiler was allowed to operate at atmospheric pressure. Figure 3.5 shows the typical temperature profile of the heat source and the vapor inside the steamdome [35].
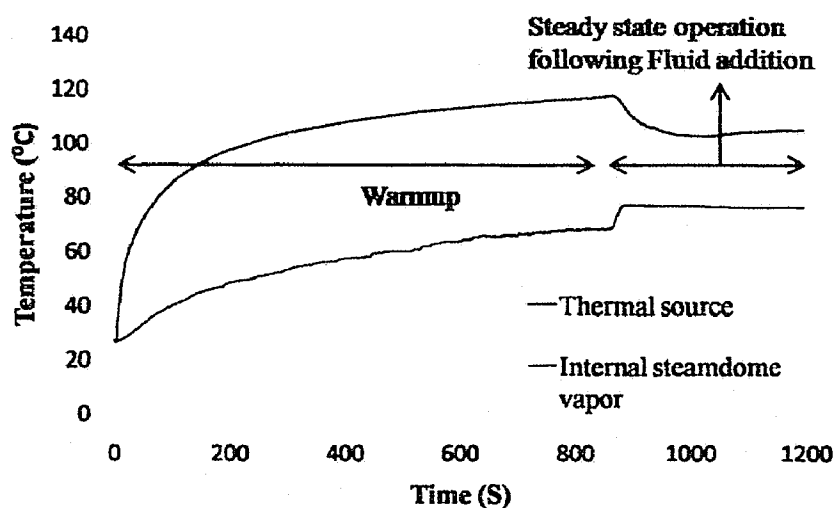
Figure 3.5: A typical temperature profile of the boiler.

Figure 3.5 demonstrates the initial heating of the boiler for approximately 15 minutes and following 4 minutes fluid addition. The capillary flow rates were noted for 57 μm, 100 μm, 150 μm, and 170 μm boiler with a power input of 2.6 W and 3.6 W. In addition to the capillary flow rates, the source temperature, steamdome internal

vapor temperature and output mass for an individual boiler were recorded as well. These recorded data for each boiler is summarized in Table 3.1 and Table 3.2 [35].

Table 3.1: Atmospheric Test at 2.6 W thermal input.

Channel Depth (μm)	Source Temperture (°C)	Steamdome Vapor Temprature (°C)	Mass Flow Rate (mg/s)
57	94.2	74.3	4.53
100	106.9	74.8	4.56
150	101.5	75.8	4.61
170	103.4	76.2	4.61

Table 3.2: Atmospheric Test at 3.6 W thermal input.

Channel Depth (μm)	Source Temperture (°C)	Steamdome Vapor Temprature (°C)	Mass Flow Rate (mg/s)
57	115.3	74.3	8.86
100	121.6	74.8	10.66
150	116.2	75.8	11.47
170	120.5	76.2	12.26

The recorded data demonstrated an average working fluid boiling temperature of 76 °C and this coincides with the boiling temperature of HFE-7200. Furthermore, the boiler demonstrated an increased mass flow rate as the channel depth increased. For the power supply of 2.6 W, the flow rate increased by 1.7% when the channel height increased from 57 μm to 170 μm. Similarly for the power input of 3.6 W, the flow rate increased by 28%. The boiler with the higher channel depth presented comparatively a higher fluid flow rate resulting in increased phase transformation rate. These recorded flow rates were consistent with the modeling and experimental activities conducted by Kim et al. on other devices [39]. Figure 3.6 shows the effect of the channel's depth on the mass flow rate [35].
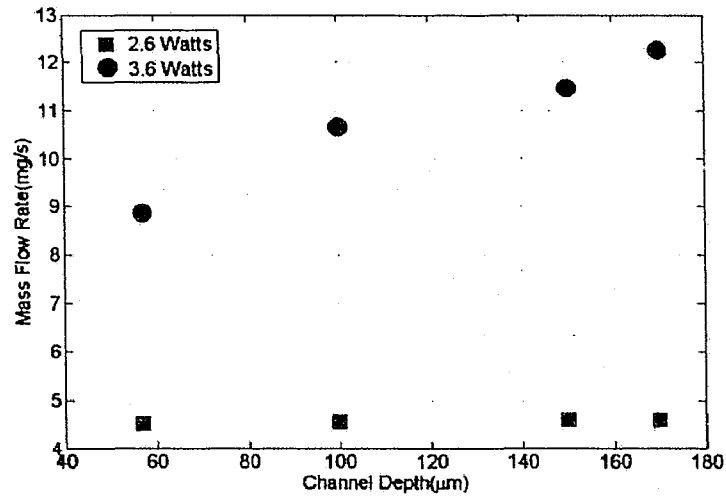
Figure 3.6: Channel depth versus average mass flow.

With the mass output flow rate known, the energy via phase change of the working fluid was calculated using Equation 3.1. Table 3.3 and Table 3.4 summarizes the energy absorbed by the boiler with 57 μm and 170 μm channel depth for given power inputs of 2.6 W and 3.6 W.

Table 3.3: Energy absorption at 2.6 W thermal input.

Channel Depth (μm)	Mass Flow Rate (mg/s)	Heat of Vaporization (Kj/Kg)	Energy Absorption (W)
57	4.53	125	0.57
170	4.61	125	0.58

Table 3.4: Energy absorption at 3.6 W thermal input.

Channel Depth (μm)	Mass Flow Rate (mg/s)	Heat of Vaporization (Kj/Kg)	Energy Absorption (W)
57	8.86	125	1.11
170	12.26	125	1.53

Energy absorbed by 57 μm and 170 μm channel depth boilers via phase change of the working fluid were 0.57 W and 0.58 W, respectively. These energy absorption values amplified with the higher power supply of 3.6 W. Energy absorption were 1.11 W and 1.53 W for 57 μm and 170 μm channel depth boilers, respectively. Although the power conversion rate elevated from 0.58 W to 1.53 W as the input power was increased from 2.6 W to 3.6 W for the 170 μm channel depth boiler, energy conversion via phase transformation was 42.5% of the total power supplied. This low energy absorption revealed poor energy conversion efficiency by the boiler. The reason is the larger volume of the steamdome. The steamdome's wall acted as a heat sink itself. The steamdome's average wall temperature was below the boiling temperature of the working fluid of 76 °C causing premature condensation of the vapor at the walls of the steamdome. This effect seems to be reduced in the case of higher power input of 3.6 W, however, the steamdome heat sink effect still dominates.

Following the Atmospheric Test, 170 μm channel depth boiler was selected for the Pressurized Test. The Pressurized Test was conducted on the boiler with 3.6 W input power. The boiler was initially heated for about 15 minutes and the working fluid was supplied via syringe pump. Based on the established flow rates from the Atmospheric Test for 170 μm channel depth boiler, the fluid was supplied without placing a restriction on the outlet tubing. The exit of the boiler was then restricted to generate the pressure inside the boiler. The mass feed rate to the boiler was adjusted to match the restricted flow out of the boiler. This was visually verified by inspecting the internal steamdome's vapor temperature and pressure data. Sets of developed pressure and associated temperature of the vapor were recorded. The

maximum operating pressure was 229.30 Pa. Table 3.5 summarizes the developed pressure and associated temperature of the vapor as the degree of restriction were increased.

Table 3.5: Pressurized Test at 3.6 W thermal input.

Channel Depth (μm)	Steamdome Vapor Temperture (°C)	Mass Flow Rate (mg/s)	Pressure (Pa)	3M®Pressure (kPa)
170	75.5	12.3	0g	0g
170	76.3	10.8	19.30	0.99
170	76.7	8.6	55.0	2.3
170	78.3	5.4	229.30	7.65

The results obtained from the tests demonstrated interesting trends and operating characteristics. The vapor temperature increased with the increase in operating pressure. This can be visualized graphically in Figure 3.7 [35]. The vapor temperature profile inside the steamdome followed the increasing operating pressure. This verified that the internal operating condition of the boiler as a saturated environment. For the maximum operating pressure of 229 Pa given a mass flow rate of 5.4 mg/s, the saturation temperature of the vapor elevated to 78.7 °C. In Figure 3.7, although the maximum pressure achieved for the test was 275 Pa, it is not considered as a steady state point for true reporting.
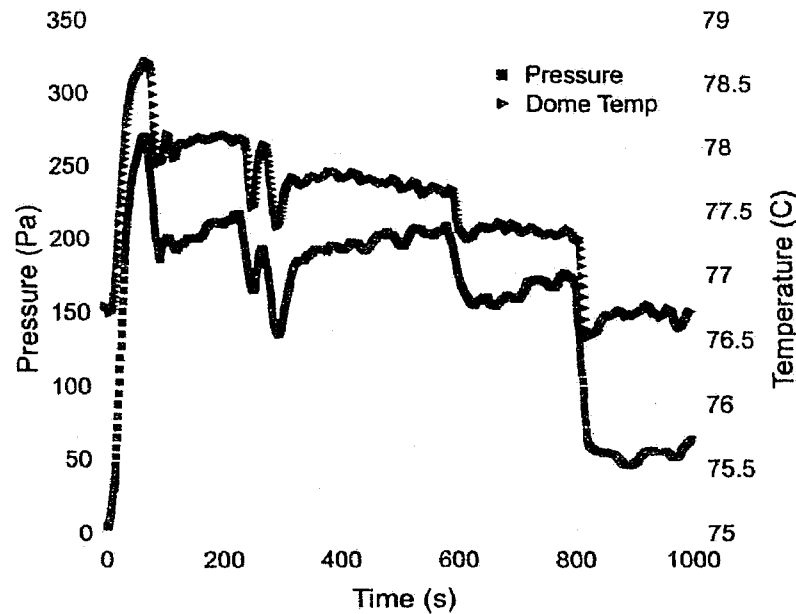
Figure 3.7: Pressure and temperature profile.

Similar to Atmospheric testing, the Pressurized Test was hampered by the steamdome heat sink effect. Future study will be focused on improving both pressure and mass flow rate of the boiler. This includes minimizing the heat sink effect of the steamdome. One way to achieve this is by reducing the steamdome volume.

3.5 Conclusion

The boiler presented is designed to capture waste heat from various real-world sources and to convert it into useful energy. A boiler consisted of a boilerplate and a steamdome epoxied together. The boilerplate was designed with micro capillary channels to drive the working fluid from reservoir to heated surface. Four boilerplates with 57 μm, 100 μm, 150 μm, and 170 μm capillary channel depth were fabricated

using microfabrication technology. Tests were conducted to evaluate the fluid flow rates, operating pressure and temperatures of these boilers.

In atmospheric testing, the maximum mass flow rate was 12.26 $\frac{mg}{s}$ demonstrated by the 170 μm channel depth boiler for the given 3.6 W power supply. This is an improvement of 28% compared to 57 μm depth capillary channel. The maximum power consumed via phase transformation of working fluid was 1.53 W. Based on these results, the 170 μm channel depth boiler was selected for pressurized testing. The Pressurized Test was conducted at a pressure ranging from atmospheric to 229 Pa. Mass flow rates were varied to match the operating pressure of the boiler, ranging from 12.26 $\frac{mg}{s}$ at atmospheric pressure to 5.4 $\frac{mg}{s}$ at 229 Pa.

Results from the tests indicated opportunities for improvement. The use of larger dimensions for a steamdome resulted in a significant cold surface for condensation within the boiler itself. As a result, mass transfer rate and the operating pressure were hampered. Future work will be focused on enhancing the mass flow rate and operating pressure. Minimizing steamdome volume is one effective way to achieve this.

CHAPTER 4

INVESTIGATION OF A MEMS BASED BOILER WITH UPGRADED MICRO RADIAL CHANNEL FOR LOW TEMPERATURE WASTE HEAT RECOVERY[†]

4.1 Motivation

In recent years, there has been increasing interest in the development of micro-devices and engines to recover waste heat. The reason is its free availability as well as abundance. Such availability is due to the inevitable losses associated with thermodynamically limited processes. In a typical Otto cycle, for instance, out of the total energy consumed by the system, only one-third of the energy is converted into useful work and the rest is discharged to the surrounding as a waste heat [1]. For a spark ignition, a 1.4-liter internal combustion engine (ICE) with the thermal efficiency of 15% to 32%, energy lost through the radiator is 1.7 kW to 45 kW and through exhaust gas it is 4.6 kW to 120 kW [1, 2]. Likewise in industries, the estimated losses are in the range of 20% to 50% [3]. These losses could be minimized either by improving the efficiency of the system itself or via the installation of secondary waste heat recovery system. The recovery system uses the losses to generate mechanical or

electrical work to enhance the efficiency of the primary system [4]. Such notion of heat recovery is utilized by the microdevice presented in this paper.

4.2 Related Research

The possibility of heat recovery using a microdevice was first validated by Muntz *et al.* in 1991 [40]. The study presented attractive characteristics of a pressure driven microdevice for power generation. Furthermore, the author noted that the pressure driven microdevices required additional study. Since then, several different microscale dynamic heat engine types have been investigated for waste heat recovery. Those are micro-sized gas turbines [41, 42] and rotary engines [28, 30], free piston engines [43, 44], and membrane type actuators for power generation [45]. The Brayton cycle based gas turbine was first proposed by Episein *et al.* Anticipated micro-device consisted of eight microscale components to fabricate the fully functional system. The power production by this device was calculated to be in the range of 10-100 W [42]. In recognition of this work, several other researchers initiated the investigation of rotatory parts for power generation based on Rankine cycle steam engines [28, 46, 29]. The steam engines were further tailored to operate from low temperature waste heat sources by utilizing low boiling point refrigerants [47, 48, 49]. These micro-devices were called organic Rankine cycle (ORC) steam engines. The ORC based engines were comparatively less complex in design and more economical in terms of cost and maintenance [50]. A Wankel-type ORC engine with rotatory design was studied as well [51].

Apart from rotary engines, free piston Sterling engines were also investigated [52]. Metha *et al.* presented a comparison of a Sterling engine for waste heat recovery using two different ORC working fluids [37]. Similarly, performance of the low temperature solar powered differential Sterling engine was also investigated. The study indicated a potentially attractive future low temperature engine [53]. In contrast to rotating and sliding engines, Washington State University introduced a P3 heat engine for power generation [45, 31]. The engine was heated by an external heat source causing phase transformation of the working fluid to gas. The expansion of the fluid deflected the piezoelectric film attached to the silicon membrane producing power. Similar to this, Saturation Phase-change Internal Carnot Engine (SPICE) was studied as well [54]. With consideration of all these efforts in development of microdevices and engines for waste heat recovery, a system capable of scavenging waste heat is presented in this paper.

4.3 Background

The system currently under investigation consists of three components: 1) boiler, 2) free piston expander (FPE), and 3) Superheater. Figure 4.1 shows the ORC system in completion. The boiler is the particular emphasis of the work presented. The boiler consists of microfabricated capillary channels and steamdome. The capillary channel provides continuous supply of the fluid to the heated areas via capillary action, which would otherwise only be possible using a pump. The boilerplate captures the waste heat initiating phase change of the working fluid to vapor. The resulting steam traverses the Superheater beneath the boiler. The pressurized superheated steam

is then introduced to the FPE unit. The FPE constitutes the power output from the system and may produce either mechanical or electrical output depending on construction and need [34, 55]. Following expansion in the FPE, the working fluid is cooled and returns to the boiler.
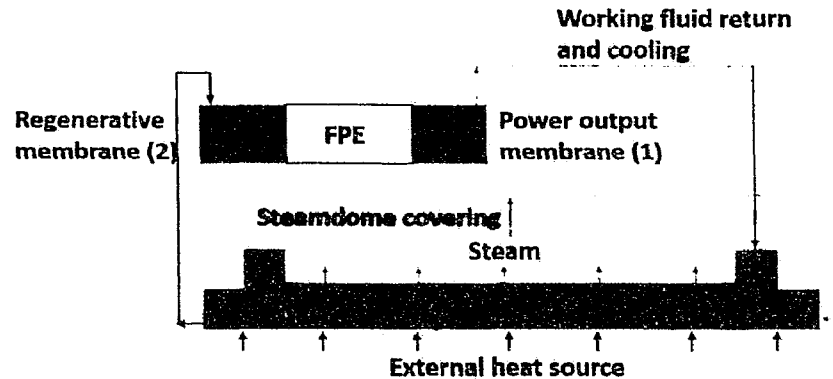
Figure 4.1: A waste heat scavenging system: the heat source, the steamdome covering, the boilerplate, the free piston expander, and the Superheater.

The work presented in this paper is focused on the microscale boiler development area. The design and the microfabrication techniques utilized to manufacture the boiler are explained. The detailed experimental plans and results obtained from the fabricated boiler are discussed in the following sections.

4.4 Research Objectives

The work presented in this chapter is focused on the boiler development area. There were four objectives to this study:

- Fabricate the boiler system based on capillaries to drive the working fluid flow.

- Evaluate the working fluid flow rate for different power inputs via modeling.

- Characterize the boiler operation under full pressurization including temperature, pressure, and working fluid flow rates.

- Thermodynamically analyze the boiler/Superheater working fluid condition.

Research objectives were achieved and presented throughout this paper for each stated point. In general, the boiler consisted of a microfabricated steamdome and a boilerplate with capillary channels. The silicon was etched using Induced Couple Plasma (ICP) to form the micro channels. Each microfabricated parts were anodically boned together to form the boiler. Thermal model was designed utilizing the structure of the fabricated capillary channels and the maximum fluid flow rate through the channels due to evaporation of the fluid was evaluated. The evaluated mass flow rate served as a baseline for the experimental tests. After evaluating the flow rate and experimentally verifying it, the pressurized characterization of the boiler as noted in the research goal was performed. The exit of the boiler was restricted and the working fluid flow rate was altered to achieve the steady state pressure. Pressure along with the corresponding flow rate was recorded and analyzed.

In-house built serpentine shaped copper Superheater was attached to the boiler's exit. This allowed exiting vapor to traverse through the Superheater and elevate its temperature. The corresponding temperatures were noted for different operating pressure. The data was then interpolated utilizing HFE-7200 thermodynamic table provided by $3M^{TM}$. In this way, the T-s diagram for HFE-7200 fluid was plotted.

4.5 Experimental Materials and Method

The microboiler tested and characterized in this work was based on the design of multiple capillary channels that accessed working fluid reservoirs. The channels transported fluid across the heated boilerplate surface where phase change was initiated. Once boiled, the working fluid was collected in a central steamdome with a single outlet. In real-world operation, the outlet can be connected to other small-scale devices like a mechanical expander for final power output and delivery [34, 55]. Figure 4.2 shows the basic operation and arrangement of the microboiler.
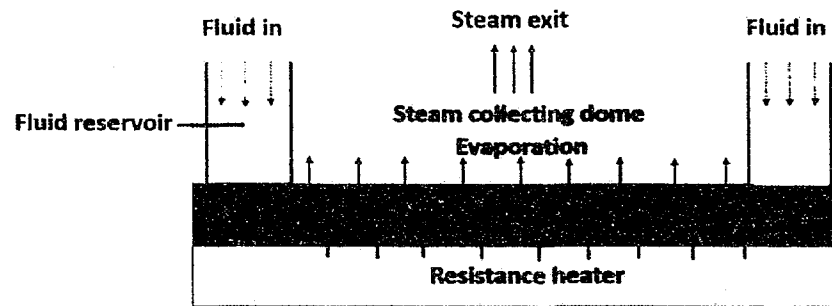
Figure 4.2: Working demonstration of the waste heat scavenging system.

Capillary channels themselves were designed based on prior experimental work [35, 36, 56] as well as expectations from open channel models [36, 57]. Two components were brought together to form the boiler. The boiler design consisted of 1) a boilerplate base with radially separated capillary channels and 2) a steam collecting dome. The overall dimension of the boiler was 35 mm by 35 mm by 1 mm. Photolithographic masks were designed for each microboiler part to transform the design into the working prototype (see Figure 4.3). A third and final mask was designed to etch inlet and outlet holes into the steamdome top. This avoided the need for any manual drill use.

Each part was fabricated independently and then assembled. Additional components were then added to allow for full characterization of the completed boiler.
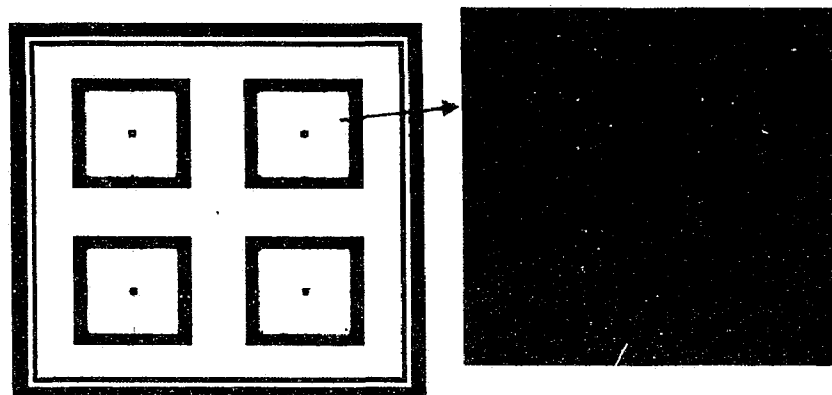
Figure 4.3: Boilerplate mask with an enlarged view of the boiler channel design.

4.5.1 Fabrication

A 4 inch type $< 100 >$ silicon wafer was utilized to fabricate the base boilerplate. First, 200 nm thick aluminum was coated on one side of the wafer. This coating served as an etch stop in subsequent fabrication steps. The aluminum was then spin-coated with S1813 photoresist (PR) and soft baked at 115 °C. The soft baked wafer was exposed and developed using MF-319 developer for about 30 seconds. The developed wafer was then soaked in an aluminum etchant. The aluminum at the photolithographic exposed area was then stripped leaving silicon features beneath. ICP (Ion Couple Plasma) etching was performed on the silicon features to yield channels and the surrounding reservoirs. The depth and width of the capillary channels were 190 μm and 100 μm , respectively. An image of one such fabricated boilerplate is shown in Figure 4.4.

Figure 4.4: ICP etched boiler plate with a SEM image showcasing the enlarged channels.

After the fabrication of the boilerplate, a glass wafer of similar dimensions to the silicon wafer was selected for the steamdome fabrication. The glass was preferred as a material of fabrication because of its insulating properties. The glass also represented significant mass reduction as compared to prior work [35, 56]. This reduced the steamdome thermal impact as part of boiler operation.

The glass wafer was coated with double layers of gold (2000 $\overset{\circ}{A}$) atop a chrome layer (200 $\overset{\circ}{A}$) on both sides of the wafer. This coating served as the etch stop for later processing steps, similar to the aluminum coating in boilerplate fabrication. The wafer was spin-coated with S1813 PR on both sides and soft baked for about 90 seconds at 115 °C. The soft baked wafer was exposed and developed to form the gold-chrome covered steamdome features on the front side of the glass wafer. The back side of the glass wafer was aligned with the front side using the back side alignment (BSA) technique to form the inlet and the outlet holes. The aligned back side of the wafer was exposed and developed. The wafer was then soaked in gold and chrome etchant to remove the gold-chrome layer on the exposed surface. Finally, glass features that defined the specific shape and design of the steamdome were etched using an

aqueous solution of hydrofluoric acid with an etch rate of 5 $\frac{\mu m}{min}$. A diagram of the final steamdome design is shown in Figure 4.5.
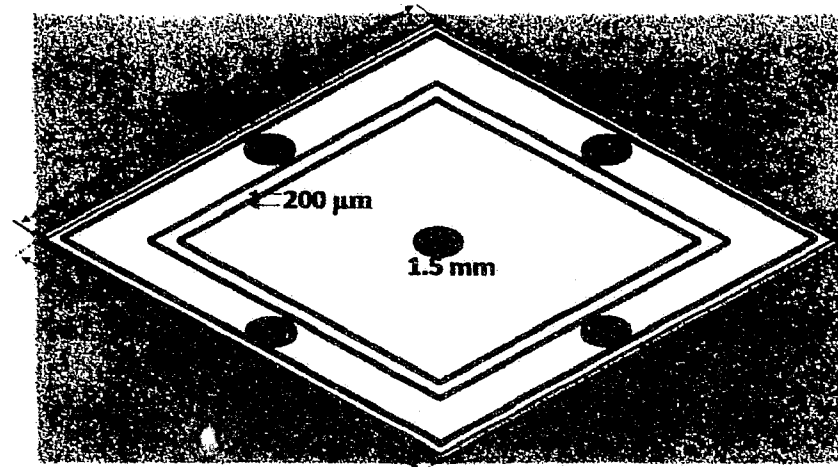
Figure 4.5: Diagram of fabricated glass steamdome.

Each fabricated part was anodically bonded together to form the completed microboiler (see Figure 4.6). The bonding setup consisted of a hotplate and a pair of aluminum plates connected to a voltage supply. The individual parts were cleaned utilizing RCA-I and RCA-II techniques prior to the bonding process [58, 59]. This removed any organic and inorganic contaminations attached to the bonding surface. The boilerplate and the glass steamdome were held in place using a pair of aluminum supports. The entire apparatus was then placed atop the hot plate. The hot plate was preheated to 400 °C and a voltage of 400V was supplied with the positive terminal connected to the silicon side [59]. The apparatus was visually inspected at 5 minute intervals to assess bonding progress. Relying on this verification, the voltage remained at 400 V or was increased up to 700 V to enhance bonding quality. After approximately 15-30 minutes, the anodically bonded boiler was obtained. Enclosed volumes for the

working fluid and the steam collecting chamber were formed by bonding the boilerplate

with the steamdome (see Figure 4.6). The boiler was now ready for the test setup

and characterization.
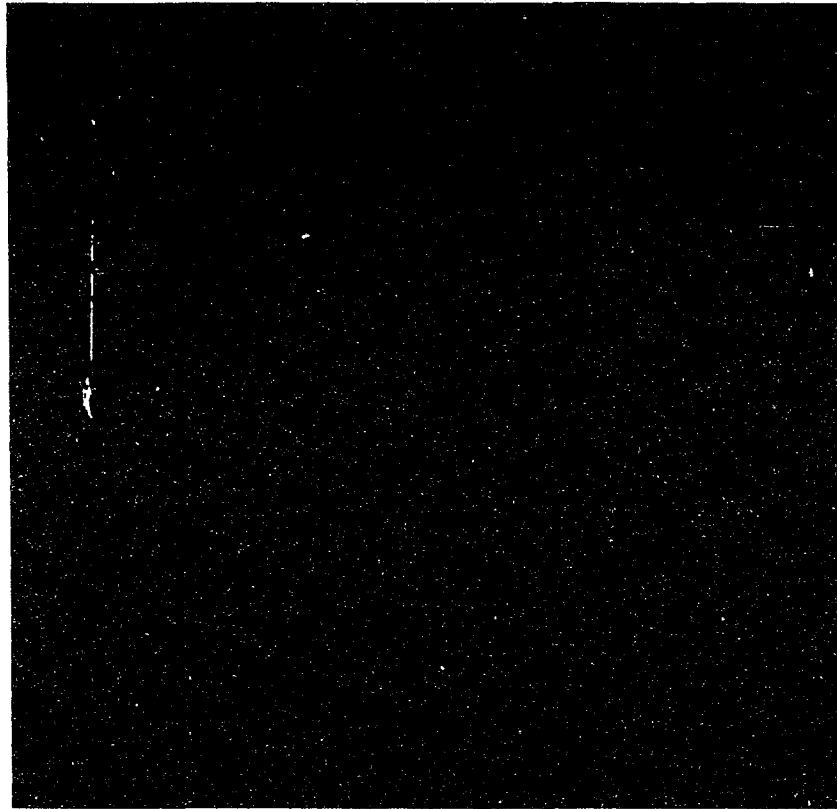
Figure 4.6: Top-down view of the anodically microboiler with steamdome and base.

4.5.2 Test Setup

A number of different components were added to the completed boiler to allow

for testing and characterization. These included fluid inlet and outlets, thermocouples

(TC), pressure transducers, and heat flux sensors (HFS). For outlet from the boiler,

a brass nipple fitting (supplied by McMaster-Carr) was attached to the central exit

hole atop the steam collecting chamber. 'T' shaped tubing was fitted to the brass

nipple and then properly sealed using epoxy to avoid any leakage of vapor exiting the

steamdome during operation. A pressure sensor type P600 (supplied by KAVLICO) was attached to the opening in line with the exit to monitor the microboiler operating pressure. Micro tubing (supplied by IDEX Health and Science LLC) approximately 8 mm long was fitted and sealed to the other opening end of the T-tube. This served as an outlet to the microboiler.

For the fluid inlet to the microboiler, micro tubing with a pressure sensor combined in-line was inserted into the inlet hole atop the reservoirs and epoxied in place to avoid fluid leakage during testing. The sensor monitored any back pressure exerted by the microboiler to the inlet flow. A resistance heater type KHLV-101/P (Omega Engineering, Inc.) was used for the heat addition to the microboiler system. The heater was connected to a DC power supply (BK Precision). The supply was capable of reading both voltage and current in a heater connected circuit. This allowed determination of power supplied to the microboiler during testing. K-type thermocouples (Omega Engineering, Inc.) were incorporated in the microboiler to monitor the temperature of the steam collecting chamber, the central part of the channels, the surrounding reservoirs and the outer surface of the steamdome. Additional thermocouples (TCs) were attached at the bottom of the microboiler to measure input or heater temperature. All attached sensors were connected to a data acquisition system (supplied by National Instruments) and then linked to a computer via LabVIEW SignalExpress software to automate recording. Figure 4.7 shows the microboiler with additional components included. Input powers of 1.8 W and 2.7 W were supplied to the heater for each series of tests. These powers were selected by comparing the resulting temperature of the heater with the waste heat temperature

available from a typical 4 cylinder Otto cycle engine, a potential source for waste heat collection. Temperatures can range from approximately 600 °C (exhaust) to 130 °C (radiator) [60]. The temperatures reflected by the heater for the given power inputs were in this range and therefore well suited for these investigations.

Figure 4.7: Microboiler test setup placed atop the balsa wood.

Three independent experiments were performed on the microboiler to understand the working capability of the boiler. The experiments were designated as: Dry, Atmospheric and Pressurized. Independent of test type, the boiler was first allowed to heat to steady state prior to data collection. This was verified by monitoring of the operating temperature profiles of the boiler during warm-up. Figure 4.8 shows a typical temperature recording for a Dry Test. Steady state was achieved after approximately 12.5 minutes. A detailed explanation of all test setups and techniques are presented in the following sections. In addition, a detailed finite-difference model was generated to predict mass flow rate expectations of the boiler in operation.
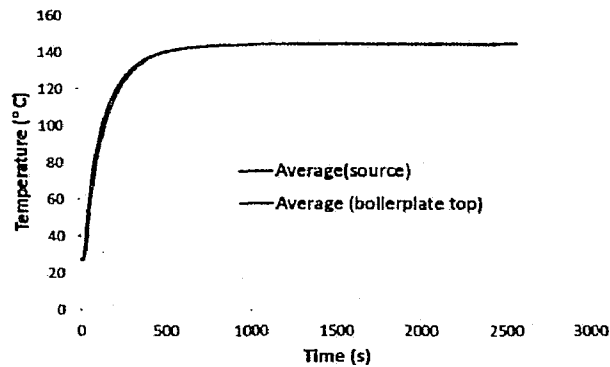
Figure 4.8: Typical operating temperatures in Dry Tests showing steady state.

4.5.2.1 Dry Test

The Dry Test was performed without supplying fluid to the boiler for each power input. The heat supply component consisted of a heat flux sensor (HFS) sandwiched between the two heaters. The heat supply component was then attached to the boiler (see Figure 4.9). Equal powers were supplied to the heaters and the HFS output was recorded. The HFS demonstrated a zero heat flux output. This indicated that there existed no temperature gradient between the top heater bottom surface and the bottom heater top surface allowing heat to flow in upward direction towards the boiler.
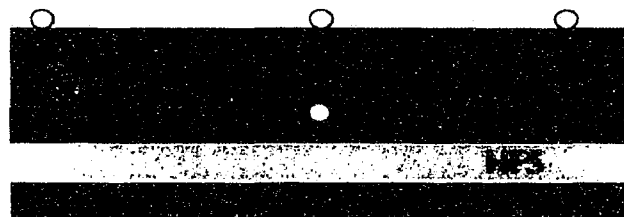
O Thermocouple

Figure 4.9: TCs attached at different loc tions of the microboiler setup.

The experiment was conducted until a steady state temperature profile was achieved. The temperature data from the TCs were recorded. Temperature data allowed evaluation of temperatures at various locations of the microboiler for both levels of power input. Temperature readings were utilized for subsequent model validation work (refer to Section 2.2.1) which was utilized to predict the available heat flux across the capillary channels for the phase change of fluid in the Wet Tests (Atmospheric and Pressurized). Following completion of boiler operation without working fluid, the data was utilized in the modeling effort described in Section 3.2.2.

4.5.2.2 Thermal Modeling

A computational model using the Finite Difference Method (FDM) was generated to replicate the Dry Test. The model allowed detailed evaluation of temperatures across the boiler plate and further utilized those temperatures to predict the energy available for phase change of the working fluid. This was utilized to establish expected working fluid consumption capability for the Wet Tests.

A transient heat conduction model was employed assuming uniform temperature distribution across the capillary channels. This was due to the symmetry structure of the radial channels as shown in Figure 4.10. A single radial channel was considered and the temperature profile was assumed constant irrespective of change in the theta direction. This reduced the 3-D problem to a 2-D problem along the $r = x$ and z (thickness) directions. The model utilized FDM to discritize the heat exchanger into nodal points. The explicit transient heat conduction equation was solved at each

nodal point to evaluate the temperature using Equation 4.1:

$$\nabla^2 T = \frac{\rho C_p}{k}\left(\frac{\partial T}{\partial t}\right).$$ (4.1)
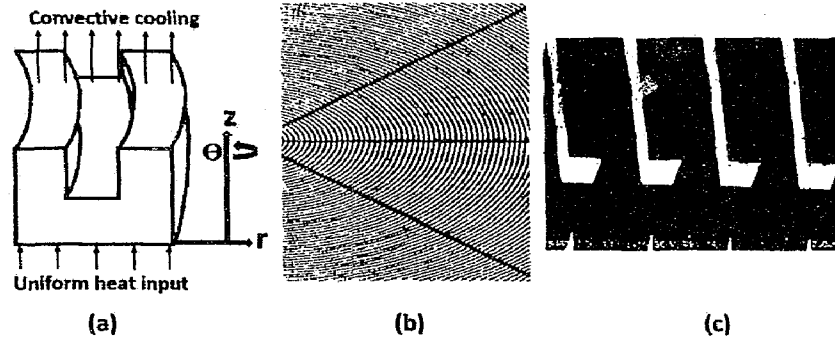
Figure 4.10: An image showcasing the axis (a), the uniformly heated symmetrical radial channels (b), and the enlarged view of the channels (c).

In Equation 4.1, T, t, ρ, C_p, and k are the temperature, time, density, specific heat capacity and conductivity, respectively. The material property of silicon and the dimensions of the wall and the channel were considered. The convection condition at appropriate nodes was also included in the model. The convection coefficient of approximately 18 $\frac{W}{m^2 K}$ was considered in the model. This was determined by introducing known values of supplied heat flux (q), the resulting temperature via conduction (T), and the ambient temperature ($T_{infinity}$) as recorded in the initial Dry Test operation. Equation 4.2 shows the subsequent calculation of h, the convection coefficient. Moreover, the calculated value of h was also well in line with the natural convection range of approximately 5 to 20 $\frac{W}{m^2 K}$ [61].

$$h = \frac{q}{(T - T_{infinity})}.$$ (4.2)

Figure 4.11 shows the 2-D geometry utilized for the model. Appropriate initial and boundary conditions were applied to replicate the real-world Dry Test. The

temperature profile across the model was obtained by converging iteration based on energy difference $(E_{in} - E_{out})$. It was maintained as low as micro-Watts for each power input. The nodal temperature generated via modeling was compared with the Dry Test temperature result to validate the model. After this validation, the amount of thermal energy available from the channels to deliver to the fluid was evaluated. The heat flux generated by the model was utilized to calculate the mass feed rate into the boiler. It is essential to determine the fluid feed rate prior to the Wet Tests (Atmospheric and Pressurized). The mathematical calculation for the maximum mass feed rate ($\dot{m}$) is given by Equation 4.3. In Equation 4.3, the available heat flux ($P_{available}$) is divided by the working fluid heat of vaporization to yield the mass feed rate. ($P_{available}$) was provided by the model and the heat of vaporization (ΔH_v) was acquired from known properties of the working fluid used in all Wet Tests.

$$\dot{m} = \frac{P_{available}}{\Delta H_v}.$$

(4.3)
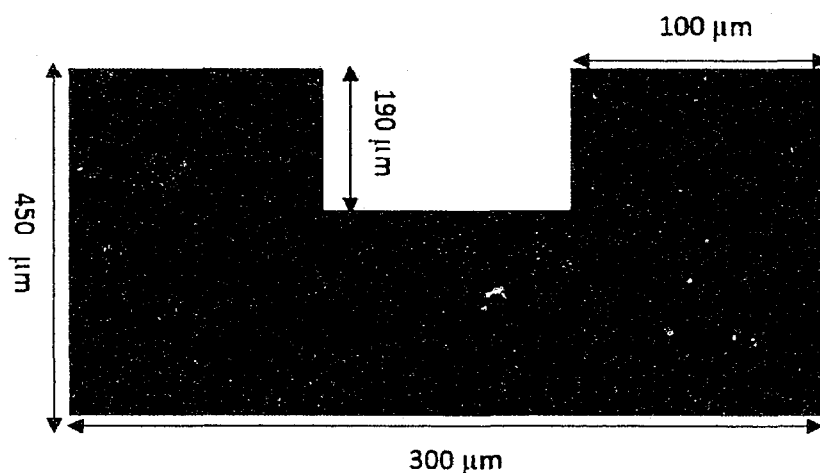
Figure 4.11: A 2-D profile of the 3-D symmetry capillary channel.

In this work, $3MNOVEC^{TM}HFE - 7200$ was selected as the working fluid. This was dependent on several things including the temperature at the boilerplate and other fluid properties like fluid-surface contact angle that enhanced capillary action, high heat of vaporization, and low environmental impact. This fluid has a favorable low boiling temperature of 76 °C which was appropriate for the study. It also demonstrated high wettability with the surface. In addition, it presented high heat of vaporization (ΔH_v) of about 125 $\frac{kJ}{kg}$ and low environmental impact [36]. Due to these favorable fluid properties, refrigerants has been utilized for boiling heat transfer in several studies [62]. Considering HFE-7200 as the working fluid, the mass flow rate was determined. This readied boiler for the Wet Tests.

4.5.2.3 Atmospheric Test

In the Atmospheric test, the boiler was operated at atmospheric pressure with working fluid supplied. The working fluid mass exiting the microboiler due to the phase change of the supplied working fluid was studied for each individual power input. The atmospheric test provided insight into the potential of the capillary channels to pump fluid at ambient condition and allowed the determination of a boiler efficiency parameter (energy absorbed via phase change of the fluid (P_{eva})) as defined by Equation 4.4.

$$Efficinecy(\%) = \frac{P_{eva}}{P_{available}} \times 100\%. \tag{4.4}$$

Figure 4.12 shows the test setup with a clamp included that was used to obstruct the exit of the boiler. The clamp was important to subsequent pressurized testing but was not utilized in these atmospheric tests. In these tests, boiler operating

pressure was maintained at atmospheric conditions; hence, the outlet was left open. A constant heat was supplied from the heater attached to the bottom of the boiler. The temperature and the pressure data were monitored. The boiler was heated for about 12.5 minutes to attain steady state (see Figure 4.8). After steady state was achieved, the predicted flow rate in Section 2.1.2 via modeling was supplied.
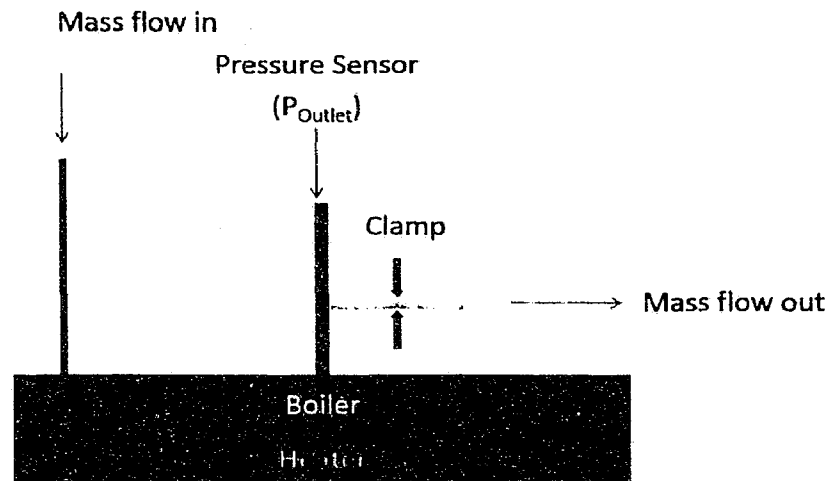
Figure 4.12: Atmospheric and Pressurized Test setup.

The working fluid was supplied to the boiler via inlet tubing connected to a syringe/infusion pump. The infusion pump was utilized in order to monitor accurately the mass flow rates supplied to the boiler. Phase change occurred on the heated boiler plate as working fluid entered and heated within the capillary channels. Working fluid exiting the boiler was collected in a 10 cc plastic syringe and cooled using ice cubes surrounding the syringe for the fixed period of about 4 minutes. Cooling the working fluid in ice cubes ensured full condensation of the collected boiler outflow. The mass of the collected fluid was measured via precision scale. The measured mass was then

divided by duration of the test and the energy absorbed due to phase transformation of the fluid. In this way, the efficiency of the boiler for each power input was determined.

4.5.2.4 Pressurized Test

Following the Atmospheric test, the pressurized test was performed on the boiler. In this test, the boiler was operated at elevated pressure. This allowed investigation of capillary channel ability to pump fluid effectively at different operating pressures.

The test setup was similar to the setup presented in Figure 4.12, however, this time making use of the clamp. The clamp provided obstruction to the boiler's exit, allowing operation under a pressurized environment. Pressurized testing commenced in similar fashion to atmospheric testing. First, the boiler was heated to steady state at the given power input (1.8 W or 2.7 W). The temperature and pressure data were recorded. Working fluid was introduced based on the modeling effort described in Section 2.2.2 with initial supply matching atmospheric test conditions. The boiler was then pressurized via clamp application and the flow rate supplied to the boiler was reduced to match the reduced mass flow leaving the boiler. This prevented an over-supply condition to the boiler's operation.

This technique was verified by visualizing the temperature and the pressure profile of the boiler over the duration of operation. In these pressurized tests, the test duration was 2 minutes. For each degree of restriction and its adjusted flow rate, the temperature and the pressure data were recorded. These tests provided the insight into saturation temperature and corresponding pressure for the specific flow

rate. However, to verify the operating condition of the boiler during elevated pressure testing, additional components and analysis were employed.

4.5.2.5 Superheater Test

Superheater components and tests were employed to validate fully and characterize the boiler's operation. The use of the Superheater was used in these tests to validate the boiler's operation and working fluid thermodynamic state. The Superheater successfully elevated the temperature of the working fluid beyond saturation conditions to full superheat as validated by $3M^{TM}$ thermodynamic tables. By monitoring the pressure and temperature of the working fluid leaving the boiler and traversing the Superheater, additional test points allowed characterization of boiler operation through the saturation conditions of the working fluid and along lines of constant pressure superheat. In real-world applications, a Superheater may be employed to increase energy available to connected power output devices.

Using the basic boiler test setup (Section 2.2), additional components to superheat the working fluid were added that included pressure sensor, TCs, and two resistance heaters. First, the boiler's exit was connected directly to the in-house built Superheater. Figure 4.13 shows the additional components employed along with the arrows pointing data collecting locations.
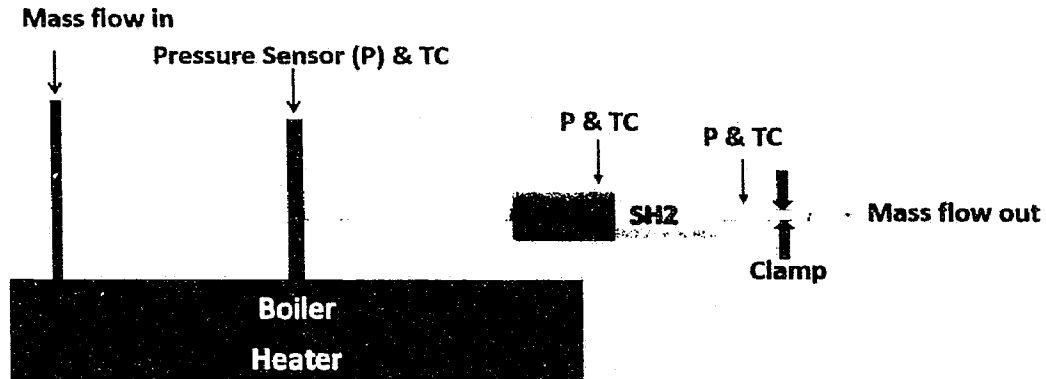
Figure 4.13: Superheater Test setup with all included components.

In fabricating the Superheater, two micro-sized copper tubes of equal length were utilized. Each tube was carefully bent in serpentine manner to allow maximum exposure to additional resistance heaters that were attached around the bends (see Figure 4.14(a)). This presented two distinct sections of the Superheater where temperature and pressure data could be monitored between sections. The heaters were then connected to separate voltage supplies with the capability of voltage and current read outs. T-tubing connected the two sections of serpentine Superheater tubes and allowed an inline pressure sensor and TC to monitor working fluid conditions. A second T-tubing was connected to the outlet of the second Superheater with a second pressure sensor and TC. Finally, the boiler's output was attached directly to one end of the combined Superheater sections. Figure 4.14(b) shows the device with heaters and tubing enclosed below insulation marked SH1 (Superheat 1) and SH2 (Superheat 2). All the connections were checked and then sealed properly to avoid any leakage of vapor during testing.
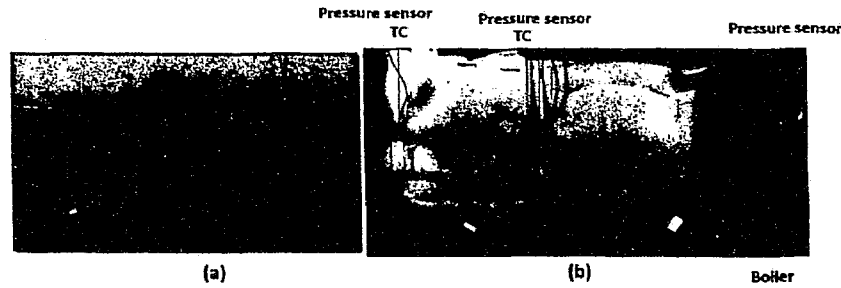
Figure 4.14: Copper tube bent in serpentine manner (a) and boiler test setup with connected Superheater (b).

Operation of the boiler and Superheater commenced with the full setup heating to steady state. All temperature and the pressure data was recorded. Table 4.1 shows the full list of pressure recordings (by location) and temperature readings (by location). As before, the working fluid flow rates were utilized based on atmospheric testing of the boiler, then reduced as operating pressure increased for each test. Several tests were conducted to investigate operating pressure versus saturated temperature and superheated temperature correlations. In this approach, first the vapor temperature was maintained constant throughout the entire setup (boiler and Superheater). This allowed the operation at the saturated region of the fluid. To operate at the superheated region, the power to the Superheater was increased in steps to further raise the temperature of the incoming vapor from the boiler. For each test, resulting vapor temperature and pressure were noted. The test was then repeated for a different flow rate and operating pressure. The noted pressure data was then utilized to verify the boiler's operation along the isobars of the working fluid.

Table 4.1: List of pressure (P) recording and temperature (T) recording by locations.

Boiler (P,T)	SH1 (P,T)	SH2 (P,T)
Vapor temperature and pressure monitored inside the steam collecting dome or at the boiler exit	Temperature and pressure recorded at the outlet of SH1 or between the Superheaters (SH1 and SH2)	Temperature and pressure of the steam recorded at the exit of the setup

4.5.3 Experimental Error

Kline and McClintock uncertainty analysis was utilized to evaluate the error associated with the test data [38]. The error associated with the voltage and the current readings were $\pm$ 0.1 V and $\pm$ 0.001 amp, respectively. The error associated with each power input was $\pm$ 9 mV. Error associated with temperature, mass of the fluid and time were on the order of $\pm$ 0.5 °C, $\pm$ 0.005 g and $\pm$ 1 second, respectively. The error associated with each individual evaporation rate was determined to be in the order of $\pm$ 0.56 $\frac{mg}{s}$. The error associated with the pressure reading was $\pm$ 0.5 kPa.

4.6 Result and Discussions

The microboiler consisted of a boilerplate base and a steamdome covering top. These parts were fabricated separately and then anodically bonded to form the boiler. The fabricated boiler was then equipped with additional components to ready it fully for testing. The tests were categorized as the Dry Test and the Wet Test (Atmospheric and Pressurized). In the Dry Test, the operational characteristics were tested without supplying any working fluid to the boiler. These included selection of the power inputs and monitoring of the temperatures for the supplied power inputs at different locations of the boilerplate. Using these temperatures, the computational model was validated. The validated model was then utilized to discern heat available at the channel for

the evaporation of the working fluid. This generated heat flux was further utilized to evaluate the working fluid mass flow rate. These combined results established the working baseline for the Wet Test.

In the Wet Test, two sets of tests were performed on the microboiler utilizing the established baseline from the Dry Test. First was the atmospheric test in which the boiler was operated in the atmospheric pressure. In this test, the boiler's ability to pump fluid out of the boiler via phase change was evaluated. This provided one measure of boiler efficiency. Second, the boiler was operated in a pressurized condition to investigate the working capability of the capillary channels to draw fluid under the pressurized environment. This test was then extended by including Superheaters at the outlet of the boiler. Results from this test were utilized to validate the boiler's operation along the isobaric pressure line of the working fluid. Reporting of these test results is presented in the following sections.

4.6.1 Dry Test

A resistance heater and the K-type thermocouples (TC) were utilized to supply heat at the bottom of the boilerplate and to measure temperatures at different locations of the microboiler, respectively. The power supplied to the heater was selected to replicate real-world available heat sources as noted in Section 2.2. Power inputs of 1.8 W and 2.7 W were selected which yielded the heater temperatures of about 106 °C and 144 °C, respectively.

Power was supplied and the temperatures were recorded at locations indicated in Figure 4.9. After steady state was achieved, the test was run for approximately

15 minutes and the temperature readings were averaged (see Figure 4.8). Table 4.2 shows the recorded temperatures. The average temperature at the boilerplate top were 105.5 °C and 143 °C for the power inputs of 1.8 W and 2.7 W, respectively.

Table 4.2: Temperature reading of the boilerplate.

P_{in} (W)	Reservior (°C)	Center of Channel (°C)
1.8	105	106
2.7	142	144

4.6.2 Thermal Modelling

The Dry experimental test provided the power inputs (P_{in}) and corresponding temperatures of the heater and the temperature at the top of the boilerplate. This data was utilized in the model as described in Section 2.2.2. The designed model replicated real test conditions to provide accurately the heat flux available at the channel for the phase conversion of the fluid. The temperature distributions of the simulated model with 1.8 W power input is presented in Figure 4.15.
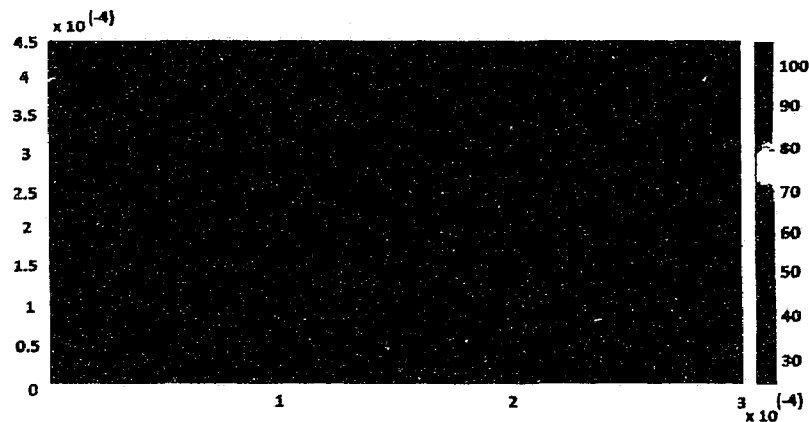
Figure 4.15: Temperature distribution with 1.8 W power supply.

In order to verify the simulation, results obtained were compared to the Dry Test temperatures. The comparison of the results are summarized in Table 4.3. The maximum discrepancy in the test and simulation model result was less than ± 5%. This validated the accuracy of the model.

Table 4.3: Comparison of the Dry Test and the model.

Input Power (P_{in}) (W)		Average Temperature (°C)		Available Heat flux (W)
Experiment	Model	Experiment	Model	
1.8	1.8	105.5	105.9	1.14
2.7	2.7	143	143.9	1.72

The heat fluxes indicated by the model as available for phase change of the fluid were 1.14 W and 1.72 W for 1.8 W and 2.7 W, respectively. These determined heat fluxes were then utilized to establish expected working fluid mass flow feed rates into the boiler for the Wet Test (Section 2.2.2). The mass flow rate for each power input is presented in Table 4.4. The mass flow rates were 9 $\frac{mg}{s}$ and 13.6 $\frac{mg}{s}$ for the power inputs of 1.8 W and 2.7 W, respectively.

Table 4.4: Determination of the mass flow rate.

P_{in} (W)	$P_{available}$ (W)	ΔH_v ($\frac{kJ}{kg}$)	$\dot{m}$ ($\frac{mg}{s}$)
1.8	1.14	125	9.12
2.7	1.72	125	13.6

4.6.3 Atmospheric Test

Following approximation of the mass flow rates, the boiler was ready for tests involving fluid with power input and fluid supply rates as shown in Table 4.4. The

typical temperature profile of the boiler before and after the fluid supply is illustrated

in Figure 4.16 for power input of 1.8 W.
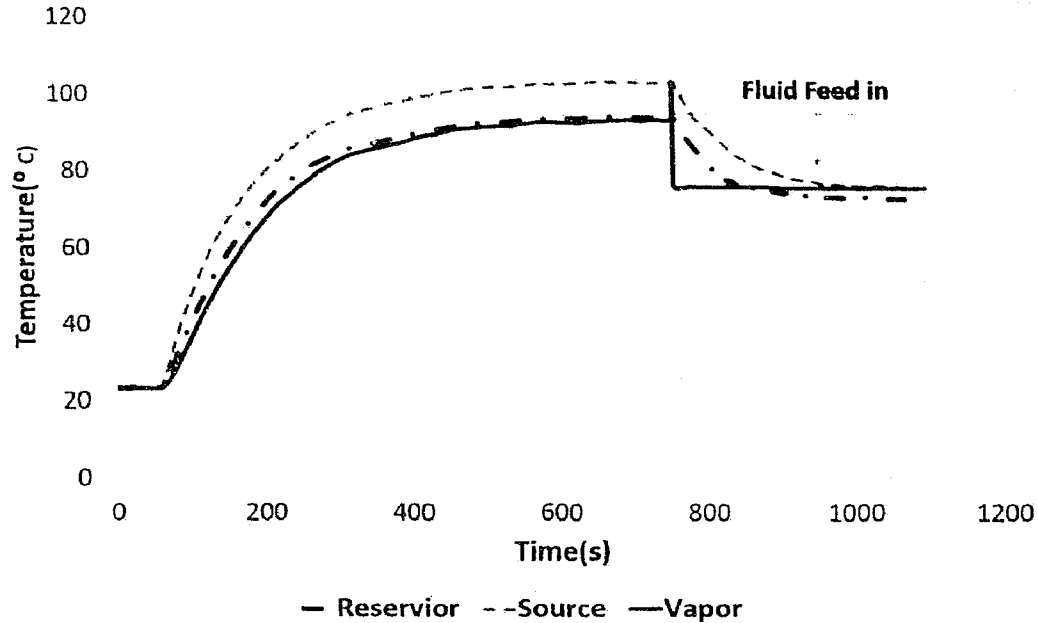
Figure 4.16: Temperature profile of the heat source, the reservoir, and the steam.

Vaporized fluid exiting out of the boiler was collected and weighed as described

in Section 2.2.3. A set of three tests was performed for each power input. Results

were averaged and are presented in Table 4.5.

Table 4.5: Measured temperature and the mass flow rate for each power input.

P_{in} (W)	$P_{available}$ (W)	Source Temperature (°C)	Steamdome Temperature (° C)	Vapor (°C)	Mass Feed Rate ($\frac{mg}{s}$)	Average Mass Exit Rate ($\frac{mg}{s}$)
1.8	1.14	106	75.1	75.6	9	8
		106	75.1	75.6	9	
		106	75.1	75.6	9	
2.7	1.72	144	75.1	75.6	13.6	11.9
		144	75.1	75.6	13.6	
		144	75.1	75.6	13.6	

The calculated averaged mass flow rate in Table 4.3 was combined with the heat of vaporization of HFE-7200 to determine energy absorbed via phase change of the working fluid and the efficiency of the microboiler. Figure 4.17 illustrates the comparison of the power input and the power observed via phase transformation of the fluid supplied. The boiler's efficiency is summarized in Table 4.6.
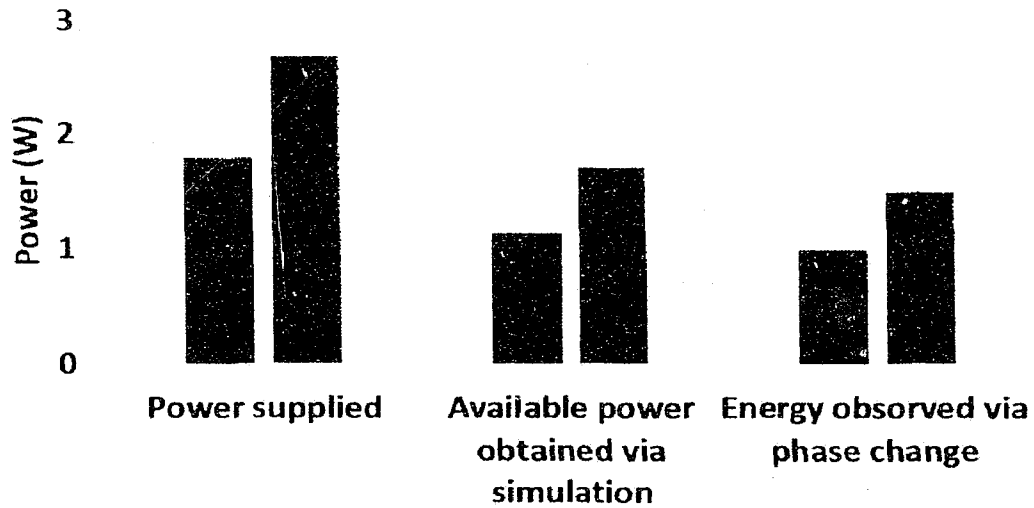
Figure 4.17: Supplied power vs power observed via phase change.

Table 4.6: Efficiency of the boiler.

$P_{available}$ (W)	ΔH_v ($\frac{kJ}{kg}$)	$P_{evaporation}$ ($\frac{mg}{s}$)	Efficiency (η) (%)
1.14	125	1	87.8
1.72	125	1.48	86.2

The boiler demonstrated the phase conversion rates of 8 $\frac{mg}{s}$ and 11.9 $\frac{mg}{s}$ for the fluid inputs of 9 $\frac{mg}{s}$ and 13.6 $\frac{mg}{s}$, respectively. These values showed improvement versus boilers presented in prior efforts where a larger dimension acrylic steamdome was utilized [35, 56]. The use of a thin glass wafer as a steamdome eliminated a significant heat sink effect as previously encountered. It should be noted that the

temperature of the steamdome and vapor are almost equal. This allowed vapor to exit the boiler without premature condensation, thus improving the boiler's operation.

Despite improved operation, some loss of working fluid mass was encountered. The boiler presented a maximum mass loss of about 12%. This loss was likely the result of the volatile nature of the HFE-7200 fluid combined with the capture and mass measure technique. To verify this assertion, an additional test was performed that replaced HFE-7200 fluid with water. This eliminated the volatile behavior of the HFE-7200 and verified the accuracy of the mass measurement.

With HFE 7200 as the working fluid, the boiler was heated to steady state and water was supplied. The phase changed vapor was collected and condensed. The comparison of the measured mass flow rate out of the boiler at 1.8 W power input using water and HFE-7200 as the working fluid is summarized in Table 4.7. For comparison, results obtained using water demonstrated significantly reduced loss. Approximately 98% of the water supplied was collected following exit from the boiler. This is not an unexpected result as indicated by formal HFE properties supplied by $3M^{TM}$. The typical evaporative losses for the HFE-7200 is approximately in the range of 339 $\frac{mg}{(s-m^2)}$ to 1017 $\frac{mg}{(s-m^2)}$ when exposed to ambient temperature and pressure [63].

Table 4.7: Comparison of the mass flow rate for the different fluids.

Workig Fluid Type	P_{in} (W)	Mass Feed Rate $(\frac{mg}{s})$	Mass Exit Rate $(\frac{mg}{s})$
Water	1.8	6 6 6	5.9
HFE-7200	1.8	9 9 9	8

4.6.4 Pressurized Test

The mass flow rate and power input were supplied to the boiler as shown in Table 4.4. The boiler was allowed to operate at atmospheric pressure and then the outlet tubing was restricted. The flow rate supplied to the microboiler was then adjusted to match the mass flowing in and leaving the boiler as explained in Section 2.2.4. Figure 4.18 shows the temperature and pressure profile for each adjusted flow rate to the boiler with 1.8 W input.
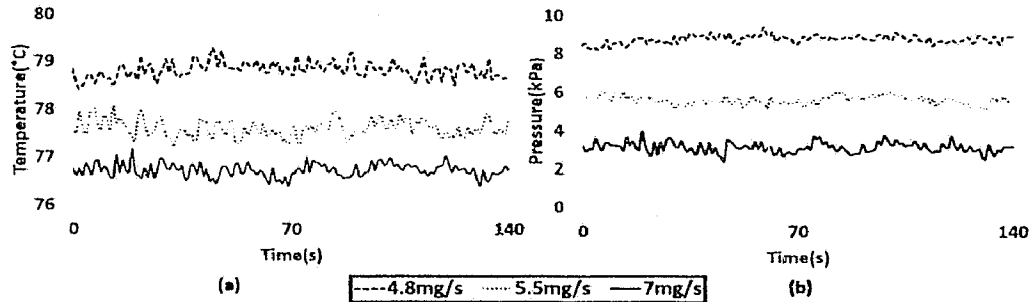
Figure 4.18: Temperature (a) and pressure (b) trends by varying restriction to the boiler exit for 1.8 W power input.

Similarly, Figure 4.19 shows the temperature and the pressure profile for each adjusted flow rate to the boiler for the 2.7 W power input.
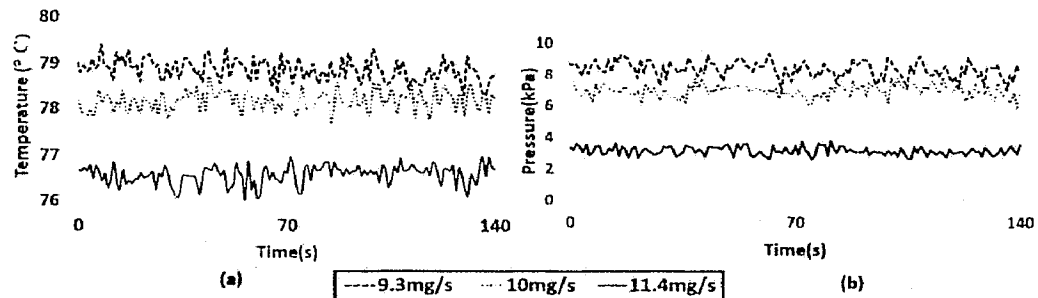
Figure 4.19: Temperature (a) and pressure (b) trends by varying restriction to the boiler exit for 2.7 W power input.

The data in Figure 4.18 and Figure 4.19 were averaged and the standard deviation associated with each temperature and pressure calculation are summarized in Table 4.8 for all power inputs.

Table 4.8: The average temperature and pressure for each flow rate along with supplied power.

P_{in} (W)	Mass feed rate ($\frac{mg}{s}$)	Vapor Temperature (°C)	Pressure (kPa)	3M®Pressure (kPa)
	9	75.6	0g	0g
	7	76.7 ± 0.14	3 ± 0.3	2.3
1.8	5.5	77.6 ± 0.2	5.6 ± 0.2	5.3
	4.8	78.8 ± 0.2	8.8 ± 0.2	9.4
	13.6	75.6	0g	0g
	11.4	76.6 ± 0.3	3 ± 0.4	2.0
2.7	10	78 ± 0.3	6.9 ± 0.4	6.6
	9.3	78.9 ± 0.35	8.5 ± 0.2	9.7

Based on Table 4.8, pressure versus temperature data were plotted as a function of the mass flow rate for each power input (see Figure 4.20). The boiler operating temperature and pressure were increased as restriction on the boiler's exit was increased. In good agreement with a saturated working condition, pressure and temperature data demonstrated that vapor temperature followed the increasing trend of the operating pressure inside the steamdome. This was true for all power inputs as well as when these power inputs were compared to each other for particular pressure point. For the operating pressure of 3 kPa, the saturated temperature of the steam was approximately 76.7 °C for both power inputs. Such phenomenon were visualized for other operating pressures as well (see Figure 4.20). This validates that for the specific saturated pressure there exists a unique saturated temperature and the boiler operation as saturated. Moreover, the pressurized test provided the saturated temperature and pressure points of the HFE-7200 working fluid.
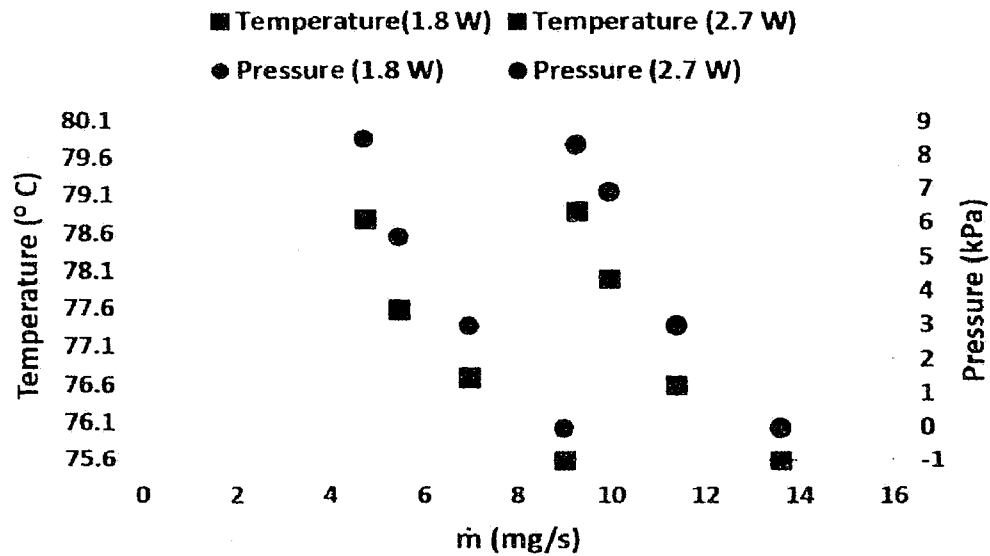
Figure 4.20: The plot of the boiler's operating pressure versus vapor temperature for all power inputs.

To obtain the superheated properties of the HFE-7200 working fluid, the temperature of the steam exiting the boiler was further raised. The results from the test are presented in the following section.

4.6.5 Superheater

Following the Pressurized tests, specific superheating tests were performed. This was achieved via inclusion of the Superheater as shown in Figure 4.14 on the output flow from the steamdome. Power of 1.8 W was supplied to the boiler and the flow rate and operating pressure were based on Table 4.8. The flow rates of 7 $\frac{mg}{s}$ and 5.5 $\frac{mg}{s}$ with the operating pressure of 3 kPa and 5.6 kPa were selected. The temperature and pressure data were recorded at different locations of the setup (refer Table 4.1). Table 4.9 summarizes these recordings at the boiler and at the Superheater.

Table 4.9: The temperature and the pressure recording of the vapor by location.

P_{in} (W)	Feed Rate ($\frac{mg}{s}$)	Vapor Temperature (°C)			Operating Pressure (kPa) (kPa)		
		Boiler Outlet	SH1 Outlet	SH2 Outlet	Boiler Outlet	SH1 Outlet	SH2 Outlet
1.8	7	76.8	76	76.5	3	3	3
		76.6	95	96.7	3	3	3
		76.7	105	107	3	3	3
1.8	5.5	77.5	76.5	77	5.6	5.6	5.6
		77.4	85	86.9	5.6	5.6	5.6
		77.4	101	103	5.6	5.6	5.6

The recorded data were then related to $3M^{TM}$ provided HFE-7200 thermody-namic tables to interpolate entropy at specific temperature-pressure points. Figure 4.21 shows the plot of temperature versus entropy. The plot establishes the boiler operation along the isobaric line of the working fluid.
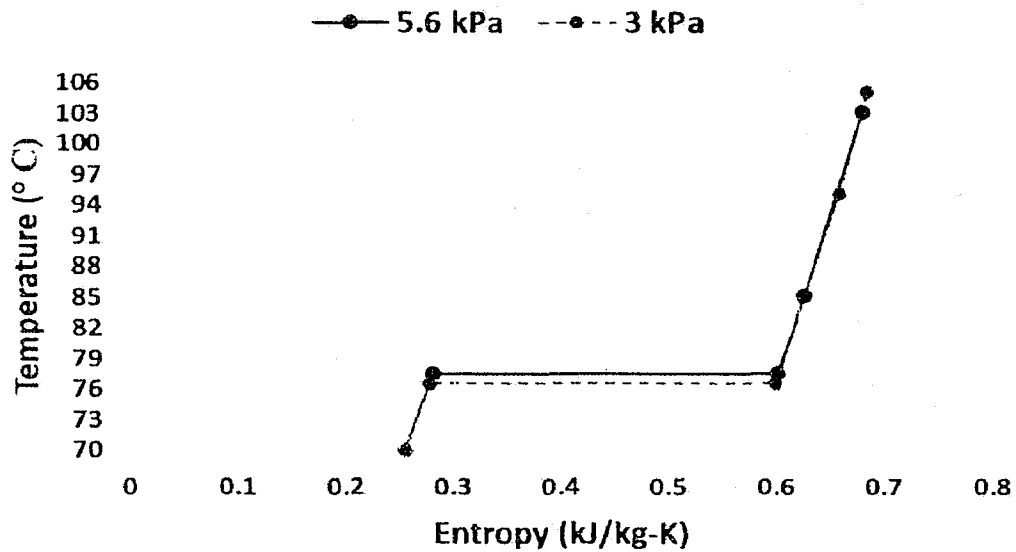
Figure 4.21: Temperature vs entropy plot of the boiler operation.

With these insights into the boiler's characterization, further boiler development has been planned. The future work includes miniaturization of the Superheater to incorporate it beneath the primary boiler plate. Such modification will allow the

evaporated fluid exiting the steam dome to traverse the Superheater utilizing a single heat source located beneath the boiler. This will better simulate a situation where a single heat source (like an Otto cycle) supplies heat to the entire system.

4.7 Conclusion

The efficiency of a thermodynamically limited process could be improved by recovering the heat lost to the environment. One such approach is via installation of a waste heat recovery system. The system recovers the heat and converts it to useful work. Already established micro devices and engines provide such opportunity at low capital cost. In this work, a MEMS based boiler has been constructed and tested for such an application.

Several tests were performed to investigate the boiler's operation. The Dry Test provided the selection of power inputs and temperatures. The selected power inputs were 1.8 W and 2.7 W and the temperatures via conduction were 106 °C and 144 °C, respectively. These temperatures were utilized to verify the finite difference method (FDM) model of the boiler. The validated model predicted the available power via conduction. The power was utilized to calculate fluid feed rate for the Wet Tests. A working fluid was selected based on the realized operating temperatures of the dry boiler. In this work, 3MTM HFE-7200 was utilized. The evaluated mass flow rates were approximately 9 mg/s and 13.6 mg/s for the 1.8 W and 2.7 W, respectively. These flow rates served as the baseline fluid feeds to the boiler in Wet Tests.

In Wet Tests, the ability of the capillary channels to pump fluid under atmospheric and pressurized environments was studied. In addition, a superheated

test was performed by raising the steam temperature exiting the boiler. Based on available working fluid data for HFE-7200, a T-s chart was plotted that graphically established key isobaric operation and thermodynamic conditions of the boiler.

Operation of the boiler across these test points clearly showed the boiler as a potential future waste heat scavenging device. Radial capillary channels presented enhanced mass flow rate for phase transformation via capillary flow. In addition, a 500 μm m glass steamdome inclusion in the design reduced the boiler mass and the heat sink effect significantly versus prior boiler iterations. Such modification minimized the pre-condensation of vapor inside the steamdome. A maximum efficiency of approximately 88% was demonstrated by the boiler, an improvement of about 50% compared to previously published work [35]. Furthermore, the operating pressure of the boiler elevated as well. A peak operating pressure of 8.5 kPa was demonstrated by the boiler.

CHAPTER 5

SUPERHEATER DESIGN FOR A MEMS BASED LOW TEMPERATURE HEAT SCAVENGING SYSTEM

5.1 Overview

This chapter presents the subsequent redesign of the Superheater discussed in Section 4.4.2.4 to form an integrated boiler/Superheater single system. A computational modeling approach was considered to study the effects of design parameters on heat and mass transfer, temperature and pressure drop across the Superheater prior to fabrication and characterization. The results of the Superheater Test (refer Section 4.5.5) served as the input parameters for this study. The design parameters, model physics and results generated by the simulation to optimize the Superheater design are presented in detail.

5.2 Motivation and Background

Interest in micro-devices and engines to recover waste heat has been increasing. This is because of the inevitable heat loss from thermodynamically inefficient systems [3]. One approach to improve efficiency is to capture the discarded energy and convert it to useful work. This can be achieved via utilization of a low cost microscale heat scavenging device. Such notion to recover waste heat has been well established. Some of the notable researched dynamic heat recovery engines are gas turbines [41, 42], other

rotary engines [28, 30], free piston engines [43, 44], and membrane type actuators [45]. These devices are designed to capture waste heat and generate mechanical or electrical power output to enhance the efficiency of the thermodynamically limited system.

Similar to the aforementioned engines, a MEMS-based system capable of capturing ambient waste heat and generating power is the focus of this study. The system at its completion consists of three miniature components: 1) boiler, 2) Superheater, and 3) free piston expander (FPE). The Superheater is the primary emphasis of this chapter. However, the work on the other two components (boiler and FPE) have been previously discussed and published in the literature [35, 36, 56, 23, 34, 55, 64].

The boiler captures the waste heat causing the phase change of the working fluid from liquid to vapor (refer to Figure 2.1). The generated steam is then allowed to traverse through the Superheater component. The FPE expands the superheated steam to produce useful work in either mechanical or electrical form [34, 55, 64]. The expanded vapor is then cooled and returned to the boiler. For an integrated boiler/Superheater design, the primary objective is to utilize the same waste heat source to phase change the fluid and superheat the steam by placing the boiler atop the Superheater atop the source. Such system design will allow increased space efficiency in real-world applications. This will yield comparatively higher power for a given surface area of the waste heat source. In addition, the use of superheated steam minimizes the damage caused by water droplets to the output device.

5.3 Related Research

A computational modeling approach was considered to design a thermally efficient Superheater system. Since the steam exiting the boiler is allowed to traverse the Superheater, the model is based on the numerical models published by various researchers on single phase flow in a micro channel. Qu *et al.* experimentally and numerically studied the pressure drop and the heat transfer characteristics of single-phase flow in a micro channel heat sink [65]. The heat sink consisted of rectangular copper micro channels covered with polycarbonate plastic. Deionized water was allowed to flow through the copper channels heated by the input heat fluxes of 100 $\frac{W}{cm^2}$ and 200 $\frac{W}{cm^2}$. A 3-D conjugate heat transfer model was utilized to investigate pressure drop and temperature distribution in both the solid and fluid regions. The model generated pressure drop and temperature distribution was in good agreement with the experimental data.

Therefore, the author noted that the conventional Navier-Stokes and energy equations were able to predict the fluid flow and heat transfer characteristics of a micro heat sink. Similarly, fluid flow and heat transfer characteristics of a silicon micro heat exchanger were investigated numerically as well [66, 67]. These numerical studies were based on the experimental results published by Kwano *et al.* [68]. The effect of channel geometry on the heat transfer characteristics were also studied. Peng *et al.* demonstrated experimentally the influence of non-circular channel geometry on the convective heat transfer in both laminar and turbulent flows [69].

5.4 Research Objectives and Model Development

There were three objectives of this Superheater design study. They are listed below:

- Develop Superheater computational model with micro channel close to real-world working conditions.

- Study heat and mass transfer, pressure drop, and temperature across the various channel parameters.

- Optimize the Superheater design based on modeling outputs.

Commercially available COMSOL Multiphysics^c modeling software was utilized to model the Superheater. The conjugate heat transfer physics model was utilized to couple heat transfer in solid and fluid mediums. The Superheater model was designed utilizing the parameters obtained from the preliminary boiler/Superheater experiments [23]. The parameters were fluid flow rate, heat input and working pressure. The HFE-7200 refrigerant served as a working fluid. In addition, copper was selected as a Superheater material for construction due to its high thermal conductivity, commercial availability, and low cost. A Superheater with micro capillary channels were considered to maximize the steam-copper interface surface area. Heat and mass transfer, temperature and pressure drop across the various channel dimensions were computationally studied to optimize the subsequent Superheater design using COMSOL.

The Superheater design was 35 mm in length (L_c) and 35 mm in width (W_t) similar to the boiler's dimensions. A fixed channel width (W_c) of 100 μm and a minimum channel spacing (W_w) of 100 μm was considered. This specific minimum

width was considered due to the restriction in fabricating smaller channel and wall dimensions. Single channel with walls enclosing the channel was constructed instead of n number of channels and enclosing walls along the 35 mm Superheater width. A single channel with dimensions is illustrated in Figure 5.1.
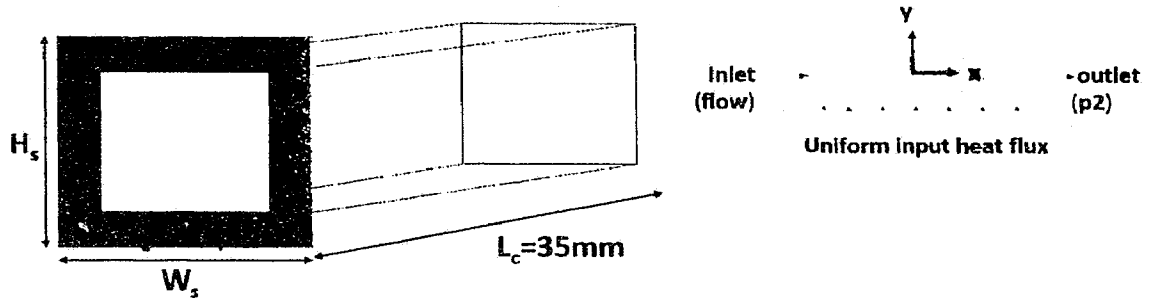
Figure 5.1: Schematic of the single channel Superheater.

The single channel model was considered due to symmetry in the channel geometry and to minimize the computational time as well. In addition, the temperature and flow distribution along each channel would be similar due to the uniform supply of heat and fluid through the Superheater. The channel heights (H_c) varied in ranges from 50 μm to 400 μm keeping a constant channel width (W_c) of 100 μm. The effect of variation in channel aspect ratios in heat and mass transfer, temperature, and pressure drop along the channels were studied (refer to Figure 5.1). Table 5.1 summarizes the channel height, width, and aspect ratio.

Table 5.1: The model channel height, width, and aspect ratio.

Height $H_c(\mu m)$	Width $W_c(\mu m)$	Aspect ratio $\frac{H_c}{W_c}$
50	100	0.5
100	100	1.0
150	100	1.5
200	100	2.0
250	100	2.5
300	100	3.0
350	100	3.5
400	100	4.0

Commercially available COMSOL Multiphysics[c] software was used for designing geometrical models, grid generation, and boundary definitions. Figure 5.2(a) and Figure 5.2(b) illustrates the 100 μm single channel model and the meshing of the Superheater. The fixed design constraint and boundary conditions were applied based on the preliminary test. Table 5.2 shows the assumptions made at the respective locations of the model. The continuity, Navier-Stokes and heat equations were solved and balanced at each discrete node to generate the required output parameters such as pressure drop, temperature, mass flow rate and change in enthalpy along the length of the channel.

$$\nabla \cdot \rho v = 0. \tag{5.1}$$

$$v \nabla v = -\frac{\nabla P}{\rho} + g + \mu \nabla^2 v. \tag{5.2}$$

$$\nabla^2 T = \frac{\rho C_p}{K} v \nabla T, \tag{5.3}$$

where ρ is density, v is velocity, P is pressure, T is temperature, μ is viscosity, K is conductivity, C_p is specific heat at constant pressure, and g is gravity.
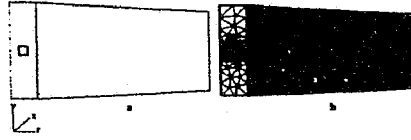
Figure 5.2: Images of the 100 μm high single channel model showcasing model (a) and mesh (b).

Table 5.2: Summary of the boundary conditions.

Boundary Condition	Location
Inlet flow velocity at channel (varying)	$X = 0$
Outlet pressure at channel (fixed)	$X = L_c$
Heat flux (uniform)	$0 < X < L_c$, $0 < Z < W_s$, $Y = 0$
Convective cooling	$X = 0$ and $X = L_c$
Adiabatic	$0 < X < L_c$, $0 < Y < H_s$, $Z = 0$ to $Z = W_s$

Equation 5.4 was utilized to calculate the flow velocity (v) for varying channel area (A). The constant input heat flux (Q_i) of 1.8 W and the mass influx rate $\dot{m}$ of 9 $\frac{mg}{s}$ was considered based on preliminary experimental result (refer to Section 4.6.5). The flow rate per channel was evaluated depending on number (n) and area (A) of the channels that can fit in the Superheater's fixed surface area of 35 mm by 35 mm using Equation 5.4. Table 5.3 summarizes the evaluated average flow velocity for different channel aspect ratios:

$$v = \frac{\dot{m}}{\rho * A * n}. \tag{5.4}$$

The evaluated flow velocity was applied as an inflow condition to the model with a respective aspect ratio. An inward heat flow of 1.8 W was applied at the bottom side of the Superheater. The adiabatic, convective and pressure conditions were applied as well to the model (refer to Table 5.2). This readied the model for computational analysis.

Table 5.3: Summary of the flow velocity versus channel height for fixed $W_c = 100$ μm.

Aspect Ratio $\frac{H_c}{W_c}$	Analytical Flow Velocity $(\frac{mm}{s})$
0.5	7.2
1.0	3.6
1.5	2.4
2.0	1.8
2.5	1.4
3.0	1.2
3.5	1.0
4.0	0.9

5.5 Model Validation

Before finalizing the computationally generated results, the model was first analyzed for its accuracy. For this the pressure drop was considered as a parameter of comparison and subsequent validation. Similar to Li *et al.*, a 1-D pressure drop equation for fully developed laminar flow in a rectangular duct was utilized to approximate the pressure drop analytically $(\Delta P_{Analytical})$ [67]. The mean flow velocity as listed in Table 5.3 was included in Equation 5.5 for the respective channel aspect ratio. The velocity (v) was considered constant at all flow locations irrespective of the channel geometry:

$$\Delta P_{Analytical} = \frac{64\rho L_c v^2}{2 Re D_h}. \tag{5.5}$$

$$Re = \frac{\rho v D_h}{\mu}. \tag{5.6}$$

$$D_h = \frac{2 W_c H_c}{W_c + H_c}, \tag{5.7}$$

where Re and D_h are Reynolds number and hydraulic diameter of the flow in a duct and calculated using Equation 5.6 and Equation 5.7, respectively. After the evaluation of pressure drop $(\Delta P_{Analytical})$, the mesh size of the model was refined until the simulated pressure drop $(\Delta P_{Simulation})$ stabilized. The plot of mesh size versus

model generated pressure drop for the channel with the aspect ratio of 1 is presented

in Figure 5.3.
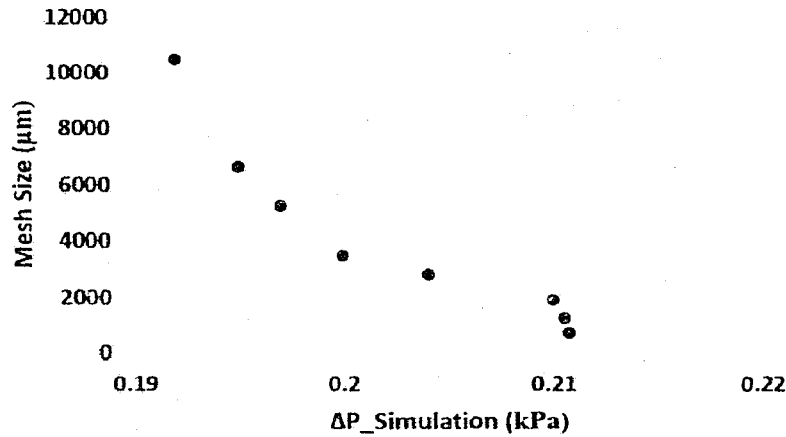
Figure 5.3: A plot of mesh size versus pressure drop.

The pressure drop approached stable value as the mesh size was reduced below

2000 μm. Table 5.4 summarizes the comparison of analytical versus simulated pressure

drop for the given mesh size of 1930 μm. The plot of $\Delta P_{Analytical}$ versus $\Delta P_{Simulation}$

for different aspect ratios is illustrated in Figure 5.4. The pressure drops for different

channel aspect ratios is summarized in Table 5.4.

Table 5.4: Summary of calculated and simulated pressure drops for different channel aspect ratios.

Aspect Ratio $\frac{H_c}{W_c}$	$\Delta P_{Analytical}$ kPa	$\Delta P_{Simulation}$ kPa
0.5	1.10	1.0
1.0	0.21	0.20
1.5	0.11	0.10
2.0	0.07	0.06
2.5	0.05	0.047
3.0	0.04	0.037
3.5	0.034	0.031
4.0	0.028	0.026
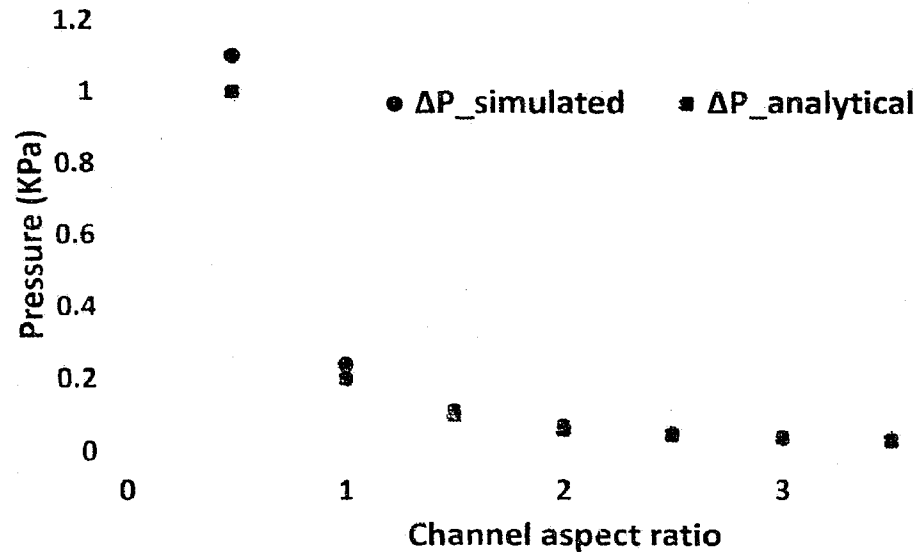
Figure 5.4: Comparison of analytical and simulated pressure drop for various aspect ratios.

The analytically calculated pressure drops along the length of the channel were comparatively higher than the model generated pressure drops. This was due to the inclusion of assumed uniform average fluid velocity along the channel in Equation 5.5 to calculate pressure drop. In real flow in a duct condition, the velocity of fluid varies from the wall to the midpoint of the channel. The velocity of the fluid is maximum at the center and decreases toward the wall. Also, the fluid experiences frictional force at the wall resisting its flow. These cases of flow variation and frictional forces at the walls were considered in model generated pressure drop results. Figure 5.5 and Figure 5.6 illustrates the model generated flow variation and temperature distribution along the channel and the geometry, respectively.
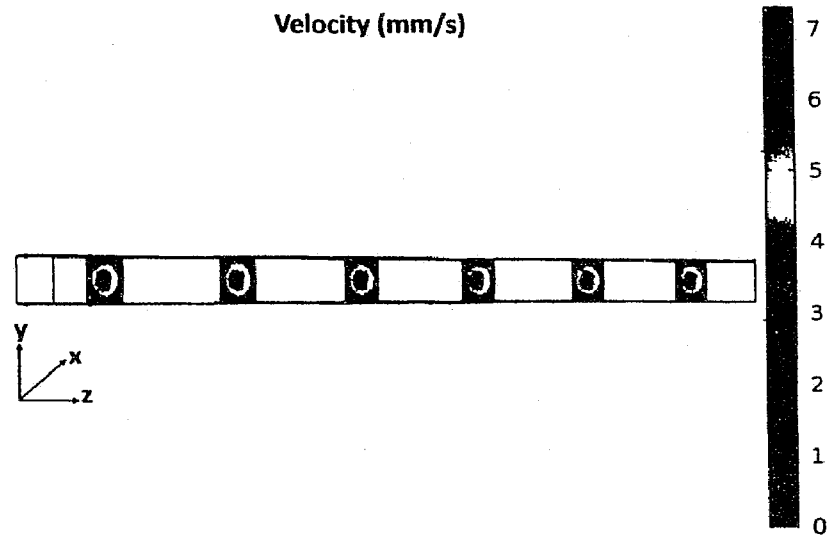
Figure 5.5: Velocity profile along the 100 μm wide by 100 μm high by 35 mm long channel (aspect ratio of 1:1).
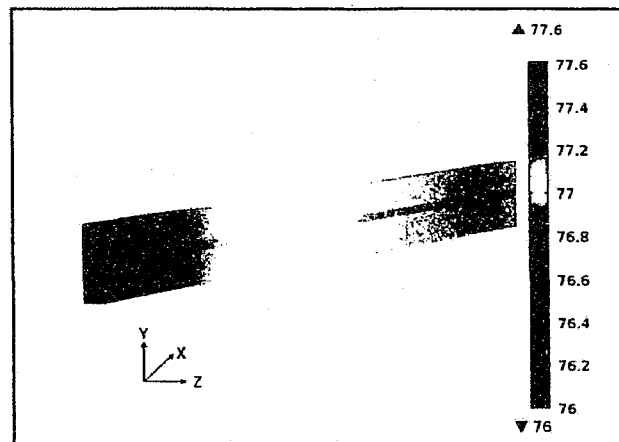
Figure 5.6: Temperature profile along the 100 μm wide by 100 μm high by 35 mm long channel (aspect ratio of 1:1).

5.6 Results and Discussion

A computational modeling was utilized to optimize the Superheater design. A model of the Superheater was designed using commercially available COMSOL software. The model was discretized into a finite number of nodes using FEM. The boundary conditions such as flow velocity, inward heat flux, convective cooling and

adiabatic were applied at specific locations in the model. The continuity, Navier-Stokes and heat equation were solved at each node. The pressure drop generated by the simulation for each aspect ratio was compared and validated with the corresponding analytically calculated pressure drop.

After the validation of the model, energy absorbed by the fluid and heat transferred from the bottom to the top of the single channel Superheater for different channel aspect ratios were studied. Energy absorbed by the fluid was calculated using Equation 5.8. Table 5.5 summarizes the energy absorbed by the fluid for different channel aspect ratios.

$$Q_{fluid} = (h_{outlet} - h_{inlet})j. \tag{5.8}$$

Table 5.5: Channel height versus Q_{fluid}.

Aspect Ratio $\frac{H_c}{W_c}$	j $\frac{kg}{m^2 s}$	Δh $\frac{kJ}{kg}$	Q_{fluid} $\frac{kW}{m^2}$
0.5	9.1	2.0	18
1.0	4.6	2.2	10
1.5	3.2	1.6	4.9
2.0	2.4	1.56	3.7
2.5	1.9	1.44	2.7
3.0	1.6	0.93	1.5
3.5	1.3	0.98	1.2
4.0	1.2	0.87	1.0

Where j is the mass flux rate, h_{outlet} is the enthalpy of fluid at the outlet of channel and h_{inlet} is the enthalpy of fluid at the inlet of channel. The model generated energy absorbed by the fluid and mass flux rate were combined using Equation 5.8 to evaluate energy absorbed by the fluid (Q_{fluid}). The energy flux for different channel aspect ratios are illustrated in Figure 5.7.
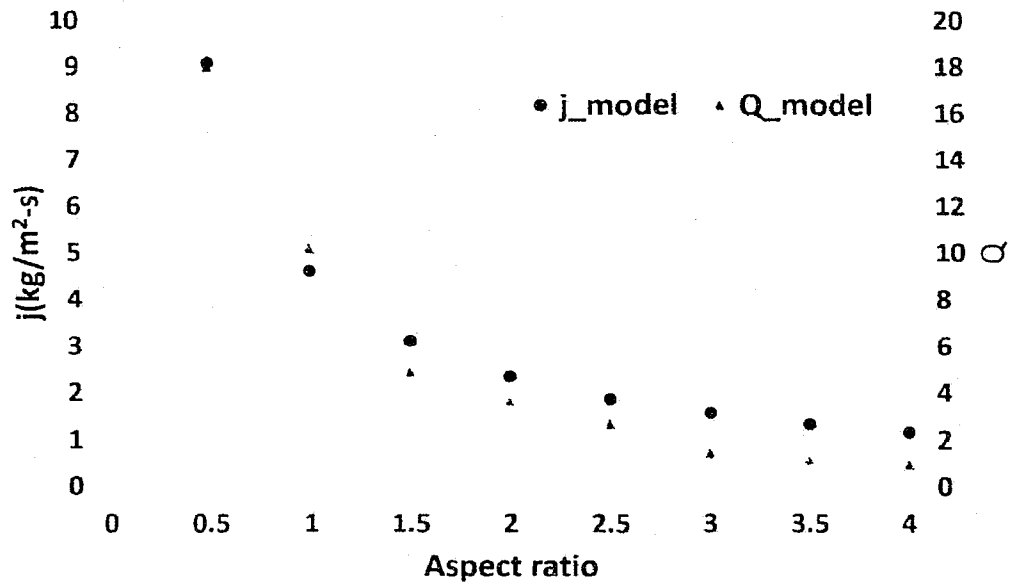
Figure 5.7: Plot of channel height versus energy flux

As illustrated in Figure 5.7, the energy flux is comparatively higher for the smaller channel area. For the 50 μm high channel (aspect ratio of 0.5), the energy flux is approximately 18 $\frac{kW}{m^2}$ and it decreased as the aspect ratio increased. This decrement is related to the mass flux. As the aspect ratio increased, the pressure drop along the channel decreased resulting in decrement of the mass flux. Also, the mass flux is proportional to the convective heat flux coefficient at the wall-fluid interference. This is illustrated by the plot of Nusselt number versus channel aspect ratio in Figure 5.8. The Nusselt number (Nu) was calculated using Equation 5.9:

$$Nu = \frac{h_{average} * D_h}{k} \tag{5.9}$$

where $h_{average}$ is convective heat flux coefficient and K is conductivity. The Nusselt number decreases with increase in channel aspect ratio.

4.50E+03 — 4
4.00E+03 — 3.5
3.50E+03 — 3   • h • Nu
3.00E+03 — 2.5
2.50E+03 — 2
2.00E+03 — 1.5
1.50E+03 — 1
1.00E+03 — 0.5
5.00E+02
0.00E+00 — 0

h(W/m2-K)   Nu

0   0.5   1   1.5   2   2.5   3   3.5   4   4.5
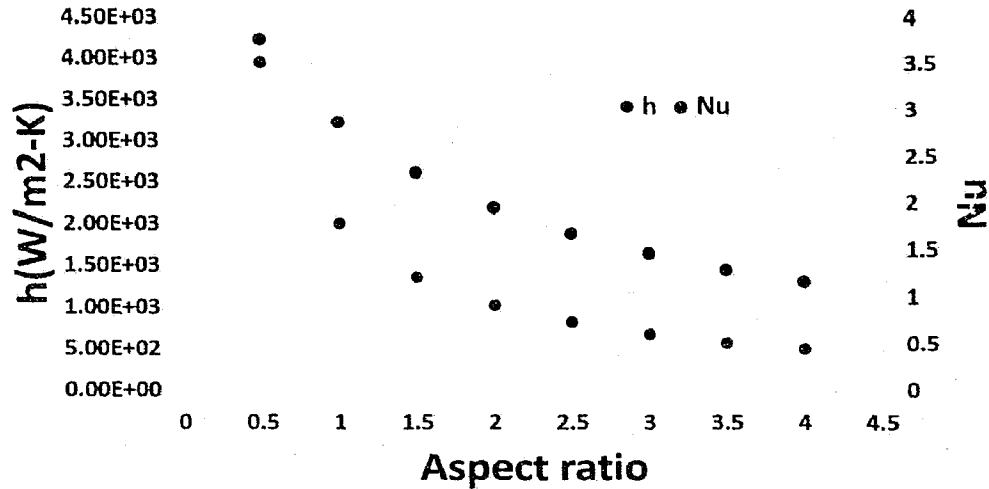
Aspect ratio

Figure 5.8: Plot of Nusselt number versus channel aspect ratio.

The value of Nusselt number evaluated for specific aspect ratio coincides with the available published data of Dharaiya *et al.* for fully developed flow in a rectangular microchannel [70]. Table 5.6 summarizes the Nusselt number found by simulation as well as available published data for varying aspect ratios of 0.5, 1 and 2. It can be visualized from Table 5.6 that the Nusselt number evaluated from numerical simulation are in good agreement with the Nusselt number from Dharaiya *et al.*

Table 5.6: Comparison of present work and proposed values by Dharaiya *et al.*

Aspect Ratio	From Reference [70]	Present work
0.5	3.744	3.765
1.0	2.884	2.867
2.0	1.928	1.952

Drop in operating pressure lowers the steam temperature (T_{max}) at the boiler side of the cycle and the overall efficiency of the cycle. This is given by Equation 5.10 and explained via general T-s (temperature- entropy) diagram in Figure 5.9. The T-s

diagram is not drawn to scale; however, it is included for the purpose of understanding the concept of pressure drop relation with temperature in a thermodynamic cycle:

$$\eta = 1 - \frac{Q_b}{Q_c} = 1 - \frac{T_{max}}{T_{condeser}} = 1 - \frac{T'_{max}}{T_{condeser}} \qquad (5.10)$$

where η is an efficiency, Q_{boiler} is the energy absorbed by the fluid, $Q_{condenser}$ is the heat rejected by the fluid, T_{max} is the temperature of the fluid, $T_{condenser}$ is the temperature of the condenser and T'_{max} is the lowered fluid temperature.

It can be visualized in Figure 5.9 that the efficiency of the thermodynamic cycle decreases with a decrease in operating pressure and temperature. Therefore, it is recommended to choose a Superheater with reasonable pressure drop along the channel and a maximum energy absorption flux rate. The channel aspect ratio of 1:1 could be favorable for the Superheater fabrication considering pressure drop and the heat flux rate (refer to Table 5.4 and Table 5.5). The pressure drop has decreased from 1 kPa for aspect ratio of 0.5 kPa to 0.2 kPa for an aspect ratio of 1:1, and also the energy absorption flux rate is about 10 $\frac{kW}{m^2}$. Moreover, the fluid exit temperature is 77.5 °C for the channel aspect ratio of 1:1.

The temperatures at the top of the Superheater as it interacts with the boiler for different channel aspect ratios were studied as well. The temperatures at the top of the Superheater for different aspect ratios are illustrated in Figure 5.10. It can be noted that the temperature at the top of the Superheater is comparatively higher for the aspect ratio of 1:1; however, the differences in temperatures are low.
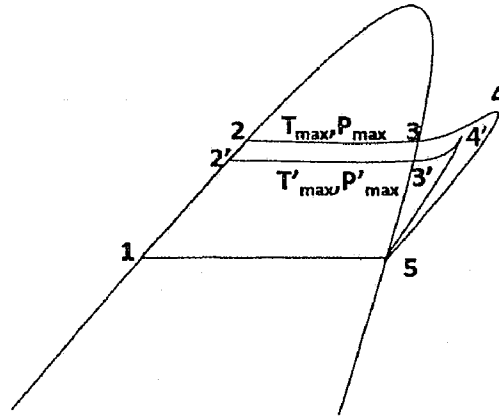
Figure 5.9: T-s diagram of an organic Rankine cycle showcasing decrease in a fluid temperature with pressure drop.
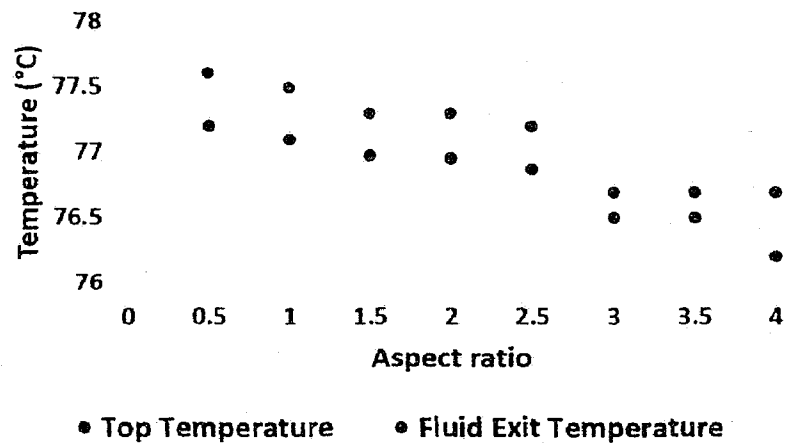
Figure 5.10: Plot of fluid exit temperature and Superheater top temperature for different channel aspect ratios.

5.7 Conclusion

This chapter is focused on subsequent redesigning of Superheater to form an integrated boiler/Superheater single system. The primary objective of the design is to utilize the same waste heat source to phase change the fluid and superheat the steam by placing the boiler atop the Superheater atop the heat source. Such a system design will allow increased space efficiency in real-world applications.

A computational modeling approach was considered to study the effects of design parameters on heat and mass transfer, temperature and pressure drop across the Superheater prior to fabrication and characterization. The input parameters to the model were based on the Superheater Test discussed previously. The results obtained from the modeling presented Superheater with an aspect ratio of 1 (100 μm height:100 μm width) favorable for the Superheater fabrication considering pressure drop and heat flux rate of 0.2 kPa and 10 $\frac{kW}{m^2}$, respectively. Moreover, the fluid exit temperature was 77.5 °C, which is comparatively higher than other considered aspect ratios.

CHAPTER 6

EXPERIMENTAL DEMONSTRATION OF AN EXHAUST HEAT RECOVERY BY A MEMS BASED BOILER

6.1 Overview

This chapter demonstrates the capability of a boiler to scavenge a real-world waste heat discarded from exhaust heat pipe experimentally. A copper foam works as a heat exchanger to extract thermal energy from the exhaust pipe and the trapped energy is made available to the integrated boiler/Superheater system presented in Chapter 4 and Chapter 5. The experimental setup designed to recover exhaust heat and the results obtained from the tests are summarized in detail.

6.2 Experimental Materials and Method

This section presents the design and fabrication of an Exhaust Heat Recovery System (EHRS). The EHRS consists of four components designated as Exhaust System (ES), Exhaust Heat Exchanger System (EHES), boiler, and Superheater. Each component was designed and fabricated separately. The fabricated components were then put together to form an EHRS. The test setup and the test procedure performed to study the EHRS are presented as well.

6.2.1 Exhaust System (ES)

Commercially available PH-1300 heat gun from ProHeat®served as a heat source. The heat gun was equipped with variable air temperature and flow control nobs. The maximum operating temperature and flow rate as specified by the ProHeat®were approximately 540 °C and 33 $\frac{kg}{hr}$, respectively. These maximum operating values were in the range with the test performed on a Fiat spark ignition engine (SIE) by Wojciechowski et al. [71]. The reported exhaust gas temperature and flow rate at 1600 rpm were approximately 500 °C and 35 $\frac{kg}{hr}$. Therefore, the heat gun utilized for the experiment will provide the real-world testing parameters.

A copper tube with an inner diameter of approximately 32 mm was chosen to fit the heat gun nozzle closely to the opening of approximately 32 mm. The copper tube served as an extension to the heated air flowing from the heat gun nozzle. The Reynolds number (Re) of the flow was then evaluated using Equation 6.1 to determine the flow type:

$$Re = \frac{\rho v_{avg} D_h}{\mu},$$ (6.1)

where ρ is the air density, v_{avg} is the average air velocity, D_h is a hydraulic diameter of the copper tube and μ is the dynamic viscosity. To allow the fluid flow inside the copper tube to be fully developed, the copper tube length greater than ten times the hydraulic diameter was considered [72]. In the present case, a diameter of the tube is the hydraulic diameter. The copper tube with a length ten times its diameter was considered. Therefore, a tube with a length of 160 mm was cut and attached to the heat gun nozzle using a flexible duct connector. The tube was then insulated

with foam insulator to minimize heat loss from the outside surface of the tube to the surroundings. Figure 6.1 shows the readied Exhaust System that includes heat gun and insulated copper tube.
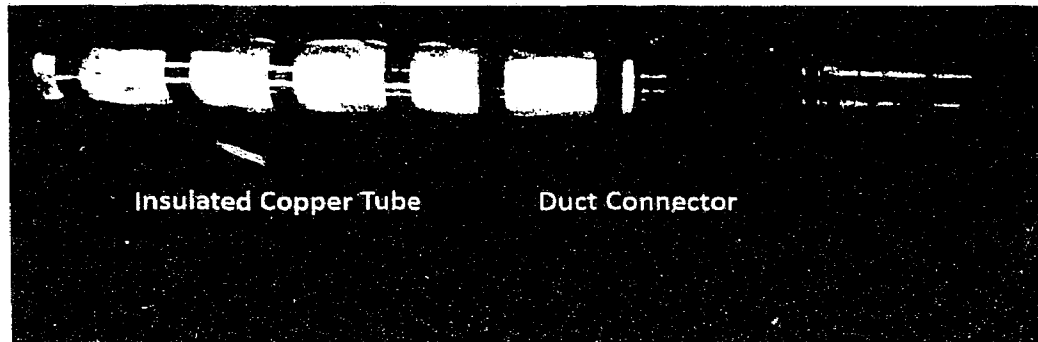
Figure 6.1: The exhaust system: heat gun and insulated copper tube.

6.2.2 Exhaust Heat Exchanger System (EHES)

A copper foam was utilized as a heat exchanger to extract thermal energy from the Exhaust system discussed in Section 6.2.1. The heated air forced via the copper tube was allowed to traverse the copper foam connected at the opening end of the tube. The trapped heat by the copper foam was made available to the integrated boiler/Superheater system in contact. In detail, fabrication as well as the test setup of the boil. and Superheater is presented in the following sections. However, this section is specifically focused on the design and fabrication of EHES.

A metal foam made of copper was chosen for heat exchanger construction because it provides a large heat transfer area per unit volume and enhanced flow mixing capabilities suitable for heat exchanger design [73]. Therefore, the foam type heat exchanger has been gaining more interest in thermal management applications [73, 74]. The copper foam is generally characterized by two parameters, the volumetric

porosity density (ε) and pores per linear inch (PPI) [73]. The volumetric porosity is the ratio of total void volume to cumulative volume occupied by the solid matrix and void space. Based on these parameters, the heat transfer characteristic of copper foam with varying PPI and porosity has been reported experimentally as well as numerically by various researchers [75, 76, 74, 77].

The copper foam with approximately 89% porosity and 40 PPI was utilized for the construction of EHES. The copper foam was supplied by ERG Duocel®. The copper foam of 14 mm in length by 100 mm in breath by 100 mm in height was diced using Proxxon 27127 Micro Band Saw to yield two copper foams of 14 mm in length by 35 mm in breath by 35 mm in height, and a copper foam of 7 mm in length by 35 mm in breath by 35 mm in height. The overall dimension of the three copper foams together was 35 mm in length by 35 mm in width by 35 mm in height. These specific dimensions were chosen to match the boiler base dimension of 35 mm in length by 35 mm in breath and the exhaust copper outer tube diameter of 34 mm.

In addition to the copper foam, two copper sheets of dimensions 35 mm in length by 35 mm in breath by 0.8 mm in height were cut as well. These copper plates served as a base and top holding the three sandwiched copper foams together (refer Figure 6.2). The copper foams and plates were cleaned using two steps ArtiClean thermal material remover and surface purifier from Artic Silver®. After the thermal cleaning, a thin layer of two-part Artic Silver Thermal Adhesive from Artic Silver® was applied to each copper plate. The thermal adhesion was utilized instead of generic epoxy to minimize thermal contact resistance between the copper foams and plates. The copper plates with thermal adhesive were placed at the top and bottom of the

sandwiched copper foams and then the copper foams and plates were clamped in place. The clamped sample was left to cure for about 24 hours to ensure proper adhesion.
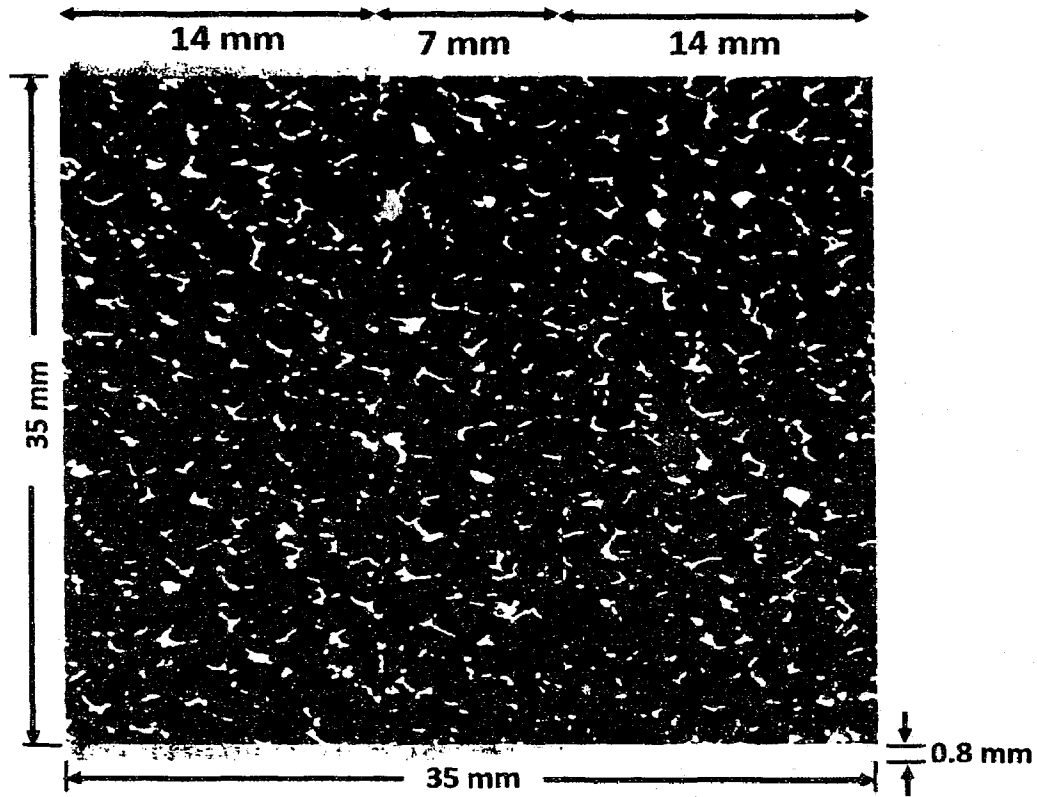
Figure 6.2: The copper plates at the top and bottom of the three sandwiched copper foams.

After the fabrication of the copper sample, a box-like casing was designed to contain the fabricated copper heat exchanger sample. Commercially available SOLIDWORKS software was utilized to design, and a 3D printer from LuzBot®was used to print the finalized design. The design included a chamber of size 35 mm by 35 mm by 35 mm to insert the fabricated sample, the holes at two opposite sides to allow exhaust gas to flow in and out via the chamber, an exposed top side of a copper plate facing outward, and a closed bottom side. Figure 6.3 presents a detailed visual description of the design with dimensions for further understanding.
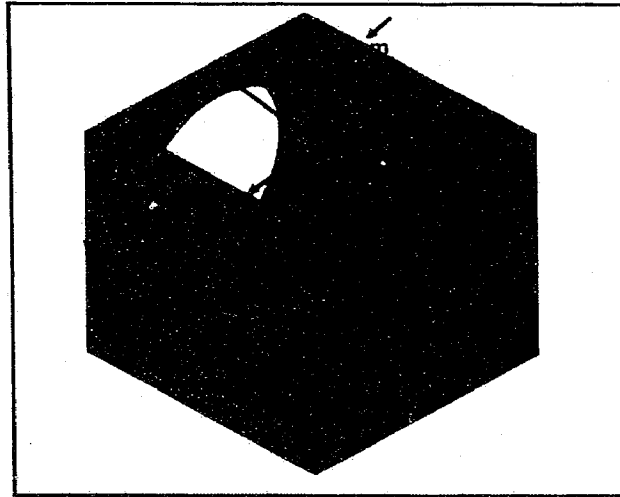
Figure 6.3: An image of the SOLIDWORKS designed casing.

As mentioned previously, a 3D printer was utilized to print the designed casing. A High Impact Polystyrene (HIPS) was used as a printing material. Figure 6.4 shows the printed casing along with the copper sample of size 35 mm by 35 mm by 35 mm inserted into the chamber. The overall dimension of the HIPS casing was 49 mm by 49 mm by 42 mm. The wall at the bottom and the sides of the casing were 7 mm. The top side of the casing was left open to mount the integrated boiler/Superheater system (see Figure 6.4). The diameter of the circular hole was 34 mm to allow the copper pipe with an outer diameter of 34 mm to fit in tightly.
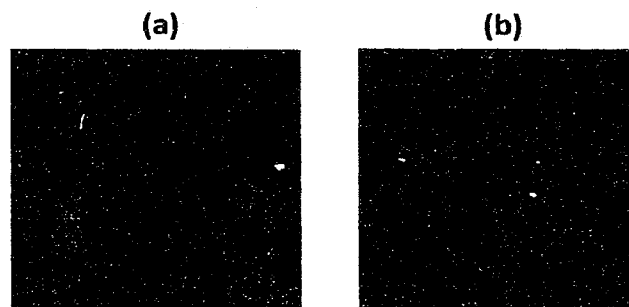
Figure 6.4: Image showcasing: side view (a) and top view (b) of the 3D printed HIPS casing with copper sample inserted into the chamber.

6.2.3 Boiler and Superheater

6.2.3.1 Boiler Fabrication

The boiler consists of circular capillary channels surrounded by rectangular reservoirs for the continuous supply of fluid at the bottom and the glass steam collecting dome at the top. The fluid flow from the reservoirs to the heated channels is achieved by the capillary action of the channels. A detailed explanation of the design and working principle of the boiler has been presented in previously published boiler characterization work [35, 56, 23]. However, in this section, the fabrication steps of the boiler is specifically explained.

The boiler was fabricated using MEMS technology in a microfab lab with cleanroom facilities here at Louisiana Tech University. The boiler consisted of two individually fabricated components, a silicon etched boilerplate and a glass covering steamdome. The fabricated components were then anodically bonded together to foam the boiler. The dimensions of the fabricated boiler were approximately 35 mm in length by 35 mm in breadth by 1 mm in height. The channel depth and width were kept constant to approximately 190 μm and 100 μm, respectively.

Initially, a photolithographic mask was designed using L-edit software and printed (refer to Figure 6.5). The boilerplate was fabricated by etching a standard 4 inch type $< 100 >$ silicon wafer. An Inductive Coupled Plasma (ICP) etching technique was utilized to etch silicon and form channels and reservoirs in the boilerplate with an etch rate of approximately 2 to 3 $\frac{\mu m}{min}$ at constant ICP power supply. The total etch time to produce 190 μm deep channels and reservoirs were evaluated to be above an hour considering the ICP etch rate. A silicon wafer coated with photoresist as

an etch resist mask alone may not be able to withstand the ionized gas inside the
ICP etch chamber for such a long exposure time. Therefore, a thin aluminum layer
of approximately 200 nm was e-beam evaporated on one side of the bare silicon
wafer. The aluminum layer along with photoresist will serve as an etch stop mask
in the subsequent boiler fabrication process. S1813, a positive type photoresist was,
considered for this work.
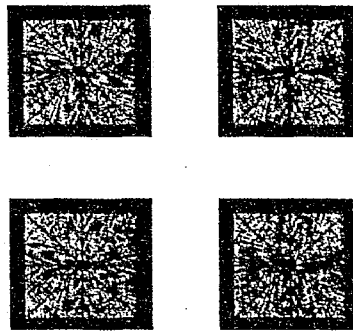
Figure 6.5: An image of a mask designed using L-edit software.

A silicon wafer was cleaned using acetone to remove any organic particles
present on the wafer's surface. The wafer was then immediately soaked in isopropyl
alcohol (IPA) to remove any stains left by acetone. After stain removing, the wafer
was rinsed well with deionized water and blown dry with a nitrogen stream. The
cleaned wafer was dehydrated by heating the wafer in a hotplate at 200 °C for about
20 minutes. This dehydration step will facilitate better adhesion of photoresist to the
wafer's surface. The dehydrated wafer was spin-coated at a maximum spinning speed
of 3000 revolution per minute (RPM) to form 1 μm thick layer of photoresist atop the
aluminum coated side of the wafer. The coated wafer was soft baked in a hotplate at

115 °C for about 90 seconds to vaporize the liquid present in the photoresist. This will improve bonding between the photoresist molecules itself and to the wafer surface as well.

The soft baked wafer was exposed to ultraviolet (UV) rays through a mask using a photolithographic mask aligner. The mask was designed to allow UV light to pass through the channel and reservoir features. The exposed portion of the photoresist through the mask became soluble in the developer due to the change in molecular structure. The exposed wafer was then soaked in MF-319 developer for 30 seconds to strip off the soluble portion of the photoresist atop the aluminum leaving imprints of circular channels and reservoirs. The aluminum was etched using aluminum enchant exposing silicon at channels and reservoirs. The wafer was etched to strip off the silicon to form channels and reservoirs in the wafer. SEM image of the fabricated boilerplate is shown in Figure 6.6 [23].

Figure 6.6: SEM image of the ICP etched channels.

The steamdome was fabricated by etching a glass wafer with dimensions similar to the silicon wafer. The use of approximately 500 μm thick glass presented a significant mass reduction as compared to the acrylic steamdome utilized in prior work [35, 56].

Furthermore, the use of glass steamdome demonstrated a significant increase in boiler energy conversion efficiency [23].

An e-beam evaporator was utilized to coat a 200 $\overset{\circ}{A}$ thick layer of chrome on both sides of the glass wafer. A gold layer of thickness 200 $\overset{\circ}{A}$ was then e-beam evaporated on both sides atop the chrome coating. This process of coating chrome and then gold was performed again to form chrome-gold-chrome-gold layers on both sides of the wafer. Such an arrangement of layers was to ensure proper etch stop against strong hydrofluoric acid utilized to etch glass. A positive photoresist, S1813, was-spin coated on both sides of the wafer. The wafer was soft baked at 115 °C for approximately one and a half minutes. The baked wafer was exposed and developed, leaving imprints of the steam collecting dome and the reservoirs compartments on one side (front). After the development, the other side of the wafer (back) was aligned to the previously exposed side using the back side alignment (BSA) technique to form the inlet and the outlet holes exactly at the reservoir and steam collecting dome, respectively. The aligned back side of the wafer was exposed and developed. The chrome-gold-chrome-gold layers at the developed surfaces on both sides of the wafer were removed using chrome and gold etchant. Finally, the exposed glass after the removal of chrome and gold layers at the developed surfaces were etched using an aqueous solution of hydrofluoric acid with an etch rate of 5 $\frac{\mu m}{min}$. A diagram of the steamdome design is shown in Figure 6.7 [23].
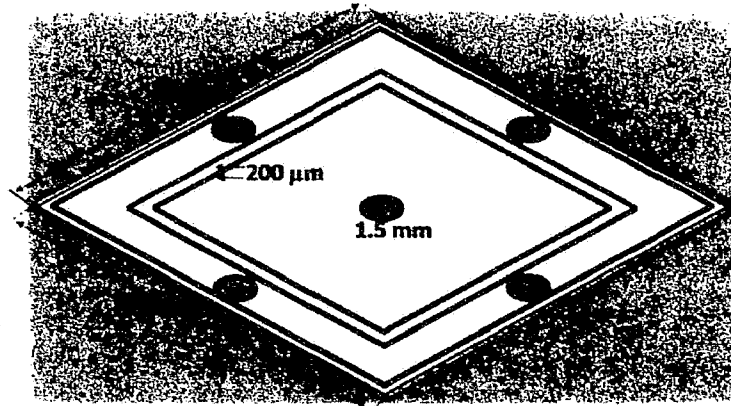
Figure 6.7: A glass steamdome.

The fabricated boilerplate and steamdome were anodically bonded to form the boiler. The bonding was performed using a hot plate and a pair of aluminum plates connected to a voltage supply. Prior to the bonding process, the boilerplate and the steamdome were cleaned utilizing RCA-I and RCA-II techniques to free the bonding surfaces from any organic and inorganic contamination [58, 59].

After the cleaning process, the hot plate was preheated to 400 °C. The bonding surfaces of the boilerplate and the steamdome were held in place using a pair of aluminum plates. The aluminum supported boilerplate and steamdome were placed on the hotplate. Initially, 400 volts was supplied to the bonding setup with the positive terminal connected to the silicon side [59]. The bonding surface was visually inspected every 5 minutes to evaluate the bonding progress. In the case of slow bonding progress based on the inspection, the voltage was increased to a maximum of 700 volts to minimize bonding time [78]. In this way, the bonded boiler was obtained after approximately 15-30 minutes. Figure 6.8 shows the boiler formed by bonding with enclosed chambers for working fluid and steam [23].
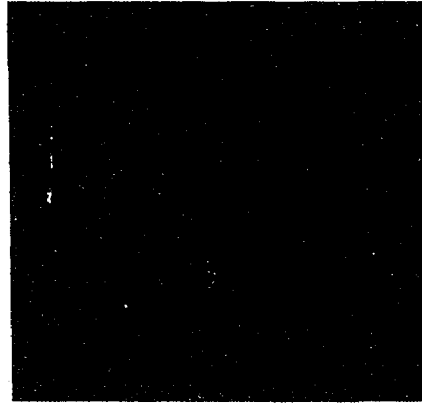
Figure 6.8: The boiler.

The components such as micro tube and "T" shaped tubing were attached to the fabricated boiler. A microtube of 1/16 inch diameter was attached to the reservoirs through the inlet hole (refer to Figure 6.8). A "T" shaped tubing from McMaster-Carr was attached to the exit hole atop the steam collection dome. A thermocouple (TC) was inserted into the "T" tubing opening in line with the exit hole and then sealed using epoxy to monitor the phase changed fluid temperature. The "T" tubing opening perpendicular to the exit hole served as an outlet for the vapor to exit the boiler.

6.2.3.2 Superheater Fabrication

Similar to the fabrication of copper foam heat exchanger in Section 6.2.2, a copper foam and a copper plate were utilized to fabricate the Superheater heat exchanger. A copper foam of 35 mm length by 35 mm in breath by 3 mm in height and a copper plate of 35 mm in length by 35 mm in breath by 0.4 mm in height were cut using a MICRO Band Saw. Each cut piece was cleaned with two step ArtiClean thermal material remover and surface purifier. A thin layer of two-part Artic Silver Thermal Adhesive was applied to the copper plate. The copper plate was then placed

atop the copper foam. The copper foam and plate were held in place with a clamp support. The clamped sample was left to cure for about 24 hours to allow proper adhesion (refer to Figure 6.9 (a)).
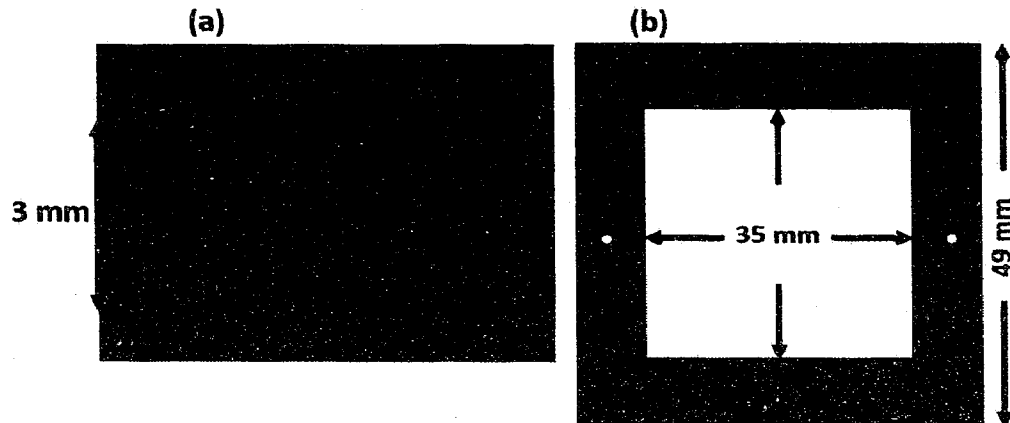
Figure 6.9: An image showing a copper foam and a copper plate glued together to form a Superheater (a) and a designed Superheater casing with hollow section at the center (b).

A casing with overall dimensions if 49 mm by 49 mm by 5 mm with a hollow section with dimensions 35 mm by 35 mm by 5 mm in the middle was designed and printed to insert the Superheater heat exchanger of dimension 35 mm by 35 mm by 3.4 mm (refer to Figure 6.9 (b)). An additional height of about 1.6 mm was considered in the casing design to allow the boiler to fit atop the Superheater heat exchanger. Inlet and outlet holes of diameter 1/16 inch were drilled through the 7 mm thick walls at the two opposite sides of the casing. These holes will facilitate the vapor exiting from the boiler to enter the Superheater through a micro tubing connection during testing. The vapor will then traverse the Superheater heat exchanger and exit the casing via a drilled outlet hole. Two holes were drilled at the top and the side of each previously drilled hole to incorporate thermocouples and pressure sensors (refer to Figure (b)

6.9). The incorporated thermocouples and pressure sensors will provide temperature
and pressure readings of the vapor entering and exiting the Superheater.

6.2.4 Exhaust Heat Recovery Experimental Setup and Procedure

This section presents a detailed explanation of the components assembled
to form the Exhaust Heat Recovery System (EHRS) (refer to Figure 6.10). The
components included Exhaust System (ES), Exhaust Heat Exchanger System (EHES),
boiler and Superheater. The sensors such as thermocouple (TC), pressure, heat flux
(HFS) and air velocity meter were added to monitor the parameters required to
study and characterize the EHRS. The recording of the reading was achieved using
SingnalExpress software via National Instrument Data Acquisition (NI-DAQ) device.
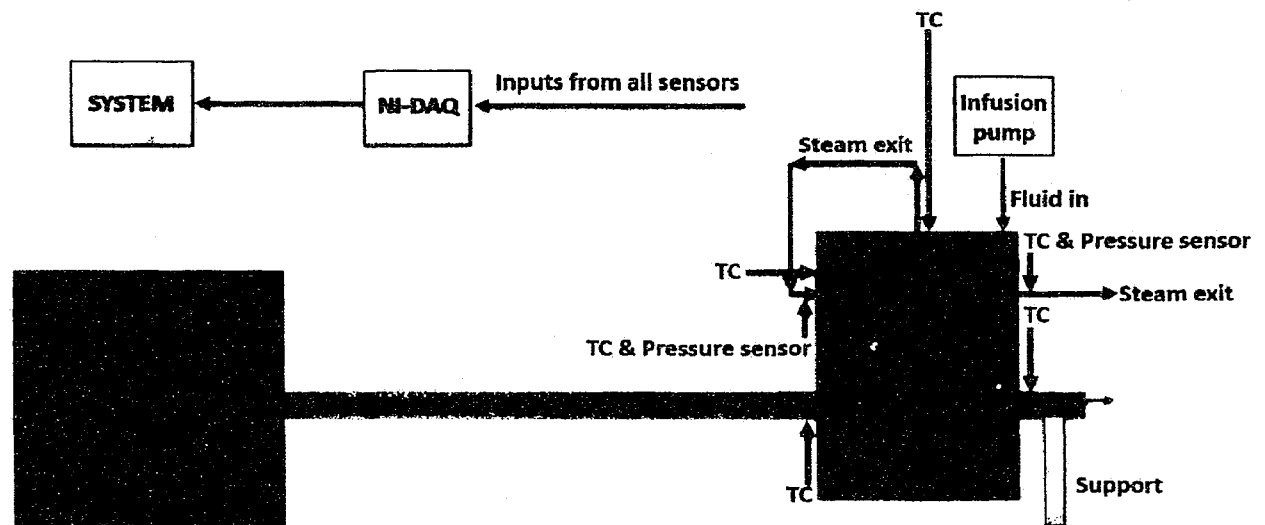
Figure 6.10: The Exhaust Heat Recovery System: Exhaust System, Copper Foam
Based Heat Exchanger, Boiler, Superheater, and Sensors.

The copper tube connected to the heat gun was inserted into the inlet circular
hole of the copper sample casing. An additional copper tube of length approximately
50 mm was inserted into an outlet to the air exiting the casing (refer to Figure

6.10); 1/16 inch holes were drilled into the copper tubes next to the inlet and the outlet of the Exhaust Heat Exchanger System (EHES) casing. Two 1/16 inch probe TCs (OMEGA®) were inserted into the drilled hole and sealed to monitor the air temperature flowing in and out of the casing. After this assembly of the Exhaust System and the Exhaust Heat Exchanger System (EHES), two tests were performed on the setup. Detailed explanation of the tests performed on the assembled system is presented in following sections.

6.2.4.1 Boiler Test

Unlike the experimental setup shown in Figure 6.10, the boiler was mounted atop the EHES HIPS casing instead of the Superheater. In other words, the Superheater was excluded from the test setup for this specific test. The coupling of the boiler to the heat exchanger copper plate was achieved using double-sided polyimide tape from $3M^{TM}$. During coupling, a heat flux sensor (HFS) and a thermocouple (TC) were sandwiched between the boiler and the copper plate to monitor the heat flux absorbed by the boiler and the temperature at the bottom of the boiler, respectively. The test provided an insight into the ability of the boiler to scavenge heat and phase change the working fluid from an exhaust heat source. Furthermore, the effect of variation in working fluid supply rates and the affect variation in exhaust air velocity itself in boiler energy absorption were investigated.

The boiler test began with the determination of the minimum temperature required to change the working fluid to vapor. $3M^{TM}$ HFE-7200 refrigerant served as a working fluid for all tests independent of test types. This fluid was used for numerous

advantages such as boiling temperature of 76 °C appropriate for low-temperature heat scavenging applications [62], high heat of vaporization [36], high wettability with surface and low environmental impact [36]. The determination of operating temperature was based on prior work [56, 23]. This was achieved by matching the boiler bottom temperature to the value reported previously. The reported boiler bottom temperature and working fluid supply rate to the boiler are summarized in Table 6.1 [56, 23].

Table 6.1: The temperature and the working fluid flow rate from prior work.

Temperature (°C)	Flow rate (mg/s)
104	9

The heat gun was turned on after setting the air temperature and flow adjusting nobs to minimum reading. The temperature of the air entering and exiting the EHES HIPS casing, the temperature at the bottom of the boiler and the heat flux were recorded. The air temperature traversing through the copper sample was raised by increasing the temperature nob reading of the heat gun in steps. This raised the boiler bottom temperature. The temperature of the air was increased until the boiler bottom attained the steady state temperature close to 104 °C. The working fluid was then introduced to the boiler via an infusion pump (KD Scientific). The infusion pump was utilized for the fluid supply to achieve accurate, continuous and repeatable fluid flow rate which may not have been viable with manual pumping otherwise. The fluid feed rate of 9 $\frac{mg}{s}$ was supplied to the boiler based on the prior boiler work (refer to Table 6.1). The vapor temperature, the boiler bottom temperature, the temperature

of the air at inlet and outlet of the EHES HIPS casing, ambient temperature, the temperature at an outside of the casing and the absorbed heat flux were recorded. Figure 6.11 shows a typical temperature profile of the recording before and after the introduction of the working fluid at the specific location represented by the legend.

—Air_out —Air_in —Casing_wall —Ambient —Vapor_boiler — Boiler_bottom
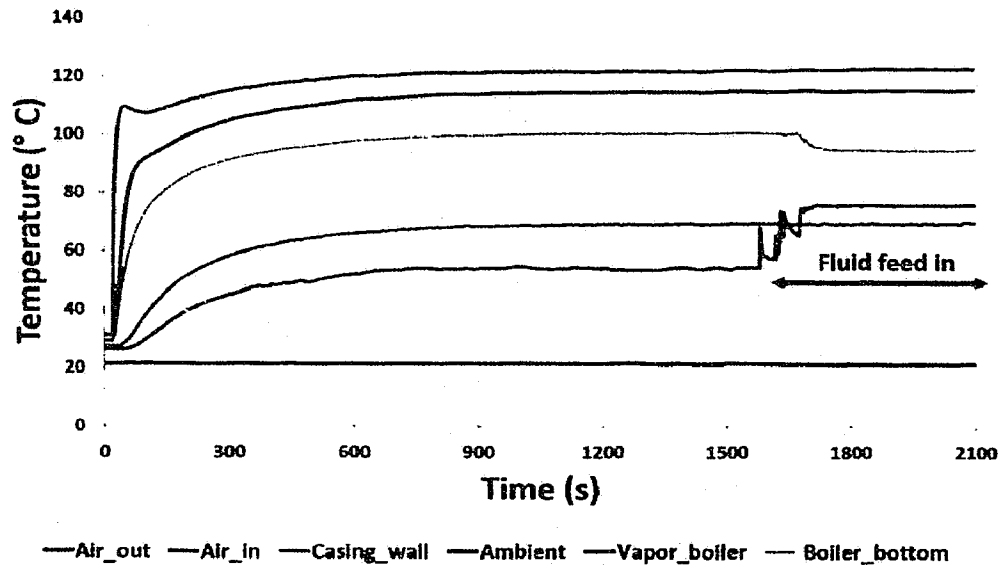
Figure 6.11: The temperature profile at various location of the test setup.

The setup was allowed to attain steady state temperature before adding working fluid to the boiler. It can be verified by inspecting temperature profiles in Figure 6.11. The system requires about 25 minutes of warm-up period to attain a steady state. This initial warm-up of the system prior to addition of the fluid and data collection was maintained for all tests independent of test types. After obtaining stead state temperature, the fluid addition part of the temperature profile presented a phase transformation of the working fluid from liquid to vapor represented by legend vapor in Figure 6.11. The phase changed vapor inside the steamdome attained the temperature of about 76 °C, which is the boiling temperature of the HFE-7200 refrigerant. In this

way, the temperature required to operate the boiler was determined. This working temperature was maintained for all tests.

After the determination of boiler operating temperature, tests were performed to select air flow velocities. The selected air flow velocities will serve as operating conditions to characterize and compare the boiler operation. The test began with disassembling the Exhaust System from the EHES HIPS casing. The disassembled Exhaust System (heat gun along with copper tube extension) was alone utilized for these specific tests. A probe type sensor extending from the air velocity meter was inserted into the opening of the copper tube (OMEGA®). The probe was then held in place using a clamp support. The heat gun was turned on with the temperature nob fixed to the previous test reading and the velocity nob at minimum reading. The air velocities at two different locations of the nob were considered for testing. For each location of the velocity nob, air velocities at four equidistant points extending from the wall to the center of the copper pipe were noted. The noted velocities at equidistant points were combined using Equation 6.2 to determine the average velocity (v_{avg}) of the air inside the tube [72]:

$$v_{avg} = \frac{2}{R^2} \int_0^R v(r) r \, dr, \tag{6.2}$$

where R is the radius of the copper tube, v(r) is the velocity profile of air flowing inside the tube, and r is the considered radius of the tube. The evaluated operating velocities were 0.92 $\frac{m}{s}$ and 1.2 $\frac{m}{s}$. These velocities will be designated as low velocity (V_{low}) and high velocity (V_{high}) for an ease of the explanation, respectively. After

the evaluation of velocities, the Exhaust System and the EHES were reassembled to perform tests on the boiler.

With the operating temperature and velocities known, a set of tests was performed on the boiler with each evaluated velocity. Beginning with the low-velocity testing, the heat gun was powered and the setup was allowed to attain steady state temperature. The temperatures of the boiler bottom, air entering and leaving the EHES HIPS casing, phase changed vapor, HIPS casing outer walls and ambient air were recorded. In addition to temperature, the readings from HFS was recorded as well to determine the thermal energy absorbed by the boiler to phase change the working fluid.

The working fluid was then supplied to the boiler. A set of four experiments was performed with varying flow rates to study the effect of varying fluid supply rates in thermal energy absorption of the boiler. The test protocol of fluid addition following the 25 minutes warm-up was carried out for each experiment. The fluid feed rates utilized for testing were $3\ \frac{mg}{s}$, $6\ \frac{mg}{s}$, $9\ \frac{mg}{s}$ and $13\ \frac{mg}{s}$. Similarly, the tests were repeated for V_{high} as well. These tests provided an understanding of boiler capability to extract thermal energy to phase transform the working fluid and the effect of varying working fluid rates in energy absorption by the boiler. In addition, the effect of varying exhaust air velocity in boiler thermal energy was studied as well.

The energy balance was performed on the test setup to study the amount of energy trapped by the EHES heat exchanger from the heated air traversing it (E_{EHES}), the energy absorbed by the boiler from copper heat exchanger via conduction to phase change the working fluid (E_{boiler}), and the energy lost from the HIPS casing via

convection to surrounding (E_{loss}). The energy balance was achieved using Equation 6.3 for each air velocity. The value for E_{boiler} was supplied by the heat flux sensor sandwiched between the boiler and the copper plate of the copper foam heat exchanger. The values for (E_{EHES}) and E_{loss} were evaluated using Equation 6.4 and Equation 6.6, respectively. The mass flow rate ($\dot{m}$) of the air required in Equation 6.4 was determined by multiplying air density (ρ), the average velocity of air calculated using Equation 6.2 and the cross section area of the copper tube (refer to Equation 6.5).

$$E_{EHES} = E_{boiler} - E_{loss}. \tag{6.3}$$

$$E_{EHES} = \dot{m}C_p(T_{in} - T_{out}). \tag{6.4}$$

$$\dot{m} = \rho V_{avg} A_{cs}. \tag{6.5}$$

$$E_{loss} = E_{EHES} - E_{boiler}, \tag{6.6}$$

where C_p is the air specific heat at constant pressure, T_{in} is the air temperature flowing in the EHES casing, T_{out} is the temperature of air leaving the EHES casing.

6.2.4.2 Integrated boiler/Superheater Test

The boiler along with the Superheater was included in this test. Figure 6.1 shows the experimental setup readied for testing. The fabricated Superheater in Section 6.2.3.2 was mounted atop the copper plate of the EHES casing. The HIPS casings were glued together to held in place (refer Figure 6.12). The coupling of the boiler to the Superheater was achieved using double-sided polyimide tape. During coupling, a heat flux sensor (HFS) and a thermocouple (TC) were sandwiched between

the boiler and the Superheater to monitor the heat flux absorbed by the boiler and the temperature at the bottom of the boiler, respectively. The outlet of the boiler and the inlet of the Superheater were connected with a micro tubing of diameter 1/16 inch. A microtube of a similar diameter was inserted into the Superheater outlet for the vapor to exit. The pressure sensors and TCs were included to monitor the vapor temperature and pressure entering and leaving the Superheater. This test provided a preliminary operational understanding of an integrated boiler/Superheater system sourced with a single heat supply.
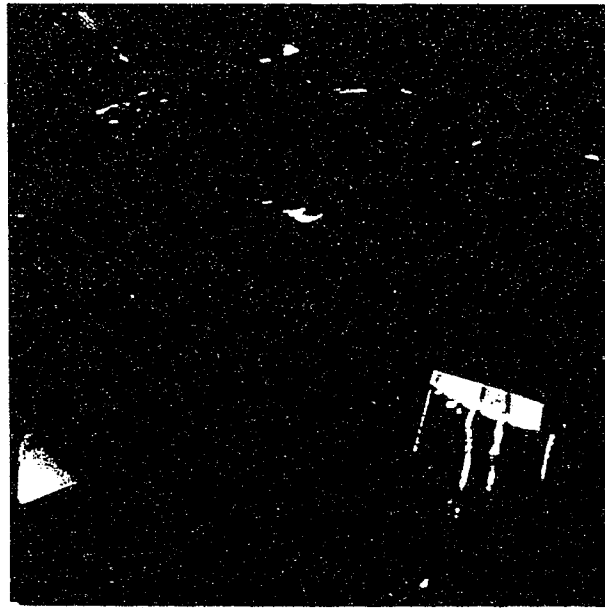
Figure 6.12: Superheater mounted atop the HIPS copper foam casing and epoxied in place.

Similar to the previous test, the boiler bottom temperature was maintained around 104 °C. This was achieved by raising the air temperature flowing through the EHES with flow rate fixed at V_{low}. The temperature of the air was determined and the temperature nob of the heat gun was fixed for the test.

The test began with an initial warm-up of the system for about 25 minutes to attain steady state temperature. The temperature readings of the air entering and leaving the EHES casing, boiler bottom, phase changed vapor inside steamdome, steam at Superheater inlet and outlet, casing outer walls and ambient air were recorded. The readings from the HFS sensor sandwiched between boiler and Superheater was recorded as well. The working fluid was introduced to the boiler. The phase changed vapor exiting the boiler was allowed to enter and leave the Superheater via connected tubing. The tests were conducted with various fluid supply rates and the effect of the fluid flow in boiler energy absorption and the vapor temperature at inlet and outlet of the Superheater were studied.

6.2.5 Experimental Error

Kline and McClintock's uncertainty analysis was utilized to evaluate the error associated with the test data [38]. Error associated with temperature, mass of the fluid and time were on the order of $\pm$ 0.5 °C, $\pm$ 0.005 g and $\pm$ 1 second, respectively. The error associated with each individual flow rate was determined to be in the order of $\pm$ 0.56 $\frac{mg}{s}$. The error associated with the pressure reading was $\pm$ 0.5 kpa. The error associated with the air velocity was $\pm$ 0.38 $\frac{m}{s}$. The error associated with the energy calculation was $\pm$ 0.01 watts.

6.3 Results and Discussion

The individually fabricated components as explained in Section 6.2 were assembled to form an Exhaust Heat Recovery testing system. The components included Exhaust System, Copper Foam Heat Exchanger System, boiler and Superheater. In

addition, thermocouples (TCs), pressure, heat flux sensor (HFS) and air velocity meter were incorporated in the system to monitor the parameters required to study the boiler capability to scavenge thermal energy from the exhaust air via the copper foam heat exchanger to phase transform the working fluid. Furthermore, an investigation of integrated boiler/Superheater system was carried out to study the ability of the integrated system to phase transform the working fluid and then superheat the vapor exiting the boiler utilizing single heat source. Figure 6.13 shows the sensors situated at the various location of the test setup.
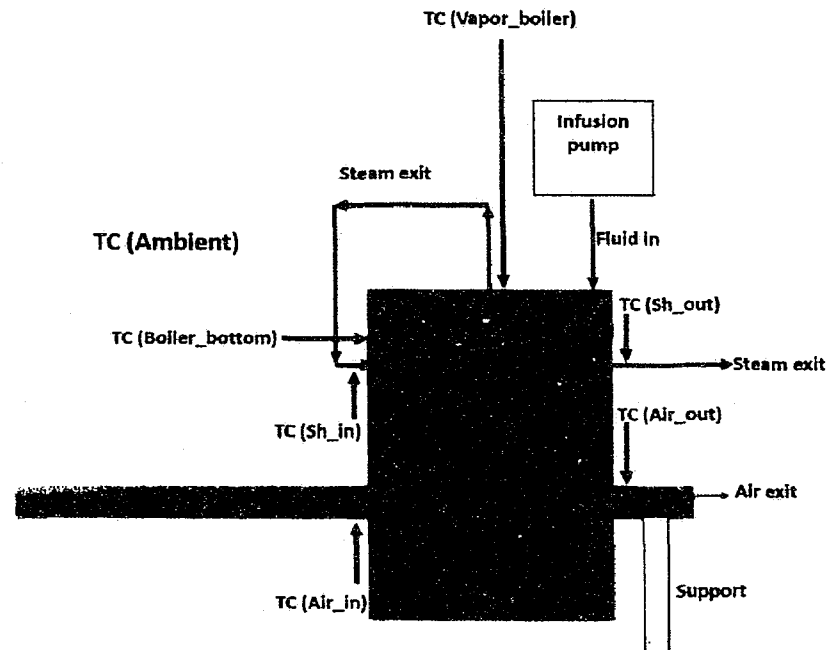
Figure 6.13: Senors location in the test setup.

6.3.1 Boiler Test

Detail explanation of the experimental setup is presented in Section 6.2.4.1. In this test, the boiler ability to absorb thermal energy trapped by a copper foam heat exchanger from an exhaust gas to phase change the working fluid was investigated.

The results obtained by varying the working fluid supply rate and the flow velocity of air itself are presented and discussed in this section. The working temperature of about 104 °C was set at the bottom of the boiler based on prior work. The testing began with the exhaust air velocity set to V_{low}, the test setup was initially heated for about 25 minutes to attain steady state temperature. The readings from the TCs located at the boiler bottom, inlet and outlet of the EHES HIPS casing, steamdome, HIPS casing outer walls and ambient air were recorded. The thermal energy absorbed by the boiler via conduction was monitored using HFS. The working fluid was then introduced to the boiler via infusion pump. A set of four tests were conducted with flow rates of 3 $\frac{mg}{s}$, 6 $\frac{mg}{s}$, 9 $\frac{mg}{s}$, and 13 $\frac{mg}{s}$. The temperature and the heat flux for the working fluid flow rate of 9 $\frac{mg}{s}$ are presented in Figure 6.14 and Figure 6.15.

Figure 6.14: Temperature profile obtained at various location of the experimental setup with exhaust air flow rate of 0.92 $\frac{m}{s}$ and refrigerant supply rate of 9 $\frac{mg}{s}$.
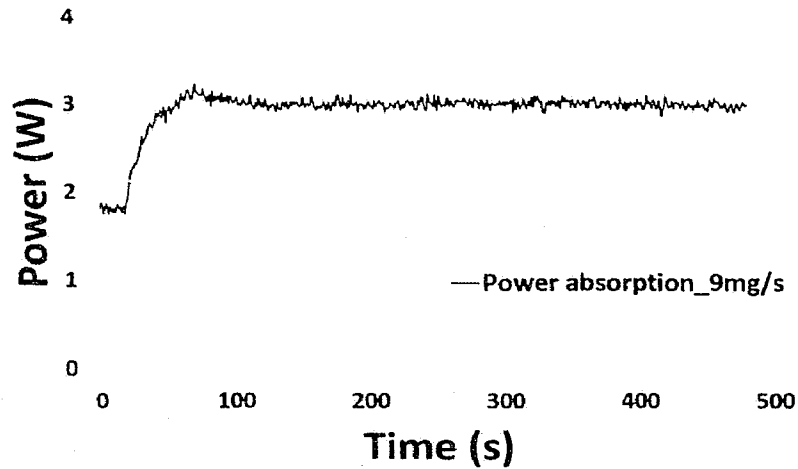
Figure 6.15: Power absorbed by the boiler with exhaust air and refrigerant flow rate of 0.92 $\frac{m}{s}$ and 9 $\frac{mg}{s}$.

Figure 6.14 shows the temperature profile at various location of the Boiler Test setup with the air velocity and working fluid flow rate set to V_{low} and 9 $\frac{mg}{s}$. The average temperature of the air at inlet and outlet of the copper heat exchanger casing were 123 °C and 115 °C, respectively. Initially, the average temperature at the bottom of the boiler was 104 °C; however, after the introduction of fluid into the boiler, the temperature gained its steady state at 93 °C. The average temperature of the vapor inside the steamdome was approximately 75 °C which is close to the working fluid boiling temperature of 76 °C . The discrepancy of 1 °C, is due to the error in temperature reading ($\pm$ 0.5 °C) and the location of TC inside the steamdome. With these considerations, it can be stated that the boiler was able to phase change the working fluid. The boiler consumed an average energy of approximately 3 watts from the Exhaust Heat Exchanger System (EHES) during the phase transformation of the refrigerant. Similarly, the tests were conducted with flow rates of 3 $\frac{mg}{s}$, 6 $\frac{mg}{s}$

and 13 $\frac{mg}{s}$. The results obtained from the tests are summarized in Table 6.2. The tests were repeated with exhaust air velocity at V_{high}. The results from the tests are summarized in Table 6.3.

Table 6.2: Average temperatures at various locations and power obtained while operating at V_{low}.

Refrigerant Flow rate ($\frac{mg}{s}$)	Air In (°C)	Air Out (°C)	Boiler Bottom (°C)	Vapor (°C)	Casing Walls (°C)	Ambient (°C)	Power Absorbed (watts)
3.0	122.7	115.0	94.8	75.8	70.0	21.5	2.63
6.0	122.0	114.5	92.6	75.2	70.0	21.5	2.95
9.0	122.0	115.0	92.8	75	71.0	21.5	3.0
13.0	122.7	114.7	92.6	74.8	71.0	21.5	2.97

Table 6.3: Average temperatures at various locations and power obtained while operating at V_{high}.

Refrigerant Flow rate ($\frac{mg}{s}$)	Air In (°C)	Air Out (°C)	Boiler Bottom (°C)	Vapor (°C)	Casing Walls (°C)	Ambient (°C)	Power Absorbed (watts)
3.0	124.6	118.7	97.7	75.7	71.6	21.5	2.7
6.0	124.3	118.3	94.2	75.2	71.9	21.5	3.2
9.0	125.4	119.4	94.6	75.0	72.0	21.5	3.4
13.0	124.9	118.9	94.3	74.9	72.9	21.5	3.3

A graphical comparison of the energy absorbed by the boiler for two different operating air velocities is presented in Figure 6.16. The plot demonstrates an interesting trend of boiler power absorption versus working fluid mass flow rate for two different operating air velocities. It can be visualized that the trends are similar for both the operating velocities. The energy absorption increased with the increase in working fluid supply rate from 3 $\frac{mg}{s}$ to 9 $\frac{mg}{s}$. The maximum power absorption was achieved at working fluid flow rate of 9 $\frac{mg}{s}$. The power absorption dropped as the working fluid

supply rate was increased to 13 $\frac{mg}{s}$. This is due to the over supply of the fluid than the boiler capability to draw the fluid and phase change it.
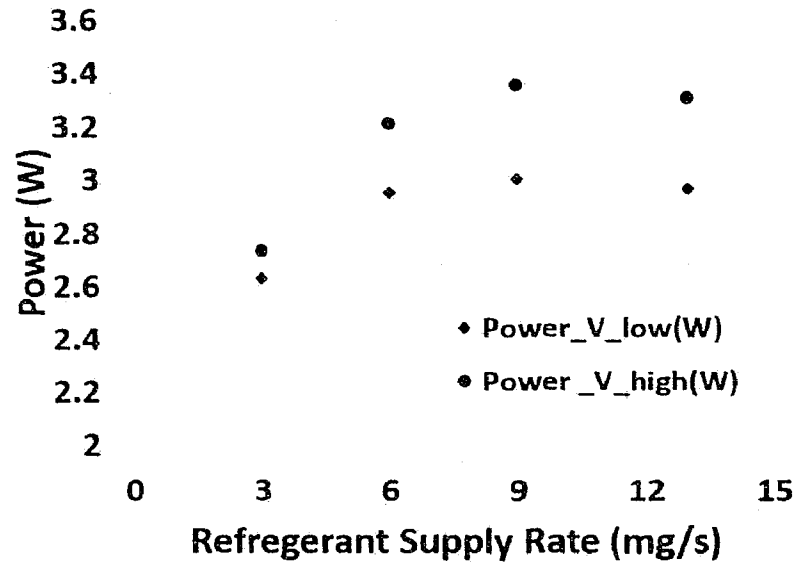
Figure 6.16: Comparison of energy absorbed by boiler at V_{low} and V_{high}.

This is due to the oversupply of the working fluid beyond the ability of capillary channels to draw fluid from the reservoirs to the heated surface of the boiler via a capillary action for phase transformation. In another word, the boiler was force fed resulting in pool boiling of the working fluid. The pool boiling hampered the heat and mass transfer capability of the boiler compared to the boiling achieved via the adequate supply of the working fluid ($9 \frac{mg}{s}$). The reason is the channels drew working fluid from the reservoirs via capillary action during the adequate supply ($9 \frac{mg}{s}$), allowing fluid to cover the channel walls sufficiently for maximum heat transfer. The fluid was evaporated and replenished via the capillary action at a similar rate, allowing the boiler to operate at its true operating condition. However, this was not the case with insufficient supply or oversupply. Furthermore, the force feed effect was

dominant when the working fluid was supplied with the flow rates above 13 $\frac{mg}{s}$. The boiler was unable to phase change the working fluid after a certain testing period resulting in accumulation of the fluid and flooding of channels with time. The results obtained from the tests are not included in the paper; however, it is brought up to justify the discussion further.

The energy balance was performed for each experiment to study the amount of energy captured by the Exhaust Heat Exchanger System (E_{EHES}), the energy absorbed by the boiler to phase change the working fluid (E_{boiler}), and the energy lost to the surrounding via convection (E_{loss}). The energy captured by the EHES was calculated using Equation 6.5 and Equation 6.4. The energy absorbed by the boiler was determined using the HFS sandwiched between the boiler and the EHES. The heat lost to the ambient from the test section was estimated to be E_{loss} from the difference between E_{EHES} and E_{boiler} using Equation 6.4. The energy values evaluated are summarized in Table 6.4.

Table 6.4: Energy calculation.

Air Velocity $(\frac{m}{s})$	Fluid flow rate $(\frac{mg}{s})$	E_{EHES} (W)	E_{boiler} (W)	E_{loss} (W)	Power Absorption (%)
0.92	3.0	4.9	2.63	2.3	53
0.92	6.0	5.0	2.95	2.1	58
0.92	9.0	5.0	3.0	2.0	60
0.92	13.0	5.0	2.97	2.0	59
1.20	3.0	5.0	2.7	2.3	54
1.20	6.0	5.1	3.2	1.9	62
1.20	9.0	5.1	3.4	1.7	66
1.20	13.0	5.1	3.3	1.8	64

The total energy absorbed by the boiler to phase change the working fluid was between 53% and 66% under the range of experimental conditions considered, depending upon air velocity and fluid supply rate.

6.3.2 Integrated boiler/Superheater Test

A detailed explanation of Integrated boiler/Superheater experimental setup is presented in Section 6.2.4.2. Unlike the Boiler Test, Superheater was included in this test. The boiler bottom temperature was maintained approximately at 104 °C with the air velocity fixed at V_{low}. This was achieved by raising the temperature of air flowing through the EHES. The averaged temperature of the air entering and leaving the EHES, the energy trapped by EHES evaluated using Equation 6.4 is summarized in Table 6.5.

Table 6.5: Temperature of the air entering and leaving EHES and the energy trapped by EHES.

Air In (°C)	Air Out (°C)	Power EHES (watts)
170.5	160.5	6.5

The boiler was initially heated for about 25 minutes and the working fluid was supplied to the boiler. The temperature readings of the air entering and leaving the EHES, boiler bottom, phase changed vapor inside the steamdome and steam at Superheater inlet and outlet were recorded. The readings from the HFS sensor sandwiched between boiler and Superheater was recorded as well. The phased changed vapor exiting the boiler was allowed to enter and leave the Superheater via connected tubing. The tests were conducted with a range of fluid supply rates and the effect of

fluid flow in boiler energy absorption and the vapor temperature at inlet and outlet of the Superheater were studied at atmospheric pressure.

The test began with the working fluid supply rate of 3 $\frac{mg}{s}$. The temperature and heat flux readings obtained from the test is presented in Figure 6.17 and Figure 6.18.
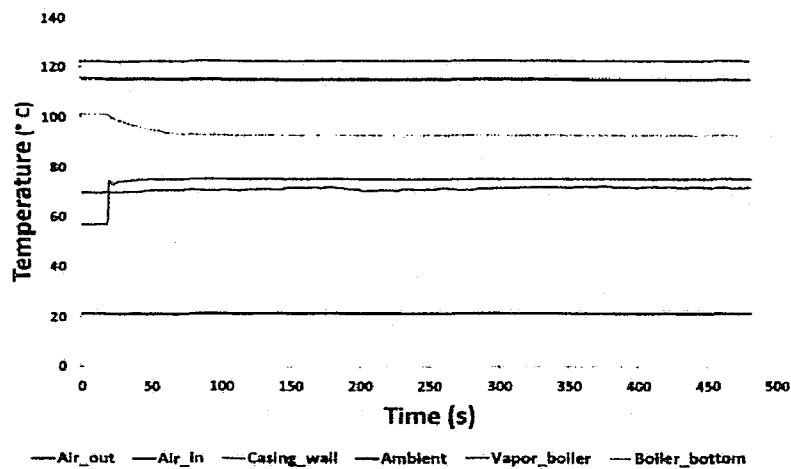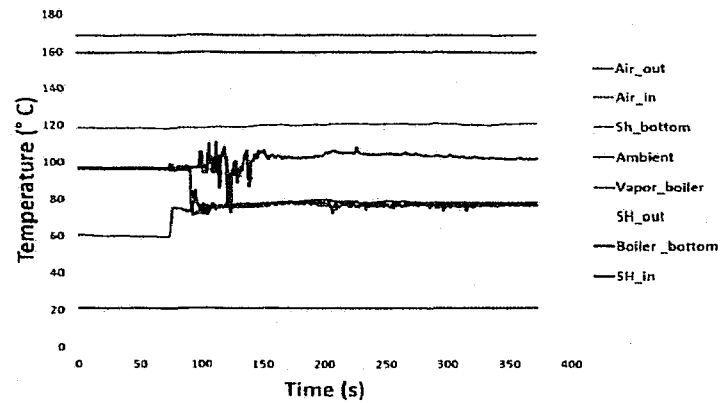

Figure 6.17: Temperature profile obtained at various location of the experimental setup with exhaust air velocity at V_{low} and refrigerant supply rate of 3 $\frac{mg}{s}$.
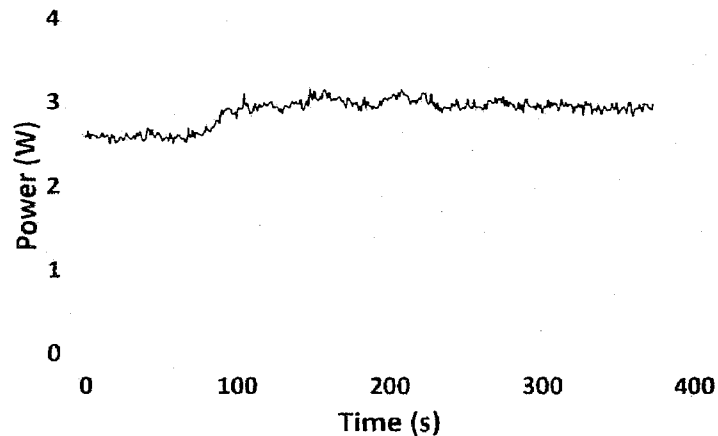
Figure 6.18: Power absorbed by the boiler with exhaust air velocity at V_{low} and refrigerant supply rate of 3 $\frac{mg}{s}$.

The temperature of the vapor exiting the boiler was approximately 78 °C. The temperature of the vapor entering and leaving the Superheater was 76 °C and 85 °C, respectively. The temperature reading at the exit of the Superheater indicated the refrigerant was superheated. The average energy absorbed by the boiler during phase transformation of the fluid was approximately 2.9 W. The test result demonstrated that the Integrated boiler/Superheater system sourced by a single heat supply was subsequently able to phase change and superheat the working fluid.

The test was then repeated by increasing the working fluid supply rate to 6 $\frac{mg}{s}$. The temperature and heat flux profiles obtained from the test are presented in Figure 6.19 and Figure 6.20, respectively.
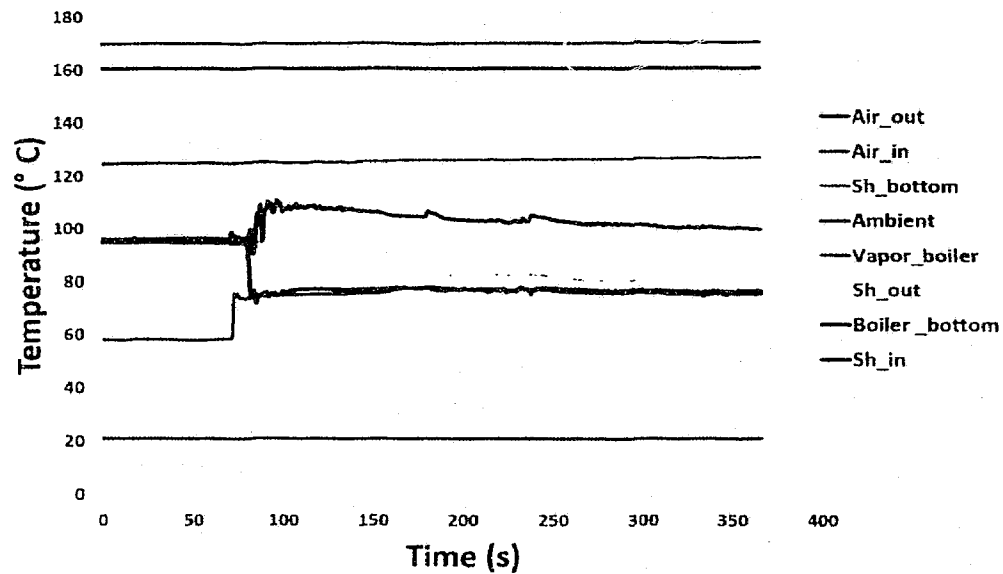
Figure 6.19: Temperature profile obtained at various location of the experimental setup with exhaust air velocity at V_{low} and refrigerant supply rate of 6 $\frac{mg}{s}$.
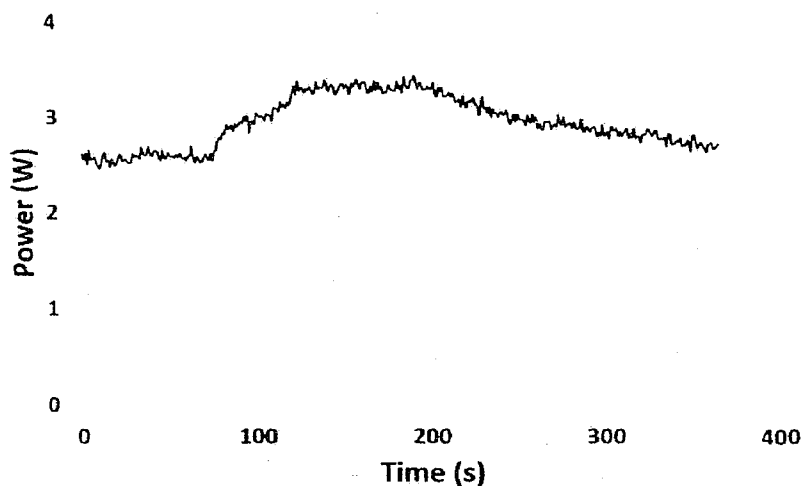
Figure 6.20: Power absorbed by the boiler with exhaust air velocity at V_{low} and refrigerant supply rate of 6 $\frac{mg}{s}$.

With the fluid flow rate of 6 $\frac{mg}{s}$, the energy absorbed by the boiler to phase change the working fluid attained a maximum value of about 3.2 W and then the value started to drop with time as the testing progressed (refer to Figure 6.20). The drop in the energy absorption was accompanied by the working fluid accumulation in the boiler. This was visually noticeable during testing. The experiment was interrupted after approximately 6 minutes to avoid any damage caused to the boiler due to continuous pumping of fluid by the infusion pump (refer to Figure 6.20). Despite the boiler bottom temperature (about 100 °C) well above the boiling temperature of HFE-7200 and the refrigerant flow rate below 9 $\frac{mg}{s}$, the boiler was unable to absorb energy to phase transform the fluid. The is due to the inclusion of additional flow resistance to the fluid exiting the boiler in the form of connecting tubing and the Superheater. Unlike the Boiler Test, the fluid exiting the boiler now has to traverse the tubing and the Superheater. Such inclusion resulted in a head loss (h_f) and failed to maintain

the required velocity head for the fluid to pass through the entire setup with ease. This resulted in the accumulation of fluid in the boiler with time.

However, this effect was not dominant in the test result obtained with the flow rate of 3 $\frac{mg}{s}$ (refer to Figure 6.18). The reason is the head loss increases with the increase in flow velocity and contrariwise for the head developed by a pump (h_p). Assuming difference in height (Z_2-Z_1) to be negligible due to micro size thickness of the Integrated boiler/Superheater System and the exit pressure (P_{out}) to be constant (at atmospheric), the pressure exerted by the boiler (P_{in}) and the (h_p) are the two components required to maintain velocity head. The higher the fluid supply rate, the higher is the h_f and the lower is the h_p. Therefore, the value for P_{in} has to be such that it takes account of increased h_f and decreased h_p to maintain velocity head. However, in this case, P_{in} is the result of the fluid flowing via capillary action in the channels. Thus, this restricts the higher supply rate to the boiler as a result of limitation on capillary action of the channels to phase change and pump fluid out of the boiler against the developed h_f.

With these insights into Exhaust Heat Recovery System (EHRS) characterization, further development on the Integrated boiler/Superheater setup has been planned. The future work includes maximizing the boiler's capability to pump working fluid out of the boiler via capillary action. This may be achieved by minimizing the head loss encountered during testing. The frictional losses could be minimized by reducing the tubing length that connects the boiler and the Superheater and also reducing the losses within the Superheater itself. Such modifications may improve the boiler capability to pump fluid with increased mass flowing out of the Superheater. In addition to this,

the future work will include characterizing the EHRS under pressurized conditions by partially restricting the Superheater outlet.

6.4 Conclusion

An experimental investigation of an Exhaust Heat Recovery System (EHRS) to scavenge a real-world waste heat discarded from exhaust heat pipe is demonstrated in this work. The EHRS consisted of Exhaust System (ES), Exhaust Heat Exchanger System (EHES), and Integrated boiler/Superheater System. Each component constituting EHES was designed and fabricated. The fabricated components were assembled to form EHES and testing was performed to characterize its heat scavenging capability under the range of experimental conditions considered, depending upon air velocity and the fluid supply rate.

The testing began with the determination of working temperature and air velocity without Superheater included in the test setup. The working temperature of approximately 104 °C was achieved via increasing the temperature of the air traversing EHES based on prior work. After the determination temperature, the working velocities of 0.92 $\frac{m}{s}$ and 1.2 $\frac{m}{s}$ were selected to study the effect of the air flow rate on the energy trapped by the EHES and the energy absorbed by the boiler to phase change the working fluid. For each air velocity, the boiler capability to absorb trapped heat from the EHES to phase transform the working fluid versus the refrigerant supply rate were studied. The tests were performed with fluid supply rates ranging 3 $\frac{mg}{s}$, 6 $\frac{mg}{s}$, 9 $\frac{mg}{s}$, and 13 $\frac{mg}{s}$. The test demonstrated the boiler was able to absorb maximum energy when the capillary flow rate achieved via capillary action of

the channels matched the fluid supply rate pumped into the boiler. In this case, the flow rate of 9 $\frac{mg}{s}$ demonstrated the maximum power absorption by the boiler.

The test was then performed with the Superheater included in the experimental setup. The working air velocity of 0.92 $\frac{m}{s}$ and the temperature of approximately 104 °C were utilized for the testing. For the fluid supply rate of 3 $\frac{mg}{s}$, the Integrated boiler/Superheater System was able to phase transform and superheat the working fluid. However, with the higher flow rate, the boiler was unable to phase change and pump fluid out of it as testing progressed. This highlighted the limitation on capillary channels' ability to phase change and pump fluid against developed head losses during increased fluid supply rate.

The future work includes maximizing boiler capability to pump working fluid out of the boiler via capillary action. This may be achieved by minimizing the head loss encountered during testing. The frictional losses could be minimized by reducing the tubing length that connects the boiler and the Superheater and also reducing the losses within the Superheater itself. Such modifications may improve the boiler capability to pump fluid with increased mass flowing out of the Superheater. In addition to this, the future work will include characterizing the EHRS under pressurized conditions by partially restricting the Superheater outlet.

CHAPTER 7

A REVIEW OF VARIOUS TES TECHNIQUES

Thermal energy storage (TES) is a technique to store thermal energy in the form of hot or cold substances and subsequently utilizing the stored energy as a thermal source [79]. This technique is well established in the large scale like in a solar power plant where the excess heat and/or the harvested heat itself is stored temporarily in a thermal storage device. The TES process is then reversed allowing stored heat to be made available to a boiler at the periods of higher energy demand. The steam produced in a boiler is supplied to the generator to produce mechanical or electrical work [9].

The TES can operate synergistically as a repository for excess thermal energy at the periods of minimal energy demand and as a thermal source making it available at the periods when needed. Moreover, it balances the supply and demand of energy [80, 81]. This makes TES a significant technique for utilizing energy resources more efficiently. Such notion of storing heat and utilizing it to produce power can be implied on a small scale as well. The excess heat from the thermodynamically limited process can be stored and later supplied to the small scale thermal energy recovery system as discussed in Section 1.1. In addition to this, it can also be utilized as a medium for reducing the energy consumption in the buildings for indoor thermal comforts [79].

7.1 Types of Thermal Energy Storage

The thermal energy storage technique is categorized as thermal and chemical [79]. Thermal energy is stored in a substance as a result of a change in internal energy (ΔU). The change in internal energy is due to the sensible heat, latent heat and thermochemical or a combination of these.

7.1.1 Sensible Heat Storage

Sensible heat storage is a technique to store thermal energy by increasing the temperature of solid or liquid without undergoing a phase change. The amount of heat stored or released depends on the material specific heat (c_p), temperature change (ΔT) and mass (m). The mathematical expression for the sensible heat storage (Q_{SHS}) is represented by Equation 7.1 [82]. For the operating temperature range below 100 °C, water is preferred as a sensible heat storage medium due to its high specific heat capacity, inexpensiveness, and availability. However, materials like molten salts, oils, and liquid metals are utilized for the temperature range above 100 °C [79].

$$Q_{SHS} = \int_{T_i}^{T_f} mc_p \Delta T.$$

(7.1)

7.1.2 Thermochemical Storage

In thermochemical heat storage (Q_{TC}), the chemical bond of the storage medium undergoes bond formation (endothermic) and bond breaking (endothermic) to absorb or release thermal energy in a reversible chemical reaction. The amount of heat stored depends on the storage material endothermic heat of reaction (ΔH_r), mass (m) and the extent of conversion (a_r) [82]. Some of the preferred thermochemical

storage materials are lead acid, nickle cadmium, iron ion and tin oxide/tin-ammonia. The chemical storage technique demonstrates higher energy density; however, the cost of developing the storage system is an expensive alternative [83]:

$$Q_{TC} = a_r m \Delta H_r.$$ (7.2)

7.1.3 Latent Heat Storage

Latent heat storage is a technique of storing thermal energy at nearly constant temperature during phase change of the storage material (usually melting). The amount of heat stored by the phase change material (Q_{LHS}) is mathematically represented by Equation 7.3 [82]. The latent heat storage is categorized into four sub groups based on the types of phase transformation:

- Solid-Solid

- Liquid-Vapor

- Solid-Vapor

- Solid-Liquid.

$$Q_{LHS} = \int_{T_i}^{T_m} mc_p \Delta T + a_r m \Delta H_r + \int_{T_m}^{T_f} mc_p \Delta T,$$ (7.3)

where m is the mass, c_p is the specific heat, a_r is the fraction melted, ΔH_f is the latent heat of fusion, T_i is the initial temperature, T_m melting temperature, and T_f is the final temperature. In Solid-Solid phase change, the heat is stored via the change in a crystalline structure of the material. The Solid-Solid storage system is comparatively easy to design as the phase transformation does not experience large volume expansion alike in the case of Solid-Vapor or Liquid-Vapor [84]. However, it suffers from a low

latent heat of fusion. Some of the preferred Solid-Solid phase transition materials are pentagycerine, potassium difluoride, Lithium sulfate and pentaerythritol [79].

Among all phase transition categories, the Solid-Liquid phase transition is more efficient and economically attractive thermal energy storage technique. The Solid-Liquid phase transformation materials involve small volume change of approximately 10% or fewer [79]. This makes the storage system design simple and practical. Moreover, the material possesses reasonable latent heat of fusion and the temperature of the storage material remains constant during the phase change avoiding to deal with complex high-temperature system design.

The commercially available phase change materials (PCM) are classified into organic, inorganic and eutectic. Based on properties such as thermal, physical, kinetic, chemical and economics, a material is selected for the particular application. However, there is not a single material that satisfies all the stated material properties [79].

CHAPTER 8

THERMAL ENERGY STORAGE WITH PHASE CHANGE MATERIAL[†]

8.1 Introduction

The predicted growth of world energy consumption is driving the need for efficient, sustainable technologies applied across a wide variety of systems. The United States Department of Energy (DoE) has indicated that within the U.S. alone, energy consumption will increase from 98 quadrillion BTUs (British Thermal Units) to 108 by 2040. Worldwide consumption is projected to increase 47% by 2035 compared to 2010 [85]. The residential sector consumed 22% of the total U.S. energy in 2011 [86]. Building thermal control is a significant source of this consumption: more than 50% of all energy consumed is related to heating and cooling [87].

There has been a trend of increasing interest and research on building infrastructure energy enhancements for the past several decades. In general, homes that were constructed between 2000 and 2005 use about 14% less energy per square foot than those built in the 1980s. These same homes use 40% less energy per square foot

[†]A part of this material has been published as Suvhashis, T., Yafie, Z., Yuri, and L. Leland, W., "HALLOYSITE CLAY NANOTUBES WITH PCM FOR THERMAL ENERGY STORAGE AND EFFICIENCY," in Proceedings of the ASME 2013 International Mechanical Engineering Congress and Exposition, 2012, pp. V06BT07A068 and is being reproduced with the kind permission of the publisher (ASME) and co-authors. The remaining part has been published as Yafei, Z., Suvhashis, T., Leland, W., Yuri, L., "PHASE CHANGE HEAT INSULATION BASED ON WAX-CLAY NANOTUBE COMPOSITE," Advance Engineering Materials, vol. 16, no. 11, pp. 1391-1399, 2014 and the figures and tables from the latter have been reproduced and referenced.

than structures built before 1950 [87]. There have been multiple recent approaches to increased building thermal energy efficiency. Notable advancements include thermal insulation technologies that now consider life-cycle analyses [88]. In addition, there has also been extensive investment in thermal energy storage (TES) research. This work considers a new material consisting of traditional waxes combined with clay halloysite nanotubes (HNTs) for use in these types of installations.

TES is already a significant component of large scale systems like solar power plants operating on the MegaWatt scale. The phase change materials utilized are typically salts, well suited for the high temperatures of operation [89, 90]. By comparison, TES applied to buildings must operate at lower temperature, and it represents an increasing area of interest and application [91, 92, 93]. In building applications, a suitable phase change material is selected to sit within the structure and capture incoming thermal energy before it affects living environments. Following thermal absorption, the energy is passively rejected back to the surrounding environment when external temperatures have decreased. These phase change materials have been successfully integrated with typical building products like gypsum board and even concrete [94]. TES has been successful at shifting peak building a thermal loading and reducing total energy consumption [95]. Peippo *et al.* noted potential savings on the order of 15% annual energy costs via TES as applied to a residence in Wisconsin [96]. Additional studies by Muruganantham *et al.* indicated that the use of PCM in an Arizona application shifted peak thermal loads up to an hour and reduced the energy costs associated with air conditioning by 29% [97].

Many current TES solutions have relied on phase change material (PCM) like waxes or oils applied to interior structure walls. The melting temperatures approximate the desired interior temperatures maintained by the HVAC systems [98]. Of particular note are micro-encapsulation techniques that hold the PCM within small-scale capsules or enclosures for application [98, 99, 100]. This maintains liquid-phase PCM within a small and thermally conductive micro enclosure and prevents movement of the PCM when in liquid form. This represents a common challenge to these TES techniques in general: the ability of the material to maintain shape when undergoing a phase change. While microencapsulation addresses this issue, this can significantly increase the cost per energy savings [98]. Alternatives to microencapsulation include microencapsulation where large quantities of PCM are held in larger volumes. This contains the liquid-phase PCM in pre-formed shapes. This is a particular challenge to building retrofitting. An additional challenge associated with TES is the low thermal conductivity of the waxes or oils employed. The typical thermal conductivity of paraffin, for example, is on the order of 0.5 $\frac{W}{mK}$. Values as low as 0.15 $\frac{W}{mK}$ have been noted for specific paraffin based TES consideration [97]. Low conductivity diminishes the ability of the substance to absorb and reject thermal energy within the periods of greatest thermal loading.

This study focusses on new TES materials that are designed to integrate with new or existing structures to increase the operating efficiency of the building itself. In this manner, significant progress is possible in this field of growing energy consumption and projected worldwide use. The material presented is a modified Phase Change Material (PCM) based on paraffin that undergoes a phase change when heated. The

material may be placed in the wall or roof structures where external thermal loading is the greatest. The material is unique and represents a combination of the base PCM (paraffin) as well as varying concentrations of additives. These include naturally occurring halloysite clay nanotubes (HNT) designed to integrate with the wax and maintain material structure during phase change. The use of HNT maintains a skeletal structure during repeated phase change cycles and can eliminate the need for formal encapsulation techniques.

This study also examines the specific use of thermal conductivity enhancements designed to improve the rate of thermal energy absorption within the material layer. These enhancements take the form of carbon-based nanotubes (CNT) or nanoparticles. Because the form is maintained when undergoing a phase change, it is possible to retain the distribution of thermal enhancement within the material given successive cycling. This has proven problematic in prior work and represents another significant benefit to the use of HNT. HNTs also represent a naturally occurring material, available at low cost in great abundance. These issues are increasingly important when considering a full life-cycle analysis of the new material in building applications. Specific tests that characterize the new PCM based on varying amounts of HNT, as well as thermal conductivity enhancement in a small scale laboratory setup, are presented in following sections.

8.2 Experimental Materials and Method

8.2.1 Materials

8.2.1.1 Paraffin Wax

Paraffin wax is a saturated hydrocarbon. The properties of wax utilized in this work are summarized in Table 8.1 [101, 102]. Figure 8.1 shows an image of a baseline wax.

Table 8.1: Baseline paraffin PCM properties.

Property	Solid	Liquid
Density $\left(\frac{kg}{m^3}\right)$	830	913
Thermal Conductivity $\left(\frac{W}{mK}\right)$	0.25-0.5	0.80
Specific Heat $\left(\frac{J}{kgK}\right)$	2981	2604
Heat of Fusion $\left(\frac{J}{g}\right)$	200	200
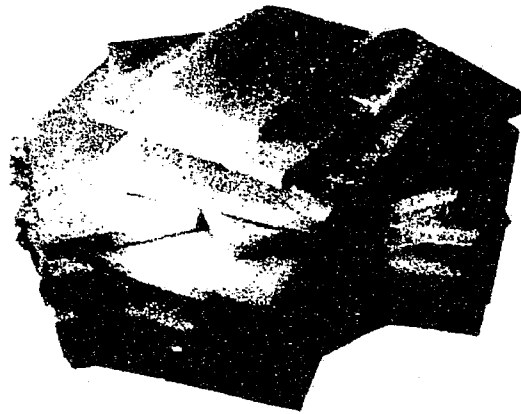
Figure 8.1: An image of a baseline wax.

8.2.1.2 Halloysite

The halloysite clay nanotubes (HNT) are hollow, naturally occurring nanotube structures that are available in great abundance at low cost. Figure 8.2 shows an image

of a halloysite nanotube [103]. Compared to CNT, prices for halloysite are approximately 150 times less expensive. Specifically, halloysite $(Al_2Si_2O_5(OH)_4 \; x \; nH_2O)$ is a two-layered (1:1) tubule aluminosilicate. When n $=$ 2, the diameter is 10 $\overset{\circ}{A}$ with one layer of water between wall layers. When n $=$ 1, the diameter is 7 $\overset{\circ}{A}$, resulting from heating of the material to 110-120 $°C$. Specific surface area of the halloysite is 105 $\frac{m^2}{g}$ and specific gravity is 2.53 $\frac{g}{cm^3}$. Dried HNT is specifically used in this work. The properties of HNT used in this work are summarized in Table 8.2 [101].

Table 8.2: Halloysite clay properties.

Property	Value
Diameter (nm)	30-70
Length (μm)	1-3
Thermal Conductivity $(\frac{W}{mK})$	0.1
Surface Area $(\frac{m^2}{g})$	64

Figure 8.2: An image of a halloysite.

8.2.2 TES Composite Preparation

Mixtures of these CNT, GNP, HNT, and base paraffin were assembled with varying concentrations by mass. Table 8.3 details the specific composite materials and specific composition [103]. In general, PCM was fabricated and tested with mixtures of wax, conductivity enhancement, and HNT that ranged from 100% paraffin wax to mixtures of 50:50 Wax:HNT by mass and 20:30:50 CNT:HNT:Wax by mass.

Table 8.3: PCM mixtures studied by % mass.

Mixture	GNP %	CNT %	HNT %	Wax %
A	0	0	0	100
B	0	0	100	0
C	0	3	10	87
D	0	0	50	50
E	0	0	10	90
F	0	5	10	85
G	6.1	0	0	93.9
H	5	5	45	45
I	0	10	45	45
J	0	20	30	50
K	10	0	45	45

All composites were generated by melting the paraffin in a beaker on a hotplate. The desired quantity of additives and isooctane solution were added to the melted wax. The mixture was stirred and refluxed under 80 °C for 3 hours. Then the mixture was vacuum dried overnight. This readied the various composites for testing and full evaluation.

8.2.3 Morphological Characterization of PCM Composites

The morphological study was performed on the fabricated composite (refer to Table 8.3). This study will allow the structural analysis of the distribution of different materials composing the sample. The study was performed utilizing Hitachi

S-4800 field emission scanning electron microscopy (FE-SEM) located at Louisiana Tech University. The FE-SEM was operated at secondary electron imaging mode with an input voltage of 1-3 kV. Nitrogen adsorption-desorption isotherms were recorded with NOVA 2200, Quanto Chrome Instruments at 77 K for the specific surface area estimations with the BET (Brunauer Emmett Teller) technique [103].

8.2.4 Test Setup

8.2.4.1 Thermal Conductivity

Composites were tested in a small-scale acrylic chamber as depicted in Figure 8.3. The chamber was fabricated from 5.75 mm thick material with dimensions of 35 by 30 by 15 mm. Three sides were permanently affixed to a bottom acrylic piece. The fourth side was constructed to allow removal during thermal application to the PCM materials. This side was held in place by four small bolts and sealed via gasket material. During testing, removal of this side allowed investigation of the material's ability to maintain shape during the phase change. A top piece was constructed and was held in place by through bolts to allow access to the inner volume where the PCM was placed. K-type thermocouples (TC) were utilized to measure a temperature of the PCM at discrete points through the material's thickness. Locations were at the top of the chamber as well as 5, 10, and 15 mm from the top. Each TC was inserted through one chamber sidewall and epoxied in place.
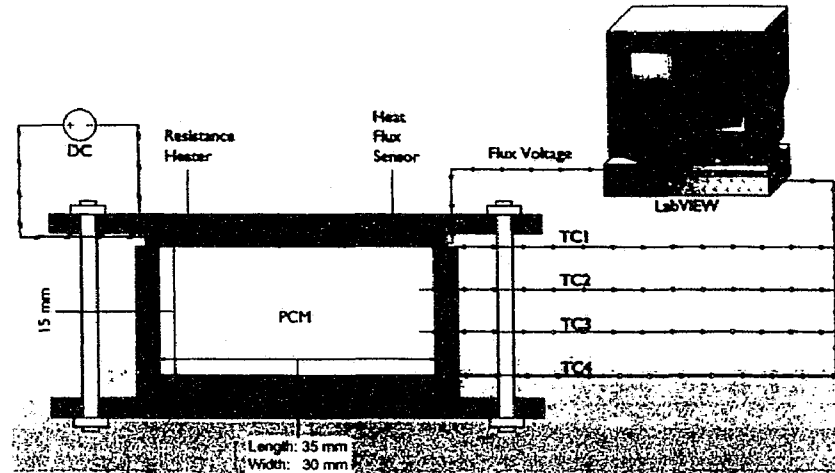
Figure 8.3: Setup of PCM test device.

Heat flux to the test device was accomplished through the use of a resistance heater. The heater simulated external thermal loading from a real-world energy source. The heater was connected to a power supply where voltage and current were measured; 5.7 W was maintained for each test independent of PCM under investigation. To fully quantify the thermal energy transfer to PCM, an Omega HFS-3 thin film heat flux sensor was placed between the resistance heater and the PCM. This, in combination with the thermocouple readings, helped establish critical PCM performance characteristics that included average thermal conductivity of the various composites.

This setup was maintained for all tests independent of PCM composition. This allowed for accurate and easy comparison between materials. Loading of the test setup was accomplished by melting the PCM and filling the inner test volume manually. Care was taken to ensure that no gaps or other anomalies were present after filling. The use of acrylic in the construction of the test device allowed for this visual inspection.

Following the filling of the test volume, the top was added to the device and the PCM was ready for evaluation.

Tests were conducted to characterize thermal conductivity as well as shape stability of the PCM materials noted in Table 8.3. A consistent 5.7 W was supplied to the resistance heater to simulate real-world thermal loading. Each test was conducted multiple times to ensure accurate readings and characterization. For each run, thermal energy was applied for several hours to attain a fully steady-state equilibrium point for each construction. After attaining a steady state, measurements from the TCs and heat flux sensor were used to quantify the operating characteristics of the various materials.

Ambient temperature around the setup was maintained at approximately 25 °C. Data was recorded and analyzed via LabView setup on a connected PC. The four k-type thermocouples provided temperature data which was used to determine the average thermal conductivity k of each mixture tested. Equation 8.1 provided the basis for this calculation where q was the heat transfer from the resistance heater (measured via heat flux sensor), A was the area of heat transfer, ΔT was the temperature gradient between TC readings, and Δz was the vertical distance between TC.

$$k = \frac{q/A}{\Delta T/\Delta z}.$$
(8.1)

8.2.4.2 Shape Preservation

In addition to measurement of thermal conductivity, tests were also conducted to establish the ability of the various PCM mixtures to maintain shape during phase change. The addition of the HNT to the base paraffin mixture enabled this unique

behavior. Upon reaching steady state, one side of the panel of the test device was removed as shown in Figure 8.4. A camera was used to photograph the material at this operating condition. Material that maintained shape easily held to the original form established by the fully enclosed test device. Because the temperature was simultaneously recorded by TC, each test was conducted only at temperatures above the melting point of the paraffin wax. This, in combination with the thermal conductivity measurements, allowed characterization of these unique materials as described in the Results section.
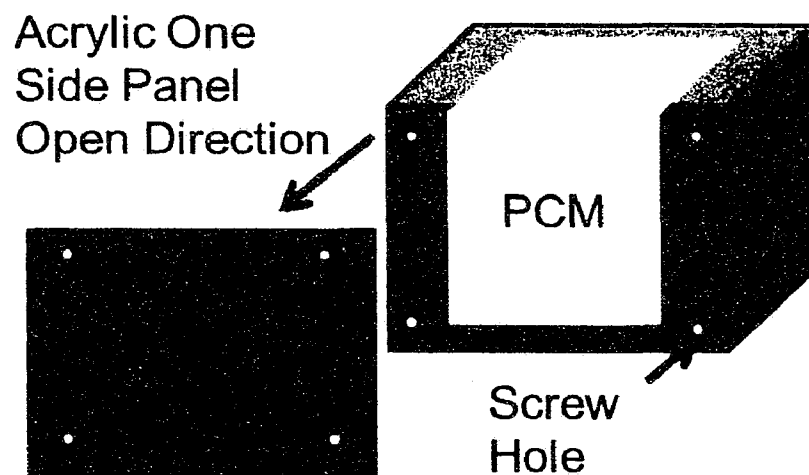
Figure 8.4: Acrylic PCM housing.

8.2.5 Thermal Characterization

In addition to the thermal conductivity and shape stabilization study as explained in Section 6.2.4, thermal analysis of PCM composites was performed. This included transition point (T_t), melting point (T_m), and latent heat (Δh) evaluation of the sample. The study was done using a differential scanning calorimetric instrument

(Diamond DSC, Perkin-Elmer) located at Louisiana Tech University. The DSC measurements were performed in a temperature range of 20-80 °C with a heating rate of 2 °C per minute.

8.3 Results and Discussion

8.3.1 Morphological Characterization of PCM Composites

The TES composites were fabricated with varying mass of wax, HNT, CNT and GNP (graphite nano powder) as listed in Table 8.3. The morphological characterization was performed on the TES samples. The SEM images of the composites are shown in Figure 8.5. The cylindrical shape of HNT with hollow open-ended lumen can be visualized in Figure 8.5 (a) and (b) [103]. The length and diameter of the cylinder were in the range of 0.5-1.5 μm and 50-70 nm, respectively.
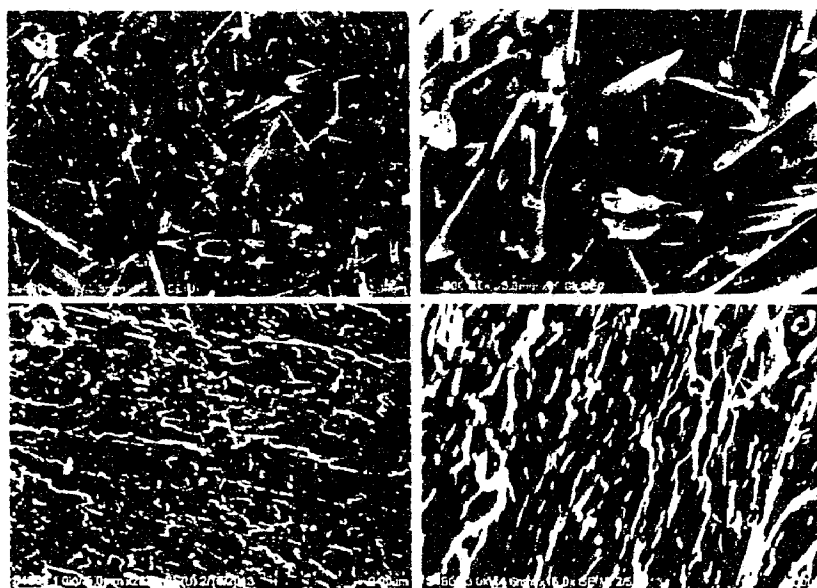
Figure 8.5: SEM images of halloysite (a, b), wax/HNT mix (50/50%) (c), and wax/HNT/GNP mix (45/45/10%) (d).

The SEM image of wax/HNT composite with an equal ratio by mass percentage is shown in Figure 8.5 (c). The cylindrical halloysites shown in Figure 8.5 (a) are well dispersed and coated with wax. The conglutination of halloysite by wax can be visualized in the image. Figure 8.5 (d) shows the image of wax/halloysite/graphite (45/45/10%). The inclusion of third component graphite to enhance the thermal conductivity of the composite seems to favor the conglutination of wax/HNT. The addition of graphite has increased the interfacial adhesion between wax and halloysite. This is evident in Figure 8.5 (d). The embedded halloysite and the conglutination of halloysite by wax are clearly visible. Moreover, the incorporation of graphite into the wax/halloysite composite resulted in a finer dispersion of the particle.

This may not have been achieved with simply wax and graphite mixture due to higher density of graphite ($\approx 2260 \ \frac{Kg}{m^3}$) than liquid wax ($\approx 913 \ \frac{Kg}{m^3}$) [101, 102, 103]. The graphite particles would have settled at the bottom of the wax resulting in higher conductivity at the bottom and lower conductivity at the top of the composite. This settling effect due to density difference has been minimized by the addition of halloysite to the wax. Further study of the shape preservation due to conglutination of halloysite by wax is presented in following sections.

8.3.2 Thermal Conductivity

PCM for the tests was fabricated with varying mixtures of wax, HNT and conductivity enhancement materials such as CNT or GNP by mass as noted in Table 8.3. Fabricated PCM was loaded carefully into the acrylic housing (refer to Figure 8.4). Tests were performed to investigate shape preservation characteristics and thermal

conductivity of prepared PCM mixtures during phase change. Figure 8.6 demonstrates a typical temperature profile of PCM at the four TC locations during thermal loading. The curves in Figure 8.6 show the increasing temperatures of the PCM that result in steady state profiles as the test continues. During the phase change, the PCM stores latent heat at constant temperature across PCM. This results in the "saddle" profile of constant temperature before a final steady state is achieved. Independent of PCM mixture, this saddle point occurs at approximately 54 °C for all tests. This is consistent with the expected paraffin melting point of 56 °C. The saddle temperature profile is because of an endothermic process associated with a change in phase of the wax from solid to liquid. Approximately after one and a half hours (90 min) the curves attained a steady state.
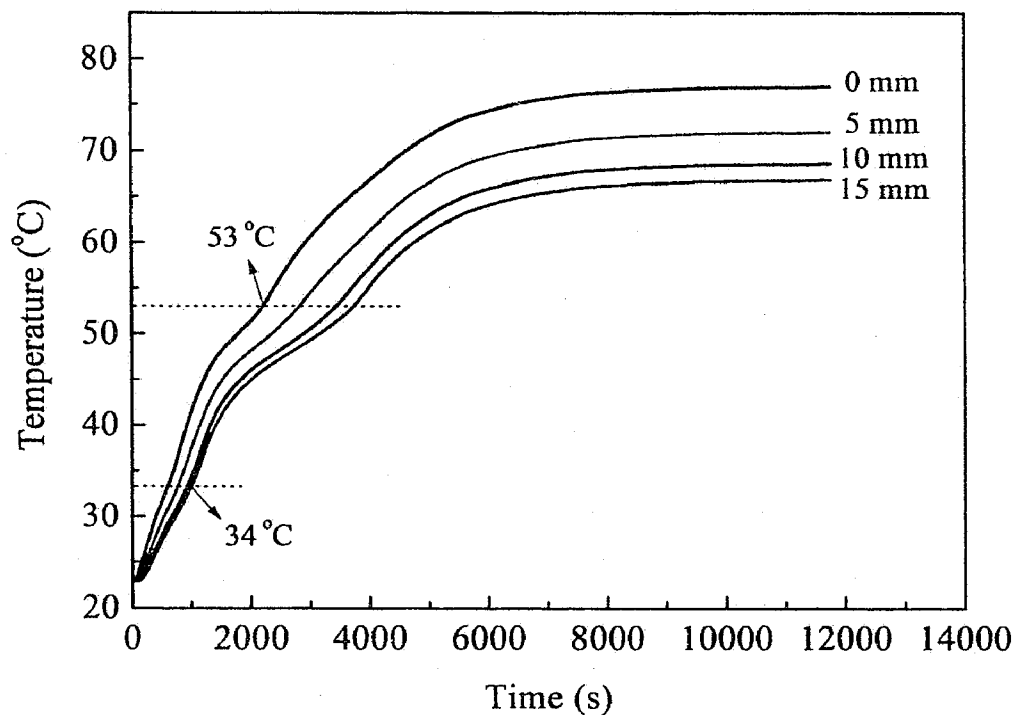
Figure 8.6: Typical temperature profile of PCM during thermal loading.

The overall temperature gradient across the 15 mm height was evaluated from the thermocouple data and combined with the heat flux data using Equation 8.1. Thermal conductivity was calculated for each sample tested. Individual PCM mixture with varying additive concentration (conductivity enhancement and HNT) by mass were designated as A through K. Table 8.4 summarizes these average thermal conductivities for the various PCM mixtures in the same order as shown in Table 8.3. The error associated with ΔT, heat flux and ΔZ were determined [38]. These were on the order of $\pm$ 0.5 °C, $\pm$ 0.19 $\frac{W}{m^2}$ and $\pm$ 0.1 mm respectively. The error associated with each individual thermal conductivity was determined to be on the order of $\pm$ 0.1 $\frac{W}{mK}$.

Several tests were performed on the PCM mixtures to investigate enhanced thermal conductivity as well as a phenomenon to preserve original shape during phase change. First, conductivity enhancements were applied to the base wax, and second, HNT was added to characterize shape preservation. Thermal conductivity enhancement materials utilized were CNT and GNP, which were added to the wax. With 6.1% of GNP and 5% of CNT additive by mass, the PCM illustrated an increased thermal conductivity of about 0.56 and 0.49 $\frac{W}{mK}$, respectively. However, the thermal conductivity of PCM mixtures was not stable due to the settling of conductivity enhancement materials at the bottom after several heating and cooling cycles. Full results are noted in Table 8.4.

Table 8.4: Thermal conductivity of PCM mixtures studied by % mass.

Mixture	$k \frac{W}{mK}$	GNP(%)	CNT (%)	HNT (%)	Wax (%)
A	0.25	0	0	0	100
B	0.1	0	0	100	0
C	0.39	0	3	10	87
D	0.34	0	0	50	50
E	0.26	0	0	10	90
F	0.48	0	5	10	85
G	0.56	6.1	0	0	93.9
H	0.83	5	5	45	45
I	0.83	0	10	45	45
J	0.84	0	20	30	50
K	1.35	10	0	45	45

8.3.3 Shape Preservation

Second, tests were performed on PCM mixtures to investigate original shape preservation. PCM with an equal amount of wax and HNT was tested. Figure 8.7 demonstrates this PCM mixture was able to preserve its shape given a maximum temperature of 81 °C. This was considerably higher than the melting point of the base wax (56 °C). However, an addition of HNT resulted in a decrease of overall PCM thermal conductivity. HNT is clay and has a thermal conductivity of about 0.1 $\frac{W}{mK}$, which is less than the thermal conductivity of wax. This expected decline in thermal conductivity fell within the experimental error of the thermal conductivity calculation. Despite this, the importance of thermal conductivity enhancement was highlighted and mixtures were fabricated that included both HNT, thermal enhancement, and the base paraffin. To accomplish this, investigations centered on the minimum amount of HNT required for full shape preservation and conductivity enhancement.
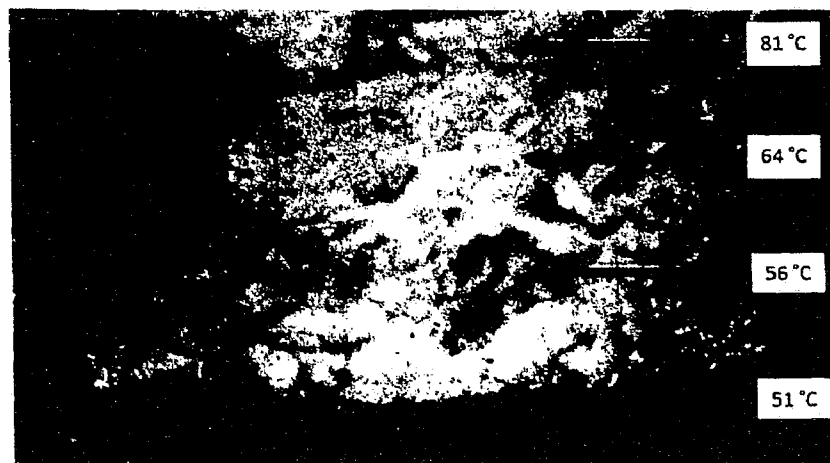
Figure 8.7: Original shape preservation by 50% of HNT and 50% of wax PCM mixture.

Through variation of the enhancement concentration and HNT, a range of values was achieved from 0.39 to 1.35 $\frac{W}{mK}$ among the various PCM materials as enhancements and HNT ranged from 3 to 20% and 10 to 45% by mass, respectively. Specific results indicated a maximum thermal conductivity was achieved of 1.35 $\frac{W}{mK}$ using a mix of 10:45:45 GNP:HNT:wax by mass. The results demonstrated that PCM mixture with HNT concentration above 30% by mass was able to retain its original shape at temperatures above the wax melting point. Figure 8.8 shows PCM mixtures with 10% and 30% of HNT by mass.
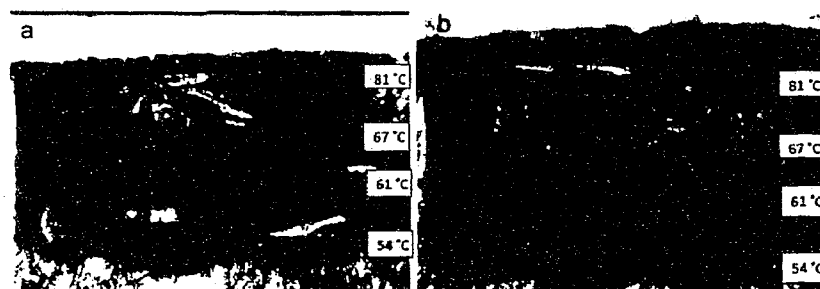
Figure 8.8: PCM mixture 10% of HNT (a) and PCM with 30% of HNT (b).

The introduction of HNT to PCM mixtures also illustrated stability in thermal conduction even after numerous heating and cooling cycles. This is shown in Table 8.5. This signaled that, unlike other approaches, the material did not allow settling of the enhancements upon multiple thermal cycling.

Table 8.5: Thermal conductivity of PCM mixture K for multiple thermal cycles.

PCM Mixture	Run 1	Run 2	Run 3	Run 4
K	1.33	1.37	1.35	1.36

8.3.4 Thermal Characterization

Differential Scanning Calorimetry (DSC) tests were performed on the pure wax and wax composites to study thermal properties such as transition temperature (T_t), melting temperature (T_m) and latent heat (ΔH). Figure 8.9 shows the DSC generated temperature versus heat flow profiles of pure wax and wax composites [103]. The DSC curve of pure wax illustrated in Figure 8.9 (a) served as a baseline for subsequent thermal characterization of wax based composites. The sharp principle peak and the minor peak generated by the DSC represents a solid-to-liquid transition and a solid-to-sold transition of the pure wax Figure 8.9 (a). The principle peak accounts for approximately 75% of the total latent heat. It is visible from the plot that the phase change transition of pure wax is initiated at approximately 47 °C and it melted at approximately 52.3 °C. The melting temperature of 52.3 °C is in close proximity with the supplier provided melting point of 52 °C and the typical temperature plot provided in Section 6.3.2 (refer to Figure 8.6). In addition, the latent heat is approximately 171 $\frac{J}{g}$ [103].
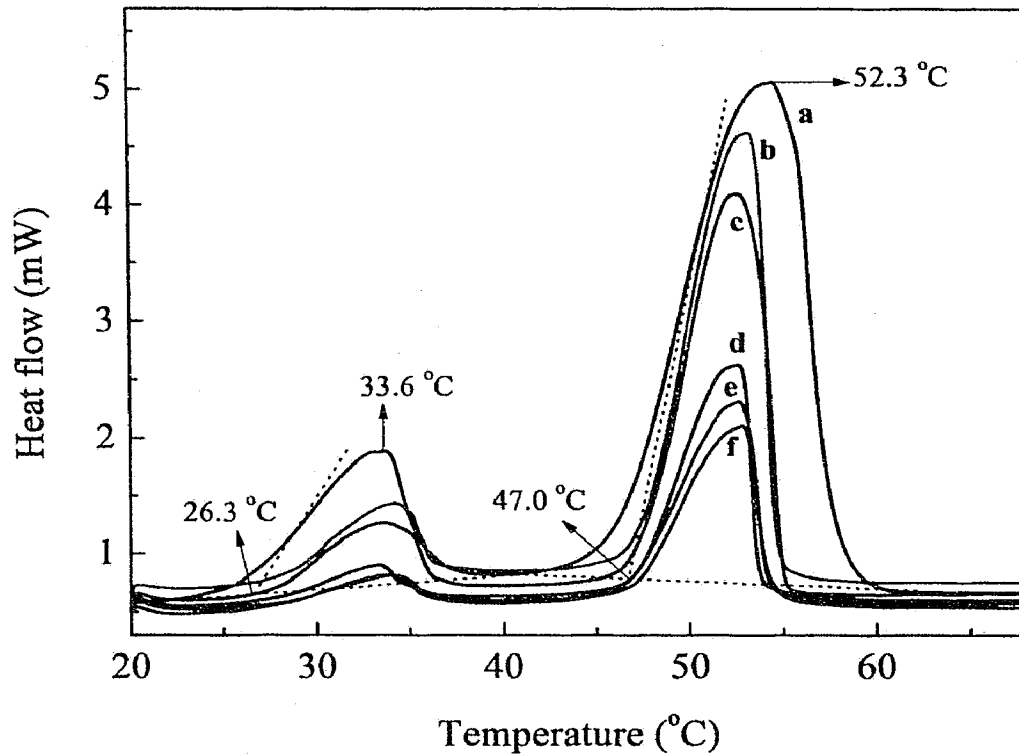
Figure 8.9: DSC thermal profile of pure wax (a), wax/HNT (50/50%) (b), wax/HNT/CNT (45/45/10%) (c), wax/HNT/GNP (45/45/10%) (d), wax/HNT/GNP/CNT (45/45/5/5%) (e), and wax/HNT/CNT (87/10/3%) (f).

After this initial study of pure wax, DSC curves were generated for various wax based shape stabilized composites to investigate the effect of additives such as halloysite, graphite and carbon nanotubes on the thermal properties of baseline wax. The DSC curves for the wax based composites demonstrated a similar trend of spikes. The solid-to-liquid and the solid-to-solid transition peaks are clearly visible. This indicates that despite the dispersion of additives throughout the wax, the wax is able to undergo phase transformation. The transition temperature and the melting temperature of the shape stabilized composites are in close agreement with the pure wax peaks within a standard deviation of $\pm$ 1 °C. However, an area under the peak is

comparatively smaller for the shape stabilized composites with reduced wax content. The evaluated thermal properties from these DSC characterizations are summarized and compared with the theoretical latent heated calculated using Equation 8.2 in Table 8.6:

$$\Delta H_{composite} = \omega \Delta H_{wax} \tag{8.2}$$

where $\Delta H_{composite}$, ω and ΔH_{wax} are the evaluated latent heat of the shape stabilized PCM, a mass ratio of wax in the composite and latent heat of pure wax, respectively. The measured latent heat is in close agreement with the calculated theoretical values, yielding a difference less than 14% [103].

Table 8.6: Thermal properties of pure wax and shape stabilized PCM composites where HNT is halloysite, CNT and GNP are carbon nanotubes and graphite particles.

Composite Wax:HNT: GNP:CNT w(%)	T_t (°C)	T_m (°C)	Melting Properties		
			Total ΔH ($\frac{J}{g}$)	Calc ΔH ($\frac{J}{g}$)	Difference (%)
100:0:0:0	47.0	52.3	171.0	–	–
50:50:0:0	46.8	53.5	87.1	85.5	-1.9
45:45:10:0	47.1	52.9	68.4	76.9	11
45:45:5:5	46.8	52.7	88.1	76.9	-14
87:10:0:3	47.4	52.7	145.7	148.7	2.1
45:45:0:10	47.1	52.7	75.7	76.9	1.6

After this thermal characterization of shape stabilized composites, tests were performed on the composite to investigate the thermal cyclic stability. It is essential for the PCM in TES applications to maintain its thermal properties stable for a number of heating and cooling cycles. For this, the shape stabilized composite with comparatively higher conductivity was selected. The DSC curves of 30 sequential heating and freezing cycles are shown in Figure 8.10 [103].
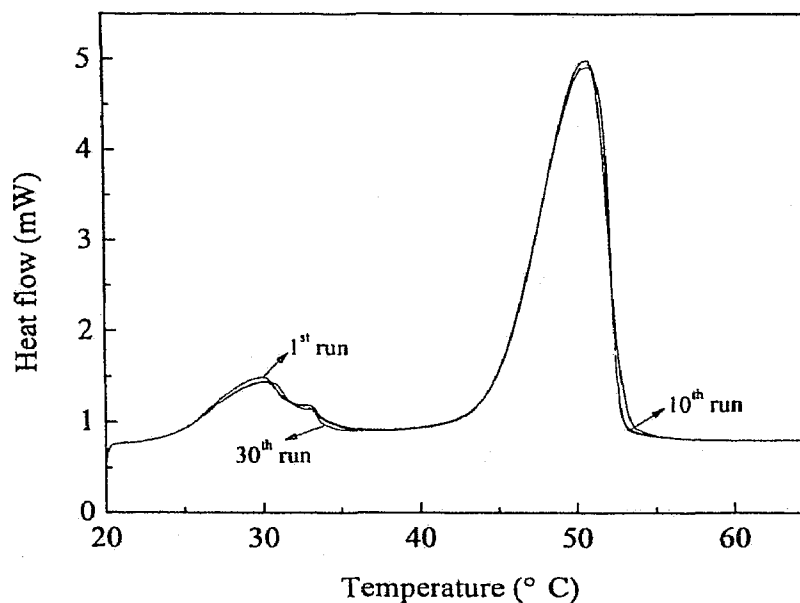
Figure 8.10: DSC test for the stability of 45:45:10:0 PCM composite.

It is visible in Figure 8.10 that the DSC curves of sequential heating and cooling cycles coincide. The transition temperature, melting temperature and latent heat of the composite are identical even after 30 melting and cooling cycles. This indicates that the composite is reusable. The thermal properties of the composite is summarized in Table 8.7 [103].

Table 8.7: Stability of phase change composite (wax (45%), HNT (45%), CNT (45%), and GNP (10%)).

Composite 50:40:0:10	Melting Properties		
	T_t (°C)	T_m (°C)	Total ΔH ($\frac{J}{g}$)
Run 1	44.9 %	50.9	92.6
Run 10	44.6	51.0	92.2
Run 30	44.7	51.0	92.2

In addition to the thermal stability test, mass loss of the composites was studied as well. The mass loss of the composites after 50 melting cycles are summarized

in Table 8.8 [103]. The results from the test demonstrated that the mass loss is higher for the sample with less halloysite content. For instance, the mass loss of wax/halloysite (90/10%) is higher than that of wax/halloysite (50/50%). The reason is because of the capability of halloysite to hold wax in its pores and network. This indicates that the higher halloysite content in the composite, the more it can preserve, resulting in comparatively less mass loss even after multiple heating-cooling cycles. Furthermore, the addition of graphite to the wax/halloysite composite demonstrated a significant decrease in mass loss. The mass loss from wax/halloysite composite is 6.75%, and this value decreased to 0.54%. Therefore, the addition of graphite to the wax/halloysite composite not only enhanced its thermal conductivity but also strengthened the thermal stability.

Table 8.8: Mass loss of phase change composite (melting point 52.3 °C).

Temperature (°C)	Mass loss (%)		
	Wax:HNT (90:10)	Wax:HNT (50:50)	Wax:HNT:GNP (45:45:10)
50	1.32	0.67	0.23
60	6.78	1.20	0.42
70	15.2	6.75	0.54

8.4 Conclusion

Tests were conducted to evaluate important characteristics of a new phase change material (PCM) that is suitable for application to buildings or other systems as part of the overall energy efficiency improvement. This phase-change insulation material combined unique characteristics of naturally occurring halloysite clay nanotubes (HNT) with low-cost paraffin wax. In addition to the inclusion of HNT, specific thermal

conductivity additives were also used to increase the average thermal conductivity of the various PCM mixtures. Additives considered were graphite nanoparticles (GNP) and common, multi-wall carbon nanotubes (CNT).

Through variations of the enhancement concentration, a range of values was achieved from 0.39 to 1.35 $\frac{W}{mK}$ among the various PCM materials as enhancements ranged from 3 to 20% by mass. Specific results indicated a maximum thermal conductivity was achieved of 1.35 $\frac{W}{mK}$ using a mix of 10:45:45 GNP:HNT:wax by mass.

The addition of the HNT allowed the material to maintain form after undergoing a phase change. This characteristic was noted with HNT concentrations above 30% by mass. This unique result also allowed the material to maintain the distribution of thermal conductivity enhancements within the composite, eliminating the need to remix and redistribute enhancements following repeated thermal cycling. This bodes well for future real-world use of these materials as no external containment is required and long-term property stability is achieved.

CHAPTER 9

CONCLUSIONS

This dissertation presents an approach to recover waste heat for power production and temporarily storing it for future use as well. The Waste can be stated as "the energy that is discarded to the environment without being put to practical usefulness". Waste heat is a result of both equipment inefficiency and thermodynamic limitation on equipment and process. In 2014, the United State consumed energy totaling 98.3 quadrillion of BTUs from sources like coal, petroleum, natural gas, nuclear, biomass and renewable resources [7]. The total energy consumed only 38.9 quadrillion of BTU was actually utilized for energy services and the rest of the 59.4 quadrillion of BTUs was rejected as waste heat. The waste heat accounts approximately 61% of the total energy consumed. It can be noted the availability of waste heat is abundant and it can itself become a potential heat source. This is where the notion of recovering and storing waste heat comes into effectiveness. In the effort to recover and store waste heat, a MEMS-based boiler capable of recovering heat and a thermal energy storage composite capable of storing heat via phase transformation is investigated.

The research began with the investigation of a MEMS-based for a waste heat recovery. As a preliminary study, a boiler with straight capillary channels and an acrylic steamdome covering was considered. A resistance heater was utilized as a heat

source. The boilerplates with a constant channel width of 100 μm and varying channel heights of 50 μm, 100 μm, 150 μm, and 170 μm were microfabricated in a silicon substrate. The tests were performed to study the effect of the channel's height in heat and mass transfer of the HFE-7200 refrigerant. The test results demonstrated a rise in heat and mass transfer with an increase in channel depth for a given power input to the boiler. The maximum heat and mass transfer via phase change of the working fluid for a channel height of 170 μm were 1.53 watts and 12.3 $\frac{mg}{s}$ and 0.58 watts and 4.6 $\frac{mg}{s}$ for the given power inputs of 3.6 watts and 2.6 watts, respectively. The boiler demonstrated a low energy conversion efficiency of about 22.3% and 42.5% for the power inputs of 2.6 watts and 3.6 watts, respectively. This low energy conversion was anticipated as a result of the larger volume of the acrylic steamdome causing premature condensation of the phase changed working fluid. Furthermore, the straight channel presented low fluid to surface contact area within the channels for maximum phase transformation of the working fluid. The maximum operating pressure attained by the boiler was 229 Pa for a flow rate of 5.4 $\frac{mg}{s}$.

Based on the results obtained from the preliminary boiler study, the boiler was modified to maximize the heat and mass transfer. The straight channels were modified to circular channels in the new boiler design to maximize fluid to the surface contact area. The acrylic steamdome covering was replaced with a glass steamdome of a thickness of 500 μm to minimize the steamdome mass. This modification significantly reduced the steamdome's height from 13 mm to 500 μm. The boilerplate with 100 μm width and 190 μm depth was microfabricated for the testing. The test presented heat and mass transfer of 1.48 watts and 13.6 $\frac{mg}{s}$ for a power input of 2.7 watts. The

boiler demonstrated energy conversion efficiency of about 54.8%. This indicates a rise of approximately 32.5% in energy conversion by the modified boiler compared to the previous design of 22.3%. The boiler operating pressure elevated from 229 Pa to 8.5 kPa as well. In addition to these testing, efforts were made to superheat the saturated steam to eliminate any liquid particles present in a vapor exiting the boiler. Such mixture of liquid and vapor may impinge turbine vanes during power production. Furthermore, the superheated steam contains more energy than the saturated steam. To superheat the vapor exiting the boiler, the steam was allowed to traverse through a heated serpentine shaped copper tube. Based on the operating pressure and temperature result, a thermodynamic T-s diagram was plotted for the HFE-7200 refrigerant at two different isobaric pressure points.

After this demonstration of boiler design modification and testing, the research focused on subsequent designing of the Superheater to form an integrated boiler/Superheater single system. The primary objective of the design was to utilize the same waste heat source to phase change the fluid and superheat the steam by placing the boiler atop the Superheater atop the heat source. Such system design will allow increased space efficiency in real-world applications. A computational modeling approach was considered to study the effects of design parameters on heat and mass transfer, temperature and pressure drop across the Superheater prior to fabrication and characterization. The input parameters to the model were based on the Superheater Test discussed previously. The results obtained from the modeling presented a Superheater with an aspect ratio of 1 (100 μm height:100 μm width) favorable for the Superheater fabrication considering pressure drop and heat flux rate

of 0.2 kPa and 10 $\frac{kW}{m^2}$, respectively. Moreover, the fluid exit temperature was 78° C comparatively higher than other considered aspect ratios.

After the optimization of the Superheater's design parameters, the boiler's capability to scavenge a real-world waste heat discarded from exhaust heat pipe was experimentally investigated. For this, a Exhaust Heat Recovery System (EHRS) was designed and built in the lab. The EHRS consisted of Exhaust System (ES), Exhaust Heat Exchanger System (EHES), and Integrated boiler/Superheater System. Each component constituting EHES was designed and fabricated. The fabricated components were assembled to form EHES and testing was performed to characterize its heat scavenging capability under the range of experimental conditions considered, depending upon air velocity and fluid supply rate. The testing began with the determination of working temperature and air velocity without Superheater included in the test setup. The working temperature of approximately 104° C was achieved via increasing the temperature of the air traversing EHES based on prior work. After the determination temperature, the working velocities of 0.92 $\frac{m}{s}$ and 1.2 $\frac{m}{s}$ were selected to study the effect of air flow rate on the energy trapped by the EHES and the energy absorbed by the boiler to phase change the working fluid. For each air velocity, the boiler's capability to absorb trapped heat from the EHES to phase transform the working fluid versus the refrigerant supply rate were studied. The tests were performed with fluid supply rates ranging 3 $\frac{mg}{s}$, 6 $\frac{mg}{s}$, 9 $\frac{mg}{s}$, and 13 $\frac{mg}{s}$. The test demonstrated the boiler was able to absorb maximum energy when the capillary flow rate achieved via capillary action of the channels matched the fluid supply rate pumped into the boiler. In this case, the flow rate of 9 $\frac{mg}{s}$ demonstrated the maximum power

absorption by the boiler. The test was then performed with the Superheater included in the experimental setup. The working air velocity of 0.92 $\frac{m}{s}$ and the temperature of approximately 104 °C were utilized for the testing. For the fluid supply rate of 3 $\frac{mg}{s}$, the Integrated boiler/Superheater System was able to phase transform and superheat the working fluid. However, with increased flow rate, the boiler was unable to phase change and pump fluid out of it as testing progressed. This highlighted the limitation on capillary channels' ability to phase change and pump fluid against developed head losses during increased fluid supply rate.

The work was then focused on the thermal energy storage part of the research. The research began with the fabrication of novel phase change material (PCM) that is suitable for application to buildings or other systems as part of the overall energy efficiency improvement. This phase-change insulation material combined unique characteristics of naturally occurring halloysite clay nanotubes (HNT) with low-cost paraffin wax. In addition to the inclusion of HNT, specific thermal conductivity additives were also used to increase the average thermal conductivity of the various PCM mixtures.

Additives considered were graphite nanoparticles (GNP) and common, multi-wall carbon nanotubes (CNT). Through variations of the enhancement concentration, a range of values was achieved from 0.39 to 1.35 $\frac{W}{mK}$ among the various PCM materials as enhancements ranged from 3 to 20% by mass. Specific results indicated a maximum thermal conductivity was achieved of 1.35 $\frac{W}{mK}$ using a mix of 10:45:45 GNP:HNT:wax by mass. The addition of the HNT allowed the material to maintain form after undergoing a phase change. This characteristic was noted with HNT concentrations

above 30% by mass. This unique result also allowed the material to maintain the distribution of thermal conductivity enhancements within the composite, eliminating the need to remix and redistribute enhancements following repeated thermal cycling. This bodes well for future real-world use of these materials as no external containment is required and long-term property stability is achieved.

9.1 Recommendations for Future Work

Results obtained from the test performed on both waste heat recovery and storage presented opportunities for improvement. Hence, to develop the technology and processes presented in this work further, the following recommendations for future work are suggested:

- The design and fabrication of boiler/Superheater System on a single substrate as shown in Figure 9.1. This way the boilerplate can be fabricated on one side and the Superheater on the other side of the substrate using microfabrication processes.

- The fabrication of the boiler and the Superheater in a single substrate will eliminate the thermal contact resistance developed while assembling two separately fabricated components.

- Due to the incorporation of inter-connected etched exit holes in the design, the head loss encountered during the Integrated boiler/Superheater System testing may be minimized. Furthermore, the recommended Superheater design parameter of 100 μm width by 100 μm depth capillary channels can be considered for fabrication to minimize the developed pressure gradient along the Superheater.

- In addition to these features, the design requires investigation of bonding techniques that will allow direct integration of silicon to copper (refer to Figure 9.1.
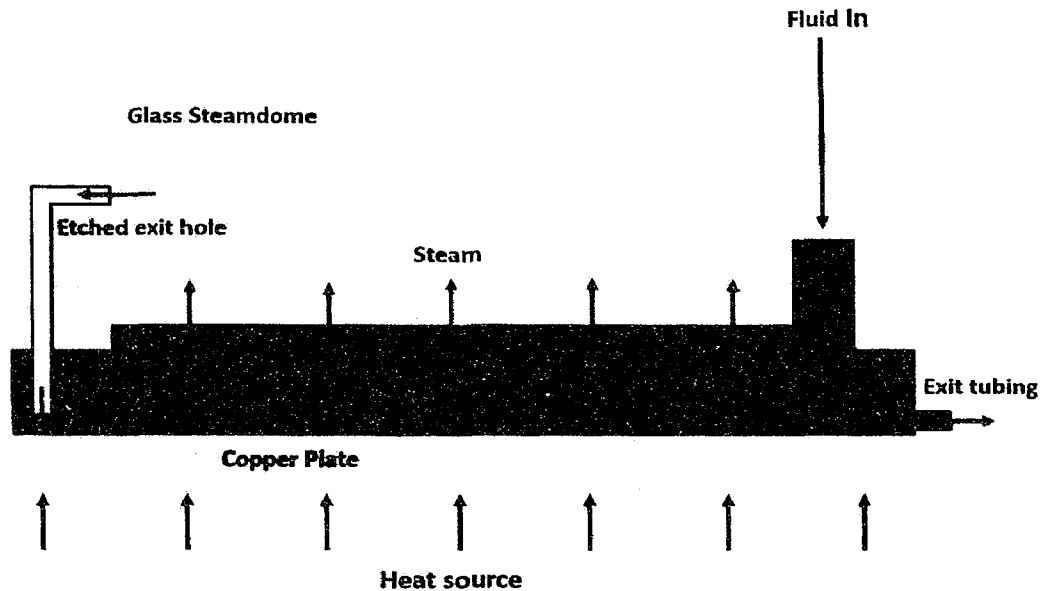
Figure 9.1: Recommended system design.

- The work requires integration of boiler/Superheater System with other devices such as free piston expanded and micro turbines for useful work output.

- Furthermore, the work requires testing of the boiler/Superheater System sourced by a thermal storage material.

APPENDIX A

COPYRIGHT PERMISSION FROM ASME

Dear Mr. Thapa,

It is our pleasure to grant you permission to use **all or any part of** the ASME paper "Halloysite Clay Nanotubes With PCM for Thermal Energy Storage and Efficiency," by S. Thapa, Y. Zhao, Y. Lvov and L. Weiss, Paper No. IMECE2013-63567, cited in your letter for inclusion in a PhD dissertation entitled Investigation of Small Scale Thermal recovery and Storage Systems to be published by Louisiana Tech University.

Permission is granted for the specific use as stated herein and does not permit further use of the materials without proper authorization. Proper attribution must be made to the author(s) of the materials. **Please note:** if any or all of the figures and/or Tables are of another source, permission should be granted from that outside source or include the reference of the original source. ASME does not grant permission for outside source material that may be referenced in the ASME works.

As is customary, we request that you ensure full acknowledgment of this material, the author(s), source and ASME as original publisher. Acknowledgment must be retained on all pages printed and distributed.

Many thanks for your interest in ASME publications.

Sincerely,

Beth Darchi
Publishing Administrator
ASME
2 Park Avenue, 6th Floor
New York, NY 10016-5990
Tel 1.212.591.7700
darchib@asme.org

APPENDIX B

COPYRIGHT PERMISSION FROM ELSEVIER

This is a License Agreement between Suvhashis Thapa ("You") and Elsevier ("Elsevier") provided by Copyright Clearance Center ("CCC"). The license consists of your order details, the terms and conditions provided by Elsevier, and the payment terms and conditions.
All payments must be made in full to CCC. For payment instructions, please see information listed at the bottom of this form.

Supplier	Elsevier Limited The Boulevard,Langford Lane Kidlington,Oxford,OX5 1GB,UK
Registered Company Number	1982084
Customer name	Suvhashis Thapa
Customer address	409 cameron st
	RUSTON, LA 71270
License number	3665671405696
License date	Jul 10, 2015
Licensed content publisher	Elsevier
Licensed content publication	Energy Conversion and Management
Licensed content title	Experimental and computational investigation of a MEMS-based boiler for waste heat recovery
Licensed content author	Suvhashis Thapa,Eric Borquist,Ashok Baniya,Leland Weiss
Licensed content date	August 2015
Licensed content volume number	100
Licensed content issue number	n/a
Number of pages	11
Start Page	403
End Page	413
Type of Use	reuse in a thesis/dissertation
Portion	full article
Format	both print and electronic
Are you the author of this Elsevier article?	Yes
Will you be translating?	No

Title of your thesis/dissertation	Investigation of small-scale thermal recovery and storage systems
Expected completion date	Nov 2015
Estimated size (number of pages)	100
Elsevier VAT number	GB 494 6272 12
Permissions price	0.00 USD
VAT/Local Sales Tax	0.00 USD / 0.00 GBP
Total	0.00 USD

Terms and Conditions

INTRODUCTION

1. The publisher for this copyrighted material is Elsevier. By clicking "accept" in connection with completing this licensing transaction, you agree that the following terms and conditions apply to this transaction (along with the Billing and Payment terms and conditions established by Copyright Clearance Center, Inc. ("CCC"), at the time that you opened your Rightslink account and that are available at any time at http://myaccount.copyright.com).

GENERAL TERMS

2. Elsevier hereby grants you permission to reproduce the aforementioned material subject to the terms and conditions indicated.

3. Acknowledgement: If any part of the material to be used (for example, figures) has appeared in our publication with credit or acknowledgement to another source, permission must also be sought from that source. If such permission is not obtained then that material may not be included in your publication/copies. Suitable acknowledgement to the source must be made, either as a footnote or in a reference list at the end of your publication, as follows:

"Reprinted from Publication title, Vol /edition number, Author(s), Title of article / title of chapter, Pages No., Copyright (Year), with permission from Elsevier [OR APPLICABLE SOCIETY COPYRIGHT OWNER]." Also Lancet special credit - "Reprinted from The Lancet, Vol. number, Author(s), Title of article, Pages No., Copyright (Year), with permission from Elsevier."

4. Reproduction of this material is confined to the purpose and/or media for which permission is hereby given.

5. Altering/Modifying Material: Not Permitted. However figures and illustrations may be altered/adapted minimally to serve your work. Any other abbreviations, additions, deletions and/or any other alterations shall be made only with prior written authorization of Elsevier Ltd. (Please contact Elsevier at permissions@elsevier.com)

6. If the permission fee for the requested use of our material is waived in this instance, please be advised that your future requests for Elsevier materials may attract a fee.

7. Reservation of Rights: Publisher reserves all rights not specifically granted in the combination of (i) the license details provided by you and accepted in the course of this licensing transaction, (ii) these terms and conditions and (iii) CCC's Billing and Payment terms and conditions.

8. License Contingent Upon Payment: While you may exercise the rights licensed immediately upon issuance of the license at the end of the licensing process for the transaction, provided that you have disclosed complete and accurate details of your proposed use, no license is finally effective unless and until full payment is received from you (either by publisher or by CCC) as

provided in CCC's Billing and Payment terms and conditions. If full payment is not received on a timely basis, then any license preliminarily granted shall be deemed automatically revoked and shall be void as if never granted. Further, in the event that you breach any of these terms and conditions or any of CCC's Billing and Payment terms and conditions, the license is automatically revoked and shall be void as if never granted. Use of materials as described in a revoked license, as well as any use of the materials beyond the scope of an unrevoked license, may constitute copyright infringement and publisher reserves the right to take any and all action to protect its copyright in the materials.

9. Warranties: Publisher makes no representations or warranties with respect to the licensed material.

10. Indemnity: You hereby indemnify and agree to hold harmless publisher and CCC, and their respective officers, directors, employees and agents, from and against any and all claims arising out of your use of the licensed material other than as specifically authorized pursuant to this license.

11. No Transfer of License: This license is personal to you and may not be sublicensed, assigned, or transferred by you to any other person without publisher's written permission.

12. No Amendment Except in Writing: This license may not be amended except in a writing signed by both parties (or, in the case of publisher, by CCC on publisher's behalf).

13. Objection to Contrary Terms: Publisher hereby objects to any terms contained in any purchase order, acknowledgment, check endorsement or other writing prepared by you, which terms are inconsistent with these terms and conditions or CCC's Billing and Payment terms and conditions. These terms and conditions, together with CCC's Billing and Payment terms and conditions (which are incorporated herein), comprise the entire agreement between you and publisher (and CCC) concerning this licensing transaction. In the event of any conflict between your obligations established by these terms and conditions and those established by CCC's Billing and Payment terms and conditions, these terms and conditions shall control.

14. Revocation: Elsevier or Copyright Clearance Center may deny the permissions described in this License at their sole discretion, for any reason or no reason, with a full refund payable to you. Notice of such denial will be made using the contact information provided by you. Failure to receive such notice will not alter or invalidate the denial. In no event will Elsevier or Copyright Clearance Center be responsible or liable for any costs, expenses or damage incurred by you as a result of a denial of your permission request, other than a refund of the amount(s) paid by you to Elsevier and/or Copyright Clearance Center for denied permissions.

LIMITED LICENSE

The following terms and conditions apply only to specific license types:

15. **Translation**: This permission is granted for non-exclusive world **English** rights only unless your license was granted for translation rights. If you licensed translation rights you may only translate this content into the languages you requested. A professional translator must perform all translations and reproduce the content word for word preserving the integrity of the article. If this license is to re-use 1 or 2 figures then permission is granted for non-exclusive world rights in all languages.

16. **Posting licensed content on any Website**: The following terms and conditions apply as follows: Licensing material from an Elsevier journal: All content posted to the web site must maintain the copyright information line on the bottom of each image; A hyper-text must be included to the Homepage of the journal from which you are licensing athttp://www.sciencedirect.com/science/journal/xxxxx or the Elsevier homepage for books

at http://www.elsevier.com; Central Storage: This license does not include permission for a scanned version of the material to be stored in a central repository such as that provided by Heron/XanEdu.

Licensing material from an Elsevier book: A hyper-text link must be included to the Elsevier homepage at http://www.elsevier.com . All content posted to the web site must maintain the copyright information line on the bottom of each image.

Posting licensed content on Electronic reserve: In addition to the above the following clauses are applicable: The web site must be password-protected and made available only to bona fide students registered on a relevant course. This permission is granted for 1 year only. You may obtain a new license for future website posting.

17. **For journal authors:** the following clauses are applicable in addition to the above:
Preprints:
A preprint is an author's own write-up of research results and analysis, it has not been peer-reviewed, nor has it had any other value added to it by a publisher (such as formatting, copyright, technical enhancement etc.).

Authors can share their preprints anywhere at any time. Preprints should not be added to or enhanced in any way in order to appear more like, or to substitute for, the final versions of articles however authors can update their preprints on arXiv or RePEc with their Accepted Author Manuscript (see below).

If accepted for publication, we encourage authors to link from the preprint to their formal publication via its DOI. Millions of researchers have access to the formal publications on ScienceDirect, and so links will help users to find, access, cite and use the best available version. Please note that Cell Press, The Lancet and some society-owned have different preprint policies. Information on these policies is available on the journal homepage.

Accepted Author Manuscripts: An accepted author manuscript is the manuscript of an article that has been accepted for publication and which typically includes author-incorporated changes suggested during submission, peer review and editor-author communications.

Authors can share their accepted author manuscript:
- – immediately
  - o via their non-commercial person homepage or blog
  - o by updating a preprint in arXiv or RePEc with the accepted manuscript
  - o via their research institute or institutional repository for internal institutional uses or as part of an invitation-only research collaboration work-group
  - o directly by providing copies to their students or to research collaborators for their personal use
  - o for private scholarly sharing as part of an invitation-only work group on commercial sites with which Elsevier has an agreement
- – after the embargo period
  - o via non-commercial hosting platforms such as their institutional repository
  - o via commercial sites with which Elsevier has an agreement

In all cases accepted manuscripts should:
- – link to the formal publication via its DOI
- – bear a CC-BY-NC-ND license - this is easy to do

- – if aggregated with other manuscripts, for example in a repository or other site, be shared in alignment with our hosting policy not be added to or enhanced in any way to appear more like, or to substitute for, the published journal article.

Published journal article (JPA): A published journal article (PJA) is the definitive final record of published research that appears or will appear in the journal and embodies all value-adding publishing activities including peer review co-ordination, copy-editing, formatting, (if relevant) pagination and online enrichment.

Policies for sharing publishing journal articles differ for subscription and gold open access articles:

Subscription Articles: If you are an author, please share a link to your article rather than the full-text. Millions of researchers have access to the formal publications on ScienceDirect, and so links will help your users to find, access, cite, and use the best available version.

Theses and dissertations which contain embedded PJAs as part of the formal submission can be posted publicly by the awarding institution with DOI links back to the formal publications on ScienceDirect.

If you are affiliated with a library that subscribes to ScienceDirect you have additional private sharing rights for others' research accessed under that agreement. This includes use for classroom teaching and internal training at the institution (including use in course packs and courseware programs), and inclusion of the article for grant funding purposes.

Gold Open Access Articles: May be shared according to the author-selected end-user license and should contain a CrossMark logo, the end user license, and a DOI link to the formal publication on ScienceDirect.

Please refer to Elsevier's posting policy for further information.

18. **For book authors** the following clauses are applicable in addition to the above: Authors are permitted to place a brief summary of their work online only. You are not allowed to download and post the published electronic version of your chapter, nor may you scan the printed edition to create an electronic version. **Posting to a repository:** Authors are permitted to post a summary of their chapter only in their institution's repository.

19. **Thesis/Dissertation:** If your license is for use in a thesis/dissertation your thesis may be submitted to your institution in either print or electronic form. Should your thesis be published commercially, please reapply for permission. These requirements include permission for the Library and Archives of Canada to supply single copies, on demand, of the complete thesis and include permission for Proquest/UMI to supply single copies, on demand, of the complete thesis. Should your thesis be published commercially, please reapply for permission. Theses and dissertations which contain embedded PJAs as part of the formal submission can be posted publicly by the awarding institution with DOI links back to the formal publications on ScienceDirect.

Elsevier Open Access Terms and Conditions

You can publish open access with Elsevier in hundreds of open access journals or in nearly 2000 established subscription journals that support open access publishing. Permitted third party re-use of these open access articles is defined by the author's choice of Creative Commons user license. See our open access license policy for more information.

Terms & Conditions applicable to all Open Access articles published with Elsevier:

Any reuse of the article must not represent the author as endorsing the adaptation of the article nor should the article be modified in such a way as to damage the author's honour or reputation. If any changes have been made, such changes must be clearly indicated.

The author(s) must be appropriately credited and we ask that you include the end user license and a DOI link to the formal publication on ScienceDirect.

If any part of the material to be used (for example, figures) has appeared in our publication with credit or acknowledgement to another source it is the responsibility of the user to ensure their reuse complies with the terms and conditions determined by the rights holder.

Additional Terms & Conditions applicable to each Creative Commons user license:

CC BY: The CC-BY license allows users to copy, to create extracts, abstracts and new works from the Article, to alter and revise the Article and to make commercial use of the Article (including reuse and/or resale of the Article by commercial entities), provided the user gives appropriate credit (with a link to the formal publication through the relevant DOI), provides a link to the license, indicates if changes were made and the licensor is not represented as endorsing the use made of the work. The full details of the license are available at http://creativecommons.org/licenses/by/4.0.

CC BY NC SA: The CC BY-NC-SA license allows users to copy, to create extracts, abstracts and new works from the Article, to alter and revise the Article, provided this is not done for commercial purposes, and that the user gives appropriate credit (with a link to the formal publication through the relevant DOI), provides a link to the license, indicates if changes were made and the licensor is not represented as endorsing the use made of the work. Further, any new works must be made available on the same conditions. The full details of the license are available at http://creativecommons.org/licenses/by-nc-sa/4.0.

CC BY NC ND: The CC BY-NC-ND license allows users to copy and distribute the Article, provided this is not done for commercial purposes and further does not permit distribution of the Article if it is changed or edited in any way, and provided the user gives appropriate credit (with a link to the formal publication through the relevant DOI), provides a link to the license, and that the licensor is not represented as endorsing the use made of the work. The full details of the license are available at http://creativecommons.org/licenses/by-nc-nd/4.0. Any commercial reuse of Open Access articles published with a CC BY NC SA or CC BY NC ND license requires permission from Elsevier and will be subject to a fee.

Commercial reuse includes:

- — Associating advertising with the full text of the Article
- — Charging fees for document delivery or access
- — Article aggregation
- — Systematic distribution via e-mail lists or share buttons

Posting or linking by commercial companies for use by customers of those companies.

20. Other Conditions:

v1.7

Questions? customercare@copyright.com or +1-855-239-3415 (toll free in the US) or +1-978-646-2777.

BIBLIOGRAPHY

[1] M. Tahani, S. Javan, and M. Biglari, "A comprehensive study on waste heat recovery from internal combustion engines using organic rankine cycle," *Thermal Science*, vol. 17, no. 2, pp. 611–624, 2013.

[2] R. El Chammas and D. Clodic, "Combined cycle for hybrid vehicles," SAE Technical Paper, Tech. Rep., 2005.

[3] I. Johnson, T. William, W. Choate, and A. Amber Davidson, "Waste heat recovery: technology and opportunities in U.S. industry," *U.S. Department of Energy, Office of Energy Efficiency and Renewable Energy, Industrial Technologies Program*, vol. 1, pp. 11–24, 2008.

[4] S. B. Viklund and M. T. Johansson, "Technologies for utilization of industrial excess heat: potentials for energy recovery and carbon dioxide emission reduction," *Energy Conversion and Management*, vol. 77, pp. 369–379, 2014.

[5] EIA, "Annual energy outlook 2013 early release overview," U.S. Energy Information Administration, U.S. Department of Energy Washington, DC 20585, Technical Report DOE/EIA-0383ER(2013), dec 2013. [Online]. Available: http://www.eia.gov/forecasts/aeo/er/pdf/0383er(2013).pdf.

[6] D. B. Fox, D. Sutter, and J. W. Tester, "The thermal spectrum of low-temperature energy use in the United States," *Energy & Environmental Science*, vol. 4, no. 10, pp. 3731–3740, 2011.

[7] L. L. N. Laboratory. (2014) Llnl energy flow chart. [Online]. Available: https://flowcharts.llnl.gov/.

[8] E. Ogbonnaya, A. Gunasekaran, and L. Weiss, "Fabrication of a MEMS-Based solar thermal collector for energy sustainability," in *Proceedings of the ASME 2011 International Mechanical Engineering Congress & Exposition IMECE2011*, vol. 1, Denver CO., 2011, pp. 1–10.

[9] S. Pincemin, X. Py, R. Olives, M. Christ, and O. Oettinger, "Elaboration of conductive thermal storage composites made of phase change materials and graphite for solar plant," *Journal of Solar Energy Engineering*, vol. 130, p. 011005, 2008.

[10] T.-C. Hung, T. Shai, and S. Wang, "A review of organic rankine cycles (orcs) for the recovery of low-grade waste heat," *Energy*, vol. 22, no. 7, pp. 661–667, 1997.

[11] S. Lu and D. Y. Goswami, "Optimization of a novel combined power/refrigeration thermodynamic cycle," *Journal of Solar Energy Engineering*, vol. 125, no. 2, pp. 212–217, 2003.

[12] E. Thorin, C. Dejfors, and G. Svedberg, "Thermodynamic properties of ammonia-water mixtures for power cycles," *International Journal of Thermophysics*, vol. 19, no. 2, pp. 501–510, 1998.

[13] P. Nag and A. Gupta, "Exergy analysis of the kalina cycle," *Applied Thermal Engineering*, vol. 18, no. 6, pp. 427–439, 1998.

[14] H. Chen, "The conversion of low-grade heat into power using supercritical rankine cycles," Ph.D. dissertation, University of South Florida, 2010.

[15] F. Ziegler, "Novel cycles for power and refrigeration," in *Proceedings of the 1st European Conference on Polygeneration Tarragona, Spain*, vol. 1, 2007.

[16] S. Vijayaraghavan and D. Goswami, "A combined power and cooling cycle modified to improve resource utilization efficiency using a distillation stage," *Energy*, vol. 31, no. 8, pp. 1177–1196, 2006.

[17] S. Trædal, "Analysis of the trilateral flash cycle for power production from low temperature heat sources," Ph.D. dissertation, Norwegian University of Science and Technology, 2014.

[18] I. Smith, N. Stosic, and C. Aldis, "Trilateral flash cycle systema high efficiency power plant for liquid resources," in *Proceedings of World Geothermal Congress, Firenze, Italy, May*, vol. 1, 1995, pp. 18–31.

[19] R. Stiedel, K. Brown, and D. Pankow, "The empirical modeling of a lysholm screw expander," in *Proceeding of Intersoc Energy Conversion Engineering Conference, United States*, vol. 1, 1983, pp. 11–21.

[20] Y. Chen, "Novel cycles using carbon dioxide as working fluid: new ways to utilize energy from low-grade heat sources," Ph.D. dissertation, Norwegian University of Science and Technology, 2006.

[21] Y. Chen, P. Lundqvist, and P. Platell, "Theoretical research of carbon dioxide power cycle application in automobile industry to reduce vehicles fuel consumption," *Applied Thermal Engineering*, vol. 25, no. 14, pp. 2041–2053, 2005.

[22] X.-R. Zhang, H. Yamaguchi, and D. Uneno, "Experimental study on the performance of solar rankine system using supercritical carbon dioxide," *Renewable Energy*, vol. 32, no. 15, pp. 2617–2628, 2007.

[23] S. Thapa, E. Borquist, A. Baniya, and L. Weiss, "Experimental and computational investigation of a mems-based boiler for waste heat recovery," *Energy Conversion and Management*, vol. 100, pp. 403–413, 2015.

[24] E. Ogbonnaya, A. Gunasekaran, and L. Weiss, "Micro solar energy harvesting using thin film selective absorber coating and thermoelectric generators," *Microsystem Technologies*, vol. 19, no. 7, pp. 995–1004, 2013.

[25] EIA, "Annual energy outlook 2011 early release overview," U.S. Energy Information Administration, U.S. Department of Energy Washington, DC 20585, Technical Report DOE/EIA-0384(2012), Sep 2011. [Online]. Available: https://www.eia.gov/totalenergy/data/annual/pdf/aer.pdf.

[26] A. K. C. Ferguson, *Internal Combustion Engines*. New York: John Wiley and sons Inc., 2001.

[27] R. Lipkin, "Micro steam engine makes forceful debut," *Science News*, vol. 144, no. 13, p. 197, 1993.

[28] C. Lee and L. G. Fréchette, "A silicon microturbopump for a rankine-cycle power generation microsystem Part I: Component and system design," *Journal of Microelectromechanical Systems*, vol. 20, pp. 312–325, 2011.

[29] C. Lee, M. Liamini, and L. G. Fréchette, "A silicon microturbopump for a rankine-cycle power-generation microsystemPart II: Fabrication and characterization," *Journal of Microelectromechanical Systems*, vol. 20, pp. 326–338, 2011.

[30] C. Lee, K. Jiang, P. Jin, and P. Prewett, "Design and fabrication of a micro wankel engine using mems technology," *Journal of Microelectronic Engineering*, vol. 73, pp. 529–534, 2004.

[31] L. W. Weiss, C. D. Richards, and R. F. Richards, "Power output force generation by a mems phase change actuator," *Journal of Microelectromechanical Systems*, vol. 20, no. 6, pp. 1287–1297, 2011.

[32] L. Weiss, "Resonant operation and cycle work from a mems-based micro-heat engine," *Microsystem Technologies*, vol. 15, no. 3, pp. 485–492, 2009.

[33] J. Cho, L. Weiss, C. Richards, D. Bahr, and R. Richards, "Power production by a dynamic micro heat engine with an integrated thermal switch," *Journal of Micromechanics and Microengineering*, vol. 17, no. 9, p. S217, 2007.

[34] L. W. Weiss, "Study of a mems-based free piston expander for energy sustainability," *Journal of Mechanical Design*, vol. 132, no. 9, p. 091002, 2010.

[35] S. Thapa, E. Ogbonnaya, C. Champagne, and L. Weiss, "Mems-based boiler operation from low temperature heat transfer and thermal scavenging," *Micromachines*, vol. 3, no. 2, pp. 331–344, 2012.

[36] B. Mathew, B. Jakub-Wood, E. Ogbonnaya, and L. Weiss, "Investigation of a mems-based capillary heat exchanger for thermal harvesting," *International Journal of Heat and Mass Transfer*, vol. 58, pp. 492–502, 2013.

[37] J. Jadhao and D. Thombare, "Review on exhaust gas heat recovery for ic engine," *International Journal of Engineering and Innovation Technology*, vol. 2, pp. 2–15, 2013.

[38] S. J. Kline and F. McClintock, "Describing uncertainties in single-sample experiments," *Mechanical engineering*, vol. 75, pp. 3–8, 1953.

[39] D. S. Kim, K.-C. Lee, T. H. Kwon, and S. S. Lee, "Micro-channel filling flow considering surface tension effect," *Journal of Micromechanics and Microengineering*, vol. 12, no. 3, pp. 230–236, 2002.

[40] E. Muntz, G. Shiftlett, D. Erwin, and J. Kunc, "Transient energy-release pressure-driven microdevices," *Journal of Microelectromechanical Systems*, vol. 1, no. 3, pp. 155–163, 1992.

[41] S. Spearing and K. Chen, "Micro-gas turbine engine materials and structures," in *Proceedings of the 21st Annual Conference on Composites, Advanced Ceramics, Materials, and Structures-B: Ceramic Engineering and Science Proceedings*, vol. 18, 1997, pp. 11–18.

[42] A. H. Epstein, S. A. Jacobson, J. M. Protz, and L. G. Frechette, "Shirtbutton-sized gas turbines: The engineering challenges of micro high speed rotating machinery," in *Proceedings of 8th International Symposium on Transport Phenomena and Dynamics of Rotating Machinery, Honolulu, HI*, vol. 1, 2000, pp. 1–10.

[43] H. Aichlmayr, D. Kittelson, and M. Zachariah, "Miniature free-piston homogeneous charge compression ignition engine-compressor conceptpart i: performance estimation and design considerations unique to small dimensions," *Chemical Engineering Science*, vol. 57, no. 19, pp. 4161–4171, 2002.

[44] S. Zhang, J. Wang, and Z. Guo, "Novel micro free-piston swing engine and its feasibility validation," *Tsinghua Science and Technology*, vol. 10, no. 3, pp. 381–386, 2005.

[45] S. Whalen, M. Thompson, D. Bahr, C. Richards, and R. Richards, "Design, fabrication and testing of the p3 micro heat engine," *Sensors and Actuators A: Physical*, vol. 104, no. 3, pp. 290–298, 2003.

[46] L. G. Fréchette, C. Lee, S. Arslan, and Y.-C. Liu, "Design of a microfabricated rankine cycle steam turbine for power generation," in *ASME 2003 International Mechanical Engineering Congress and Exposition*, vol. 1, 2003, pp. 335–344.

[47] F. Vélez, J. J. Segovia, M. C. Martín, G. Antolín, F. Chejne, and A. Quijano, "A technical, economical and market review of organic rankine cycles for the conversion of low-grade heat for power generation," *Renewable and Sustainable Energy Reviews*, vol. 16, no. 6, pp. 4175–4189, 2012.

[48] P. J. Mago and R. Luck, "Energetic and exergetic analysis of waste heat recovery from a microturbine using organic rankine cycles," *International Journal of Energy Research*, vol. 37, no. 8, pp. 888–898, 2013.

[49] T. Hung, "Waste heat recovery of organic rankine cycle using dry fluids," *Energy Conversion and Management*, vol. 42, pp. 539–553, 2001.

[50] H. Chen, D. Y. Goswami, and E. K. Stefanakos, "A review of thermodynamic cycles and working fluids for the conversion of low-grade heat," *Renewable and Sustainable Energy Reviews*, vol. 14, no. 9, pp. 3059–3067, 2010.

[51] M. Antonelli, A. Baccioli, M. Francesconi, U. Desideri, and L. Martorano, "Operating maps of a rotary engine used as an expander for micro-generation with various working fluids," *Applied Energy*, vol. 113, pp. 742–750, 2014.

[52] S. A. Zulkifli, M. N. Karsiti, and A. R. A. Aziz, "Starting of a free-piston linear engine-generator by mechanical resonance and rectangular current commutation," in *Proceeeding of Vehicle Power and Propulsion Conference*, vol. 1, 2008, pp. 1–7.

[53] B. Kongtragool and S. Wongwises, "A review of solar-powered stirling engines and low temperature differential stirling engines," *Renewable and Sustainable Energy Reviews*, vol. 7, no. 2, pp. 131–154, 2003.

[54] E. Lurie and A. Kribus, "Analysis of a microscale saturation phase-change internal carnot engine," *Energy Conversion and Management*, vol. 51, no. 6, pp. 1202–1209, 2010.

[55] C. Champagne and L. Weiss, "Investigation of a mems-based boiler and free piston expander for energy harvesting," in *ASME 2012 International Mechanical Engineering Congress and Exposition*, vol. 1, 2012, pp. 945–953.

[56] S. Thapa, J. Fang, D. Wood, and L. Weiss, "Investigation of microboiler for discarded thermal scavenging," in *ASME 2013 Heat Transfer Summer Conference collocated with the ASME 2013 7th International Conference on Energy Sustainability and the ASME 2013 11th International Conference on Fuel Cell Science, Engineering and Technology*, vol. 1, 2013, pp. V002T07A013–V002T07A013.

[57] H. Lee, T. Quy, C. Richards, D. Bahr, and R. Richards, "Experimental and numerical study of evaporative heat transfer from ten-micro microchannels," in *ASME 2006 International Mechanical Engineering Congress and Exposition*, vol. 1, 2006, pp. 371–375.

[58] J. Wei, H. Xie, M. Nai, C. Wong, and L. Lee, "Low temperature wafer anodic bonding," *Journal of Micromechanics and Microengineering*, vol. 13, no. 2, p. 217, 2003.

[59] Y. Bäcklund, K. Hermansson, and L. Smith, "Bond-strength measurements related to silicon surface hydrophilicity," *Journal of the Electrochemical Society*, vol. 139, no. 8, pp. 2299–2301, 1992.

[60] J. R. Armstead and S. A. Miers, "Review of waste heat recovery mechanisms for internal combustion engines," *Journal of Thermal Science and Engineering Applications*, vol. 6, p. 014001, 2014.

[61] M. S. Mohamed and J. L. Parker, "Enhanced boiling of hfe-7100 dielectric liquid on porous graphite," *Energy Conversion and Management*, vol. 46, pp. 2455–2481, 2005.

[62] M. S. El-Genk and J. L. Parker, "Enhanced boiling of hfe-7100 dielectric liquid on porous graphite," *Energy Conversion and Management*, vol. 46, no. 15, pp. 2455–2481, 2005.

[63] 3M, "The science of precision and electronic cleaning," *3M*, vol. 1, pp. 1–16, 2003.

[64] C. Champagne and L. Weiss, "Performance analysis of a miniature free piston expander for waste heat energy harvesting," *Energy Conversion and Management*, vol. 76, pp. 883–892, 2013.

[65] W. Qu and I. Mudawar, "Experimental and numerical study of pressure drop and heat transfer in a single-phase micro-channel heat sink," *International Journal of Heat and Mass Transfer*, vol. 45, no. 12, pp. 2549–2565, 2002.

[66] A. G. Fedorov and R. Viskanta, "Three-dimensional conjugate heat transfer in the microchannel heat sink for electronic packaging," *International Journal of Heat and Mass Transfer*, vol. 43, no. 3, pp. 399–415, 2000.

[67] J. Li, G. Peterson, and P. Cheng, "Three-dimensional analysis of heat transfer in a micro-heat sink with single phase flow," *International Journal of Heat and Mass Transfer*, vol. 47, no. 19, pp. 4215–4231, 2004.

[68] K. Kawano, M. Sekimura, K. Minakami, H. Iwasaki, and M. Ishizuka, "Development of micro channel heat exchanging," *JSME International Journal Series B Fluids and Thermal Engineering*, vol. 44, no. 4, pp. 592–598, 2001.

[69] X. Peng and G. Peterson, "Convective heat transfer and flow friction for water flow in microchannel structures," *International Journal of Heat and Mass Transfer*, vol. 39, no. 12, pp. 2599–2608, 1996.

[70] V. Dharaiya and S. Kandlikar, "Numerical investigation of heat transfer in rectangular microchannels under h2 boundary condition during developing and fully developed laminar flow," *Journal of Heat Transfer*, vol. 134, no. 2, p. 020911, 2012.

[71] K. Wojciechowski, M. Schmidt, R. Zybala, J. Merkisz, P. Fuć, and P. Lijewski, "Comparison of waste heat recovery from the exhaust of a spark ignition and a diesel engine," *Journal of Electronic Materials*, vol. 39, no. 9, pp. 2034–2038, 2010.

[72] A. C. Yunus and J. M. Cimbala, "Fluid mechanics: fundamentals and applications," *McGraw Hill Publication*, vol. 1, pp. 185–201, 2006.

[73] A. Diani, K. K. Bodla, L. Rossetto, and S. V. Garimella, "Numerical analysis of air flow through metal foams," *Energy Procedia*, vol. 1, no. 45, pp. 645–652, 2014.

[74] S. Mancin, C. Zilio, A. Diani, and L. Rossetto, "Experimental air heat transfer and pressure drop through copper foams," *Experimental Thermal and Fluid Science*, vol. 36, pp. 224–232, 2012.

[75] N. Dukhan and K.-C. Chen, "Heat transfer measurements in metal foam subjected to constant heat flux," *Experimental Thermal and Fluid Science*, vol. 32, no. 2, pp. 624–631, 2007.

[76] P. Elayiaraja, S. Harish, L. Wilson, A. Bensely, and D. Lal, "Experimental investigation on pressure drop and heat transfer characteristics of copper metal foam heat sink," *Experimental Heat Transfer*, vol. 23, no. 3, pp. 185–195, 2010.

[77] S. Mancin, C. Zilio, A. Diani, and L. Rossetto, "Air forced convection through metal foams: Experimental results and modeling," *International Journal of Heat and Mass Transfer*, vol. 62, pp. 112–123, 2013.

[78] G. Wallis and D. I. Pomerantz, "Field assisted glass-metal sealing," *Journal of Applied Physics*, vol. 40, no. 10, pp. 3946–3949, 1969.

[79] A. Sharma, V. Tyagi, C. Chen, and D. Buddhi, "Review on thermal energy storage with phase change materials and applications," *Renewable and Sustainable Energy Reviews*, vol. 13, no. 2, pp. 318–345, 2009.

[80] A. H. Abedin and M. A. Rosen, "A critical review of thermochemical energy storage systems," *Open Renewable Energy*, vol. 4, pp. 42–46, 2011.

[81] G. K. Pavlov and B. W. Olesen, "Building thermal energy storage-concepts and applications," in *12th ROOMVENT Conference*, vol. 1, 2011, pp. 1–10.

[82] G. A. Lane, *Solar heat storage: Latent heat materials*. CRC, 1986, vol. 2.

[83] D. N. Nkwetta and F. Haghighat, "Thermal energy storage with phase change materiala state-of-the art review," *Sustainable Cities and Society*, vol. 10, pp. 87–100, 2014.

[84] K. Pillai and B. Brinkworth, "The storage of low grade thermal energy using phase change materials," *Applied Energy*, vol. 2, no. 3, pp. 205–216, 1976.

[85] J. J. Conti, P. Holtberg, J. Beamon, A. Schaal, J. Ayoub, and J. Turnure, "Annual energy outlook 2011 with projections to 2035," *Office of Integrated and International Energy Analysis*, vol. 1, pp. 48–60, 2011.

[86] U. EIA, "Annual energy review," *Energy Information Administration, US Department of Energy: Washington*, no. DOE/EIA-0383ER(2011), 2011. [Online]. Available: http://www.eia.gov/forecasts/aeo/er/pdf/0383er(2011).pdf.

[87] E. Efficiency, "Buildings energy data book," *U.S. Department of Energy*, vol. 1, pp. 1–10, 2009.

[88] A. M. Papadopoulos and E. Giama, "Environmental performance evaluation of thermal insulation materials and its impact on the building," *Building and Environment*, vol. 42, no. 5, pp. 2178–2187, 2007.

[89] M. Hale *et al.*, "Survey of thermal storage for parabolic trough power plants," *NREL Report, No. NREL/SR-550-27925*, vol. 1, pp. 1–28, 2000.

[90] B. Zalba, J. M. Marin, L. F. Cabeza, and H. Mehling, "Review on thermal energy storage with phase change: materials, heat transfer analysis and applications," *Applied Thermal Engineering*, vol. 23, no. 3, pp. 251–283, 2003.

[91] A. M. Khudhair and M. M. Farid, "A review on energy conservation in building applications with thermal storage by latent heat using phase change materials," *Energy Conversion and Management*, vol. 45, no. 2, pp. 263–275, 2004.

[92] U. Stritih, "Heat transfer enhancement in latent heat thermal storage system for buildings," *Energy and Buildings*, vol. 35, no. 11, pp. 1097–1104, 2003.

[93] A. Hariri and I. Ward, "A review of thermal storage systems used in building applications," *Building and Environment*, vol. 23, pp. 1–10, 1988.

[94] M. Hadjieva, R. Stoykov, and T. Filipova, "Composite salt-hydrate concrete system for building energy storage," *Renewable Energy*, vol. 19, pp. 111–115, 2000.

[95] C. Klaassen, J. M. House, and I. E. Center, "Demonstration of load shifting and peak load reduction with control of building thermal mass," *Teaming for Efficiency: Commercial Buildings: Technologies, Design, Performance Analysis, and Building Industry Trends*, vol. 3, pp. 1–55, 2002.

[96] K. Peippo, P. Kauranen, and P. Lund, "A multicomponent pcm wall optimized for passive solar heating," *Energy and Buildings*, vol. 17, no. 4, pp. 259–270, 1991.

[97] K. Muruganantham, P. Phelan, P. Horwath, D. Ludlam, and T. McDonald, "Experimental investigation of a bio-based phase change material to improve building energy performance," in *ASME 2010 4th International Conference on Energy Sustainability*, vol. 1, 2010, pp. 979–984.

[98] K. R. Campbell and D. J. Sailor, "Phase change materials as thermal storage for high performance homes," in *Proceeding of ASME 2011 International Mechanical Engineering Congress and Exposition*, vol. 1, 2011, pp. 809–818.

[99] J. Li, P. Xue, W. Ding, J. Han, and G. Sun, "Micro-encapsulated paraffin/high-density polyethylene/wood flour composite as form-stable phase change material for thermal energy storage," *Solar Energy Materials and Solar Cells*, vol. 93, no. 10, pp. 1761–1767, 2009.

[100] L.-X. SUN and T. O. ZHANG, "Microencapsulation of n-eicosane as energy storage material," *Chinese Journal of Chemistry*, vol. 22, pp. 411–414, 2004.

[101] S. Thapa, S. Chukwu, A. Khaliq, and L. Weiss, "Fabrication and analysis of small-scale thermal energy storage with conductivity enhancement," *Energy Conversion and Management*, vol. 79, pp. 161–170, 2014.

[102] A. Trp, "An experimental and numerical investigation of heat transfer during technical grade paraffin melting and solidification in a shell-and-tube latent thermal energy storage unit," *Solar Energy*, vol. 79, no. 6, pp. 648–660, 2005.

[103] Y. Zhao, S. Thapa, L. Weiss, and Y. Lvov, "Phase change heat insulation based on wax-clay nanotube composites," *Advanced Engineering Materials*, vol. 16, no. 11, pp. 1391–1399, 2014.